STIF

ERT

06

Document P-0619
Type 3 Report
January 1975 through January 1976
September 1976

Prepared for
National Aeronautics and Space Administration
Goddard Space Flight Center,
Greenbelt, Maryland 20771

Investigation of mesoscale cloud features viewed by Landsat

Prepared by

Pieter J. Feteris
Anthony S. Lisa
Clinton J. Bowley
Mary Grace Fowler
James C. Barnes

ENVIRONMENTAL RESEARCH & TECHNOLOGY, INC.
CONCORD, MASS. • CHICAGO • LOS ANGELES • WASHINGTON, D.C.

ERT

Document P-0619
Type 3 Report
January 1975 through January 1976
September 1976

Prepared for
National Aeronautics and Space Administration
Goddard Space Flight Center,
Greenbelt, Maryland 20771

Investigation of mesoscale cloud features viewed by Landsat

Prepared by

Pieter J. Feteris
Anthony S. Lisa
Clinton J. Bowley
Mary Grace Fowler
James C. Barnes

ENVIRONMENTAL RESEARCH & TECHNOLOGY, INC.
CONCORD, MASS. • CHICAGO • LOS ANGELES • WASHINGTON, D.C.

1. Report No.	2. Government Accession No.	3. Recipient's Catalog No.

4. Title and Subtitle	5. Report Date
Investigation of Mesoscale Cloud Features Viewed by Landsat	September 1976
	6. Performing Organization Code
7. Author(s) Pieter J. Feteris, Anthony S. Lisa, Clinton J. Bowley, Mary Grace Fowler and James C. Barnes	8. Performing Organization Report No. P-619
	10. Work Unit No.
9. Performing Organization Name and Address Environmental Research & Technology, Inc. 696 Virginia Road Concord, Massachusetts 01742	11. Contract or Grant No. NAS5-20804
	13. Type of Report and Period Covered Final Report (Type III) January 1975 through January 1976
12. Sponsoring Agency Name and Address National Aeronautics & Space Administration Washington, D.C. 20546	14. Sponsoring Agency Code

15. Supplementary Notes
Technical Officer: Harold Oseroff
Goddard Space Flight Center
Greenbelt, Maryland

16. Abstract

Landsat imagery has been used to study cumulus cloud banding, wave clouds and other mesoscale cloud features. Characteristics of the cloud bands were determined from the Landsat imagery and compared with meteorological and topographical data to define the physical processes causing the cloud banding. These analyses showed that the measured conditions agreed well with those predicted by theories of shear instability and that the cloud street patterns could be used to estimate low-level winds. Analysis of the wave cloud situations indicated that a low-level wind maximum, in a marginally stable atmosphere, may favor the development of turbulent vortex pairs along the wind maximum.

17. Key Words (Suggested by Author(s))	18. Distribution Statement
Cumulus Cloud Banding Wave Clouds Landsat Imagery Mesoscale Cloud Features	Unclassified - Unlimited

19. Security Classif. (of this report)	20. Security Classif. (of this page)	21. No. of Pages	22. Price*
Unclassified	Unclassified	116	

*For sale by the Clearinghouse for Federal Scientific and Technical Information
Springfield, Virginia 22151

PREFACE

The purpose of the investigation described in this report was the study of cumulus cloud banding and other mesoscale cloud features using Landsat imagery. The specific objectives were two: to study cumulus cloud banding and determine the physical processes which cause it, and to study the relationships between meteorological conditions and other mesoscale cloud features observed by Landsat satellites. Typical of such features were wave clouds and severe storm situations.

Landsat visible and infrared imagery was selected during this study through the use of private and government browse files. From the selected cases, some fifty Landsat scenes were analyzed to identify the structure and characteristics of cumulus cloud bands. Meteorological and topographical conditions associated with each case were also carefully analyzed to provide information on the physical processes causing the cloud streets. These two data sets were then compared to determine the interaction among atmospheric, surface and cloud parameters, and to compare the interactions to those predicted by theories of shear instability in the Ekman boundary layer. Similar analyses were performed for wave clouds and severe storm cases.

Analyses of the cloud banding cases indicate that in nearly every instance the conditions predicted by theory were met. In addition, since the theory and the empirical measurements agreed, it was possible to estimate the characteristics of the low-level flow from the cloud street patterns. Unfortunately, verification of the results by observational data was hampered by the incompatibility of the resolution of the rawinsonde data with that of the Landsat data.

The results of the analyses of terrain-induced wave clouds indicate that a low-level wind maximum in a marginally unstable atmosphere may favor the development of turbulent vortex pairs along the wind maximum. These vortices, which would be triggered at the downwind slope of the mountain ridge and coincide with the wave crests, are considered significant because they could have an adverse effect on aircraft safety.

It is recommended that continued analyses be performed using Landsat data for mesoscale cloud studies. A significantly larger data set of cloud banding images was available for study than was possible to examine under this project. These cases should be analyzed for the development of a statistical data bank of cloud street characteristics and associated geophysical conditions. Furthermore, although the analysis here was hampered by the lack of correlative ground truth, special measurement networks (e.g., Project Hiplex) now in operation will permit a more detailed study of parameter interactions. Also, the interpretation of the cloud street patterns to estimate low-level winds over data-silent areas and to reveal regions of localized flow perturbations should be further investigated as a possible forecasting tool. Finally, additional Landsat imagery should be studied for further detection and analysis of the low-level wave clouds found during this study.

ACKNOWLEDGEMENTS

The investigation described in this report was performed for the National Aeronautics and Space Administration by Environmental Research & Technology, Inc. (ERT) under Contract No. NAS 5-20804. The Technical Monitor was Mr. Harold Oseroff of NASA Goddard Space Flight Center.

Overall direction in the study was provided by Mr. Paul E. Sherr, the Principal Investigator. Assistance in the data analysis was provided by Mr. Clyde Porter, Ms. Virginia Gates, Ms. Cynthia Bowley and Ms. Virginia Fowler.

TABLE OF CONTENTS

		Page
LIST OF ILLUSTRATIONS		xi
LIST OF TABLES		xiv
LIST OF SYMBOLS		xv
1.	INTRODUCTION	1
	1.1 Purpose and Objectives	1
	1.2 Applications of Landsat Data to Meteorology	1
	1.3 Contents of Report	3
2.	DATA SAMPLE	5
	2.1 Landsat Data	5
	2.2 Correlative Meteorological Data	11
3.	MESOSCALE CLOUD BANDS	15
	3.1 Flow Characteristics Associated with Cloud Banding	15
	3.2 Landsat Cases Selected to Study Cloud Bands	20
	3.3 Measurement of Cloud Band Parameters	24
	3.4 Summary of General Meteorological Conditions Associated with Cloud Band Patterns Observed in Landsat Data	25
	3.5 Case Study Analysis of Mesoscale Cloud Bands Seen In Landsat Images	27
	3.6 Discussion of Results of Cloud Band Analysis	40
4.	TERRAIN-INDUCED CLOUDS	45
	4.1 Description of Terrain-Induced Clouds	45
	4.2 Analysis of Terrain-Induced Clouds Seen in Landsat Imagery	46
	4.3 Discussion of the Results of the Analysis of Terrain-Induced Clouds	58
5.	OTHER MESOSCALE CLOUD FEATURES OBSERVED IN LANDSAT IMAGERY	61
	5.1 Cumulonimbus (Cb) Cells - New England and Florida	61
	5.2 Offshore Convective Cloud Bands - North Carolina	65
	5.3 Large-Scale Convective Cloud Bands Over Mountainous Terrain	67
	5.4 Altocumulus Cloud Layer - Ohio	67

TABLE OF CONTENTS (Continued)

		Page
6.	CONCLUSIONS	71
	6.1 Conclusions Based on Analysis of Mesoscale Cloud Patterns	71
	6.2 Advantages and Limitations of Landsat Data	72
	6.3 Recommendations for Further Study Using Landsat Data	73
REFERENCES		75
APPENDIX A	THEORY OF FORMATION OF MESOSCALE CLOUD BANDS	A-1
APPENDIX B	THEORY OF FLOW FOR TERRAIN-INDUCED CLOUDS	B-1

LIST OF ILLUSTRATIONS

Figure		Page
3-1	Landsat-1 MSS-5 Image (I. D. No. 1284-15552), 3 May 1973, Showing Extratropical Cloud Bands Occurring in a Polar Outbreak over Tennessee	17
3-2	Diagram Showing the Variables in Kuettner's Theory of Banded Cumulus Convection: a) Wind Profile, b) Cloud Band Geometry	18
3-3	Landsat-1 MSS-5 Image (I. D. No. 1638-15150), 22 April 1974, Showing Cloud Band Located over the Flat Terrain of the Carolinas Coastal Plain	22
3-4	Landsat-1 MSS-5 Image (I. D. No. 1375-16003), 2 August 1973, Showing Cloud Bands Located over the Mostly Hilly Terrain of the Tennessee, Alabama and Mississippi Border Region	23
3-5	Landsat-1 MSS-5 Image (I. D. No. 1329-15014), 17 June 1973, Showing Cumulus Cloud Banding over Southern New England	28
3-6	Upper Air Soundings, 17 June 1973, at 0600 GMT	29
3-7	Landsat-1 MSS-5 Images (I. D. Nos. 1727-15041 and 1727-15043), 20 July 1974, Showing Cloud Banding over the New York and Pennsylvania Area	32
3-8	Diagram Showing Relationship between Alignment of Cloud Bands in Figure 3-7 and Surface Isobars, 20 July 1974 at 1500 GMT	35
3-9	Landsat-1 MSS-5 Image (I. D. No. 1543-14453), 17 January 1974, Showing Cloud Bands Developing over the Ocean off the Coast of Maine	38
3-10	Frequency Distributions of Cloud Band Parameters Measured from Landsat Data Sample	42
3-11	Comparison between Average Wind Speed in the Convective Layer Computed from Cloud Band Configurations in Landsat Imagery	43
4-1	Landsat-1 MSS-5 image (I. D. No. 1256-18212), 5 April 1973, Showing Terrain-Induced Clouds Located over the Columbia Basin Area of Washington	49

LIST OF ILLUSTRATIONS (Continued)

Figure		Page
4-2	Landsat-1 MSS-5 Image (I. D. No. 1598-14500), 13 March 1974, Showing Distinct Pattern of Wave Clouds over Maine	50
4-3	Diagram Showing Vertical Wind Profile (U) and Curvature (U'') for Portland, Maine at 1200 GMT, 13 March 1974	51
4-4	Landsat-1 MSS-7 (near-IR) Image (I. D. No. 1599-14554), 14 March 1974, Showing Wave Clouds over Northern New Hampshire	53
4-5	Adiabatic Diagram for the Portland, Maine 1200 GMT, Rawinsonde Data of 14 March 1974	54
4-6	Landsat-1 MSS-5 Image (I. D. No. 1257-15021), 6 April 1973, Showing a Dissipating Wave Cloud Pattern over Southern New England	56
4-7	Adiabatic Diagrams Showing Temperature, Dew Point, and Winds at Chatham, Mass. and New York City, 1200 GMT, 6 April 1973	57
5-1	Landsat-1 MSS-5 Image (I. D. No. 1401-15001), 28 August 1973, Viewing a Massive Cumulonimbus Cell over Central New Hampshire	62
5-2	Comparison between Area of Cumulonimbus Cell and Cirrus Anvil Seen in Landsat Image (Figure 5-1) and the Actual Precipitation Area Measured by Radar at the Time of the Satellite Observation	63
5-3	Landsat-1 MSS-5 Image (I. D. No. 1388-15325), 15 August 1973, Showing Three Different Scales of Convective Cells over Northern Florida	64
5-4	Landsat-1 MSS-5 Image (I. D. No. 1438-15074), 4 October 1973, Viewing Convective Cloud Formations over the Ocean Just East of Cape Hatteras	66
5-5	Landsat-1 MSS-5 Image (I. D. No. 1642-17193), 26 April 1974, Showing Large-scale Convective Bands over Colorado and Wyoming	68
5-6	Landsat-1 MSS-5 Image (I. D. No. 1390-15412), 17 August 1973, Showing What Appears to be Fields of Altocumulus Floccus and Castellanus over Ohio	69

LIST OF ILLUSTRATIONS (Continued)

Figure		Page
A-1	Graph Showing the Correlation between Maximum Wind Speed (U_{max}) and Average Speed ($\overline{U}^{H}$) in Convective Layers during Strong Surface Heating	A-5
A-2	Graph Showing the Average Wind Speed in the Layer $0<z<H$ as a function of λ_x and H for Specified Conditions	A-9
A-3	Graph Showing Average Wind Speed in the Layer $0<z<H$ as a Function of H and $g\beta$ for Specified Conditions	A-10
B-1	Graph Showing Solution of Equation 4 for $\overline{U}$ when $F = (2\pi/\lambda)^2 = \overline{U}''/\overline{U}$	B-3

LIST OF TABLES

Table		Page
2-1	Summary of Landsat-1 Cases Selected from ERT In-House Data and 16 mm Microfilm	6
2-2	Summary of Landsat Cases Selected from Review of USGS Browse File	7
2-3	Cloud Street Cases Analyzed	8
2-4	Wave Cloud Cases Analyzed	8
2-5	Cumulonimbus Cloud Cases Analyzed	10
2-6	Classification of Synoptic Conditions	13
3-1	Cloud Street Pattern Characteristics in Relation to Terrain and Circulation Types	21
3-2	Cloud Street Characteristics, 17 June 1973 Case	30
3-3	Comparison of Flow Properties Computed from Cloud Characteristics with Ground Truth; 17 June 1973 Case	30
3-4	Comparison of Flow Properties Derived from Cloud Street Characteristics with Ground Truth, 20 July 1974 Case	34
3-5	Cloud and Airflow Characteristics, 20 July 1974 Case	37
3-6	Comparison of Flow Characteristics Derived from Cloud Street Features with Ground Truth	41
4-1	Wave Cloud Pattern Characteristics in Relation to Terrain and Circulation Types	48
4-2	Comparison of Wind Speeds Computed from Wave Cloud Characteristics with Atmospheric Parameters	59
A-1	Dependence of the Relative Error in the Computed Average Wind Speed $\bar{U}^H$ on the Location of the Wind Maximum	A-6
A-2	Dependence of the Coefficient K_6 in Equation 7a on Assumed Values for the wind Speed C_3	A-6
A-3	Dependence of Solution of Equation 17 on Assumed Values of Pertinent Coefficients	A-15

LIST OF SYMBOLS

B_m is the mountain half-width measured towards the downwind side.

$\overline{\beta}$ is the averaged instability of the unstable layer.

Γ_d is the dry adiabatic lapse rate.

Γ_e is the environmental lapse rate.

$C_{1,2,3}$ are constants.

$\overline{D}$ is the vectorially averaged wind direction.

$\overline{D}^H$ is the vectorially averaged wind direction over the depth of the conditionally unstable layer.

D_{geo} is the direction of the geostrophic wind.

D_{850} is the wind direction at the 850 millibar (mb) level.

$\overline{D}_{RS}$ is the vectorially averaged wind direction determined from rawinsonde.

H is the height of the cloud tops above the surface.

H_s is the depth of the cloud layer in which the waves form, estimated from soundings.

η is the location of the wind speed.

κ is the heat of diffusivity parameter.

L is the length of the cloud street.

l is the length of the mountain ridge.

λ is the wavelength.

λ_x is the spacing of the cloud elements in a row.

λ_y is the spacing of the rows.

n is the number of waves in the wave train.

ν is the kinematic viscosity momentum.

σ is the static stability.

$\overline{T}$ is the averaged temperature.

$\overline{U}$ is the averaged wind speed.

LIST OF SYMBOLS (Continued)

$\overline{U}^H$ is the averaged wind speed over the depth for the conditionally unstable layer.

U_s is the surface wind speed.

$\overline{U}_{5.4}$ is the averaged wind speed in the convective layer using C_3=5.4.

$\overline{U}_o$ is the averaged wind speed in the convective layer using C_3=0.

$\overline{U}_{RS}$ is the averaged wind speed computed from rawinsonde data.

$\overline{U}_1$ is the averaged wind speed computed from wavelength and static stability (Equations 19 or 20).

$\overline{U}_2$ is the averaged wind speed computed from H_s and λ, assuming σ=0 (Equation 21),

$$\lambda/H_s < 0.2$$

$\overline{U}''$ is the second derivative of the ambient wind with respect to height averaged over the depth H.

$\overline{V}^H$ is the vectorially averaged wind speed over the depth of the conditionally unstable layer.

V_{geo} is the speed of the geostrophic wind.

V_{max} is the maximum wind speed.

V_{850} is the wind speed at the 850 mb level.

Z_m is the height of the mountain tops.

1. INTRODUCTION

1.1 Purpose and Objectives

The purpose of this investigation was to use Landsat data to study mesoscale cloud features. Specifically, the investigation had two objectives: (1) to study cumulus cloud banding and the physical processes which cause it; and (2) to correlate meteorological conditions with other mesoscale cloud features observed by Landsat. With regard to the study of cloud banding, the parameters derived from the Landsat imagery were related to the appropriate meteorological and topographic conditions, and the results of this analysis were compared to results predicted by theories of shear instability in the Ekman boundary layer. Other mesoscale cloud features studied included wave clouds and cumulonimbus (Cb) cells of various sizes.

In the course of the investigation, some 50 Landsat scenes were analyzed. The majority of these cases were in the northeastern United States where the network of meteorological reporting stations is somewhat denser than in other parts of the country, and thus more adequate for studying mesoscale phenomena. Through the comparative analysis of the features detected in the Landsat images and conventional meteorological data, it has been possible to gain a better understanding of the formation and characteristics of various mesoscale cloud features. Furthermore, since cumulus cloud banding is closely related to the low-level wind field, the results of the study also led to the development of new techniques for deriving winds in data sparse areas.

1.2 Applications of Landsat Data to Meteorology

The Landsat satellite is designed primarily to view the earth's surface rather than the earth's clouds. This is in contrast to other operational satellite systems, such as the NOAA-VHRR (Very High Resolution Radiometer), which are designed primarily for meteorological purposes. Nevertheless, as Landsat data have been accumulated, it has become obvious that the images display a considerable amount of information relevant to meteorology.

The initial spacecraft in the Landsat series was placed into orbit at a height of about 900 km in late July 1972. The second spacecraft, Landsat-2, was placed in operation in January 1975. The principal sensor system on board Landsat, the Multispectral Scanner Subsystem (MSS), observes in four bands, which are in the visible and near-infrared portions of the spectrum. The four bands are designated as the MSS-4 (green, 0.5 - 0.6 μm), MSS-5 (red, 0.6 - 0.7 μm), MSS-6 (red/near-infrared, 0.7 - 0.8 μm), and MSS-7 (near-infrared, 0.8 - 1.1 μm). Observations are only available, therefore, during the daytime.

Landsat views an area 185 km wide (as compared to some 2,000 km for a VHRR image), and has a resolution of 70 to 100m (as compared to approximately approximately 1 km for the VHRR). Because of the relatively narrow swath, the satellite can not provide daily coverage, as is possible with the VHRR. At low-and mid-latitudes, Landsat repeats coverage of the same area once every 18 days (at mid-latitudes, some overlap does occur from one day to the next). With two spacecraft in operation, repeat coverage occurs every nine days.

Because of the emphasis on the use of the early Landsat-1 data for earth resources applications, very few studies related to meteorology were attempted. The studies that have been carried out have been directed almost entirely towards the use of the data for environmental surveys. In these efforts, which are summarized by Walter (1973) and Greenwood (1974), the use of Landsat data to detect certain types of air pollution has been demonstrated.

Among the studies related to the detection of atmospheric effects using Landsat data are those reported by Lyons and Pease (1973), Griggs (1974), Copeland, et al. (1974), and Lyons and Northouse (1974). Lyons and Pease found it possible to detect the long-range transport (over 50 km) of suspected particulate plumes from the Chicago-Gary steel mill complex over Lake Michigan using mainly the MSS-5 spectral band; these investigators have also shown that the interaction of air pollution and meteorology over the Great Lakes, which leads to inadvertent weather modification, can be observed in Landsat images. Griggs found that radiance measurements over water (from Landsat digitized data) could be used to calculate the vertical aerosol burden to an accuracy approaching ±10 percent, whereas Copeland, et al. have confirmed that Landsat can

be used to detect smoke plumes and aircraft contrails. In studies of haze in the Los Angeles basin, a correlation was found between radiance and visibility, but it was concluded that the radiance values over land were not a particularly sensitive measurement of air pollution (Greenwood, 1974).

The use of analytical models in conjunction with Landsat data has also been studied. Lyons and Pease are modeling the Great Lakes area to study the interaction of air pollution and the dynamics of cloud behavior and have shown verification in a qualitative sense. Griggs is using models of the atmospheric aerosol distribution as part of his data analysis technique to convert radiance values to aerosol burden. Several investigators have considered the use of Landsat imagery for verification of models to predict plume and contrail dispersion, but no definitive results have yet been reported (Greenwood, 1974).

Through these environmental-survey studies and through other investigations related to disciplines such as hydrology and marine resources, it has become evident that Landsat data are well suited for studying mesoscale cloud features. In studies of arctic sea ice, for example, detailed stratus cloud streaks forming over open water areas have been detected (Barnes and Bowley, 1974). Also, in general descriptions of Landsat images, cloud patterns, apparently influenced by urban areas, have been discussed qualitatively. The ground resolution of the MSS is nearly as good as the resolution from a high-altitude aircraft, and yet a single image covers an area of 185 km square. Thus, for the first time, it is possible to analyze detailed mesoscale cloud features and, at the same time, to view a large enough area to ascertain the extent of a particular cloud pattern and in some instances the relationships of the mesoscale pattern to the overall synoptic scale cloud pattern.

1.3 Contents of Report

The data sample used in this investigation is discussed in Section 2 of the report. With regard to the Landsat data sample, the data search and data handling procedures are explained, and the cases selected for analysis are listed; the sources of the correlative meteorological observations used in the study are also explained. In Section 3 and Appendix A, the theory of the formation of mesoscale cloud bands and the

application of the theory for satellite cloud observations are discussed; the analysis of cloud bands seen in Landsat imagery, including the detailed analysis of three cases, is presented in Section 3. In Section 4, terrain-induced clouds are discussed, and the detailed analysis of mesoscale wave clouds in selected Landsat cases is presented. Other mesoscale cloud features seen in Landsat imagery, including cumulonimbus cells, are discussed in Section 5. The conclusions of the investigation are presented in Section 6 along with recommendations for future work using Landsat data.

2. DATA SAMPLE

2.1 Landsat Data

2.1.1 Data Search Procedure

The Landsat data sample used in the investigation was collected through three data-search methods. Initially, Landsat-1 images, already on file at ERT from earlier investigations, were reviewed to select images displaying cumulus cloud bands (streets), wave clouds, cumulonimbus cells, and other mesoscale cloud features. The majority of the data was over the midwestern United States. Landsat-1 16 mm microfilm, also on file at ERT, was reviewed to select additional cases. Through these two procedures, some 42 Landsat-1 images were selected for analysis; the dates and identifier numbers for these images are given in Table 2-1. The time of the Landsat image on each day is about 1000 LST.

An additional 98 Landsat-2 images, showing mesoscale cloud features, were selected from review of the Landsat browse file located at the Boston office of the United States Geological Survey (USGS). The dates and image identifier numbers for these scenes are shown in Table 2-2.

A further review of more recent Landsat-2 data at the USGS browse file produced 76 additional cases, which were placed on order. Unfortunately, however, these data were severely damaged in shipping, and the time required for reprocessing did not allow analysis of these cases for inclusion in the report.

Once selection of the images was completed, using these data search procedures, the individual frames were placed on order from NOAA-NESS Landsat data processing facility. Since many of the initial cases were selected from ERT's in-house Landsat data file, the cost of the data required to complete the study was considerably reduced.

2.1.2 Cases Selected for Analysis

From review and interpretation of the initially selected images, a total of 24 cloud street cases (shown in Table 2-3) was selected for detailed analysis of the spacing and heights of the individual cloud

TABLE 2-1

SUMMARY OF LANDSAT-1 CASES SELECTED FROM
ERT IN-HOUSE DATA AND 16 mm MICROFILMS

Date	Image I.D. No.	Date	Image I.D. No.
26 July 72	E-1803-16332	24 August 73	E-1397-16242
05 August 72	E-1013-17302	24 August 73	E-1397-10065
31 October 72	E-1008-15192	27 September 73	E-1431-16130
02 August 73	E-1375-17344	26 August 74	E-1764-15115
02 August 73	E-1375-15591	26 August 74	E-1764-16505
02 August 73	E-1375-16003	29 August 74	E-1767-15294
04 October 73	E-1438-15074	15 April 74	E-1631-17593
06 August 73	E-1379-16235	25 August 74	E-1763-15061
06 August 73	E-1379-16242	11 April 74	E-1627-11364
06 August 73	E-1379-16250	11 April 74	E-1627-17373
08 August 73	E-1381-14511	16 April 74	E-1632-14375
08 August 73	E-1624-15352	16 April 74	E-1632-14382
09 August 73	E-1382-16481	22 April 74	E-1638-15144
12 August 73	E-1365-15113	22 April 74	E-1638-15150
13 August 73	E-1386-15181	26 April 74	E-1642-15352
15 August 73	E-1388-15325	26 April 74	E-1642-17170
17 August 73	E-1390-15412	26 April 74	E-1642-17193
21 August 73	E-1759-16270	27 April 74	E-1643-15402
21 August 73	E-1759-18042	29 April 74	E-1645-15553
22 August 73	E-1760-16281	07 May 74	E-1653-16402
23 August 73	E-1761-16382		
24 August 73	E-1762-16404		

TABLE 2-2

SUMMARY OF LANDSAT CASES SELECTED FROM REVIEW OF USGS BROWSE FILE

Date	Image I.D. No.	Date	Image I.D. No.
23 June 75	E-2152-17114	03 July 75	E-2162-16300
23 June 75	E-2152-17121	03 July 75	E-2162-16305
23 June 75	E-2152-17123	03 July 75	E-2162-14423
23 June 75	E-2152-17130	03 July 75	E-2162-14441
23 June 75	E-2152-17132	03 July 75	E-2162-18102
23 June 75	E-2152-17135	03 July 75	E-2162-18111
23 June 75	E-2152-14141	03 July 75	E-2162-18483
23 June 75	E-2152-17144	04 July 75	E-2163-14482
23 June 75	E-2152-17150	04 July 75	E-2163-14491
23 June 75	E-2152-17153	04 July 75	E-2163-14493
23 June 75	E-2152-17155	04 July 75	E-2163-14500
24 June 75	E-2153-17170	04 July 75	E-2163-14514
24 June 75	E-2153-17173	04 July 75	E-2163-18142
24 June 75	E-2153-17175	04 July 75	E-1263-18145
24 June 75	E-2153-17182	04 July 75	E-2163-16345
24 June 75	E-2153-17104	04 July 75	E-2163-16354
24 June 75	E-2153-17191	04 July 75	E-2163-16361
24 June 75	E-2153-17193	04 July 75	E-2163-16363
24 June 75	E-2153-17200	06 July 75	E-2163-15003
24 June 75	E-2153-17211	06 July 75	E-2165-14594
24 June 75	E-2153-17220	06 July 75	E-2165-15033
24 June 75	E-2153-17202	06 July 75	E-2165-15044
24 June 75	E-2153-15300	06 July 75	E-2165-21452
24 June 75	E-2153-15382	06 July 75	E-2165-21454
24 June 75	E-2153-15385	08 July 75	E-2167-15125
24 June 75	E-2173-14500	10 July 75	E-2169-20254
25 June 75	E-2154-13593	12 July 75	E-2171-15363
25 June 75	E-2154-15400	15 July 75	E-2174-17370
27 June 75	E-2156-17344	16 July 75	E-2175-17424
27 June 75	E-2156-17350	18 July 75	E-2177-16123
27 June 75	E-2156-17355	18 July 75	E-2177-16130
27 June 75	E-2156-17362	18 July 75	E-2177-17525
27 June 75	E-2156-17371	18 July 75	E-2177-21110
27 June 75	E-2156-17385	19 July 75	E-2178-16104
28 June 75	E-2157-17405	19 July 75	E-2178-16190
28 June 75	E-2157-17411	19 July 75	E-2178-16195
28 June 75	E-2157-17414	24 July 75	E-2153-17164
28 June 75	E-2157-17420	25 July 75	E-2184-15101
28 June 75	E-2157-17423	25 July 75	E-2184-15110
30 June 75	E-2159-16084	11 August 75	E-2201-16471
30 June 75	E-2159-16090	13 August 75	E-2203-16531
01 July 75	E-2160-17565	13 August 75	E-2203-16575
01 July 75	E-2160-17571	13 August 75	E-2203-16581
01 July 75	E-2160-17585	13 August 75	E-2203-18363
01 July 75	E-2160-18001	13 August 75	E-2203-15122
02 July 75	E-2161-16223	14 August 75	E-2204-15190
02 July 75	E-2161-18043	14 August 75	E-2204-15213
03 July 75	E-2162-16282	14 August 75	E-2204-17024
03 July 75	E-2162-16284	14 August 75	E-2204-17033
03 July 75	E-2162-16291	15 August 75	E-2205-15264

TABLE 2-3

CLOUD STREET CASES ANALYZED

Date	Image I.D. No.	Location
03 May 73	1284-15550	Kentucky
03 May 73	1284-15552	Tennessee
03 May 73	1284-15555	Tennessee-Alabama
17 June 73	1329-15014	Massachusetts-Rhode Island
02 August 73	1375-15591	Indiana
24 August 73	1397-16242	Texas
01 January 74	1543-14453	Off Maine coast
22 April 74	1638-15150	No. Carolina coast
22 April 74	1638-15152	No. Carolina coast
20 July 74	1727-15040	New York
21 August 74	1759-16270	Texas
22 August 74	1760-16281	Minnesota
30 June 75	2159-16090	Wisconsin
30 June 75	2159-16090	Michigan
03 July 75	2162-16282	Kansas
03 July 75	2162-16284	Kansas
04 July 75	2163-16354	Texas
04 July 75	2163-16363	Texas
04 July 75	2163-16345	Oklahoma
12 July 75	2171-15363	Ohio
18 July 75	2177-16123	Louisiana
18 July 75	2177-16123	Texas
25 July 75	2184-15110	Florida
24 August 75	1762-16404	Nebraska

TABLE 2-4

WAVE CLOUD CASES ANALYZED

Date	Image I.D. No.	Location
31 July 72	1008-15192	Virginia
05 April 73	1256-18212	Washington State
06 April 73	1257-15021	Connecticut
20 April 73	1271-16261	Texas
20 April 73	1271-16264	Texas Gulf Coast
22 April 73	1273-16351	Kansas
13 March 74	1598-14500	Maine
14 March 74	1599-14554	Maine
11 April 74	1627-17364	Utah
11 April 74	1627-17373	West Central Utah
26 April 74	1642-15352	Michigan
08 May 74	1654-15004	Vermont
04 July 75	2163-14491	Maine-New Hampshire

bands, as well as for analysis of the band lengths and orientation relative to available correlative synoptic data. These cases represented the best examples of cloud streets over both hilly and uniformly flat terrain of the eastern United States and the midwest. For eight of the 24 cloud street cases, sufficient correlative meteorological information was available to allow a more detailed analysis to be completed. These detailed analyses were then compared with existing theories of cloud street development.

A total of 13 wave cloud cases (shown in Table 2-4) were selected from the original data base for further analysis of terrain, associated synoptic conditions, flow direction, average wave lengths, cloud heights, and lateral extent of the wave patterns. As many of the wave cloud cases were found to occur over data sparse areas, detailed comparison with meteorological parameters was limited to six cases. Efforts were concentrated on selecting the optimum techniques for studying wave phenomena using the satellite photographs and conventional surface and upper air observations. In addition, 11 cumulonimbus cloud examples (Table 2-5) were selected for analysis.

2.1.3 Data Handling Procedures

The Landsat imagery used in this investigation was primarily in the 9.5 inch positive paper-print format. Most of the analyses were done using the MSS-5 (0.6 - 0.7 μm) spectral band, since experience has shown that the MSS-5 band is the most useful for observing cloud structures.

The scale of the standard Landsat 9.5 inch paper prints is 1:1 million; however, in an effort to determine the most useful scale for insuring accuracy of the measurement of the various cloud parameters, some reprocessing of the data was performed in ERT's photographic laboratory. For example, two of the cloud street cases, occurring over the New England area, were enlarged to a scale of 1:500,000. Although measurements could be made more easily at this scale, the reprocessing proved somewhat costly considering the amount of data to be analyzed. Therefore, most cloud measurements were made from the standard sized prints using a lighted optical magnifying device. This procedure was

TABLE 2-5

CUMULONIMBUS CLOUD CASES ANALYZED

Date	Image I.D. No.	Location
20 April 73	1271-16234	Missouri
02 August 73	1375-17343	Indiana
06 August 73	1379-16250	Texas
15 August 73	1388-15264	Georgia
17 August 73	1390-15412	Ohio
04 October 73	1438-15074	Off coast of Carolinas
15 April 74	1631-17593	Nevada
26 April 74	1642-15352	Colorado
23 August 74	1761-16382	Texas
25 August 74	1763-15061	Off Georgia coast
26 August 74	1764-15115	Off So. Carolina coast

particularly helpful in the cloud street cases where relatively small-scale measurements were being analyzed. The measurements of the various mesoscale cloud parameters for the images selected for detailed analysis were made on transparent acetate overlays.

In the analysis procedure for each of the mesoscale cloud types, the cloud parameters, such as cloud diameters, cloud spacings and length of the cloud shadows were measured directly from the Landsat images. For computation of the cloud top heights from their shadows, the cloud tops were assumed to be located at the center of the clouds. The heights were computed from the length of the shadows and the tangent of the sun's elevation angle.

2.2 Correlative Meteorological Data

For each Landsat case selected for analysis, correlative surface and upper air data were collected. The meteorological data used in the analysis were chosen based on one or more of the following conditions:

1) The proximity of the reporting station to the location of the cloud feature being studied; the rawinsonde stations used in the analysis were generally within approximately 180 km of the study area.

2) The difference in time between the meteorological observation and the satellite observation; the rawinsonde data were used if recorded within six hours of the Landsat time (since the Landsat observation is at about 1000 in the morning LST, the closest upper air observation in the eastern part of the country was the 1200 GMT (0700 LST) observation).

3) The ability of the rawinsondes to describe accurately the atmospheric conditions at the time of the Landsat observation; if synoptic conditions were changing drastically over the study area and no supplementary rawinsonde data could be located, then the case was rejected for study.

During the course of this investigation, every effort was made to determine the atmospheric conditions at the time of the satellite observation as accurately as possible. In many cases, more than one rawinsonde station was used, and teletype data from both the Service A and Service C networks were used. In addition, surface and upper air facsimile charts were often used, along with historical northern hemisphere pressure charts, to deduce atmospheric conditions. In some instances, nevertheless, the Landsat image covered an area where supporting data were insufficient to permit a detailed mesoscale isobaric analysis.

For each Landsat case analyzed, the synoptic conditions were classified with regard to the general flow pattern. The classification scheme is given in Table 2-6.

In the analysis of mesoscale cloud features in hilly and mountainous terrain, topographic charts were used to determine elevation contours. Charts of a scale of 1:250,000 were found to be useful for comparison with the terrain features visible in the Landsat images.

TABLE 2-6

CLASSIFICATION OF SYNOPTIC CONDITIONS

Code	Description of Synoptic Pattern
WN	Westerly flow, 500 mb jet axis north of Landsat area
WS	Westerly flow, 500 mb jet axis south of Landsat area
WC	Westerly flow, cyclonically curved
WA	Westerly flow, anticyclonically curved
NWC	Northwesterly flow, cyclonically curved
NWA	Northwesterly flow, anticyclonically curved
NW	Straight broad northwesterly flow most levels
NC	Northerly flow, cyclonically curved
NA	Northerly flow, anticyclonically curved
MN	Straight broad northerly flow, meridional circulation
SC	Southerly flow, cyclonically curved
SA	Southerly flow, anticyclonically curved
MS	Straight broad southerly flow, meridional circulation
SWC	Southwesterly flow, cyclonically curved
SWA	Southwesterly flow, anticyclonically curved
SW	Straight, broad southwesterly flow, most levels
CWL	Weak circulation, upper-level flow
CWT	Weak circulation, upper-level trough
CWR	Weak circulation, upper-level ridge
WF	Warm frontal zone over Landsat area
CF	Cold frontal zone over Landsat area
H	Near center of high pressure

3. MESOSCALE CLOUD BANDS

Because a major portion of the investigation of mesoscale cloud features seen in Landsat imagery was devoted to the study of the cloud bands, a review of the theory of formation of this type of organized convection is given. Since Rayleigh's famous 1916 paper on convection currents in a horizontal layer of fluid, cloud bands and associated meteorological conditions have been the subject of several studies. A considerable volume of literature has been reviewed by Kuettner (1971); most of the observational work in this review was based on cloud photogrammetry, aircraft reconnaissance flights and routine surface and upper wind data (Plank, 1966). In the 1970's this material was augmented by radar observations of dry convection (Konrad, 1970; Rowland, 1973; Plank, 1974).

Combining the Rayleigh-Kuettner theory of cloud bands with energy considerations and known properties of cumulus clouds, it is possible to develop a model that enables, in principle, the qualitative prediction of the flow characteristics in heated unstable airmasses from the pattern characteristics of any visible banded cumulus clouds in these airmasses. Through use of this model, detailed meteorological observations are not needed, except for a crude estimate of the average temperature in the layer, which can easily be obtained from either radiometric measurements or climatology. The model can be refined on the basis of statistical relationships among vertically averaged wind speed, wind profile curvature and the maximum wind speed, and the surface wind speed under cloud banding conditions.

Landsat images of cloud bands provide the necessary resolution for the measurements of the smaller cumulus clouds that are seen in marginally stable heated airmasses. The analysis of the cloud pattern characteristics derived from Landsat images and correlative meteorological conditions is described in this section.

3.1 Flow Characteristics Associated with Cloud Banding

Extratropical cloud streets or bands occur mostly in vigorous polar or arctic outbreaks during which the northerly flow is quasisteady. Depending on the horizontal extent of this flow the banded pattern may

be up to a thousand km long and several hundreds of km wide and consist of a large number of individual cloud rows aligned in the direction of the flow. An example of such a pattern is given in Figure 3-1, a Landsat image of the Tennessee area in May.

On days with extratropical cloud street development the vertical wind profile is characterized by small variations of wind direction (less than 20°) with height z and a low-level maximum of the wind speed U about 1,500m above the surface. The wind profile curvature $\partial^2 U/\partial z^2$ is negative; its absolute value varies according to

$$0.3 \times 10^{-7} < \frac{\partial^2 U}{\partial z^2} < 3 \times 10^{-7} \text{ cm}^{-1} \text{ sec}^{-1}$$

while $\partial^2 U/\partial z^2$ (averaged over the layer) is on the order of -10^{-7} cm^{-1} sec^{-1}. This value is an order of magnitude smaller in the tropics. Figure 3-2a shows the curved wind profile.

Cloud streets have a length L on the order of 50 km. The spacing of the bands from axis to axis, λ_y, is 5 to 10 km, of which half or more is clear sky. Along a cloud band the spacing of the individual elements λ_x is of the same magnitude as their diameters. In very moist atmospheres the individual cumulus cells may completely merge to form a solid line. An example of extensive cloud banding is shown in Figure 3-2b.

The depth H of the cloud layer is mostly between 1-1/2 and 3 km though deeper clouds are occasionally observed. Correlation of λ_y with H suggests a rather well defined relationship of the type:

$$\lambda_y = \varepsilon H; \; 2.0 < \varepsilon < 3.0 \qquad (1)$$

The small variation of the wind direction with height in the convective layer and the absence of an Ekman type vertical wind distribution is a result of the configuration of cold surface anticyclones and their associated upper lows west of the belt of strong surface winds. This configuration causes a decrease of horizontal pressure gradient with height and a reversal of this gradient between heights of 2 to 4 km. The resulting thermal wind component would cause the wind to decrease

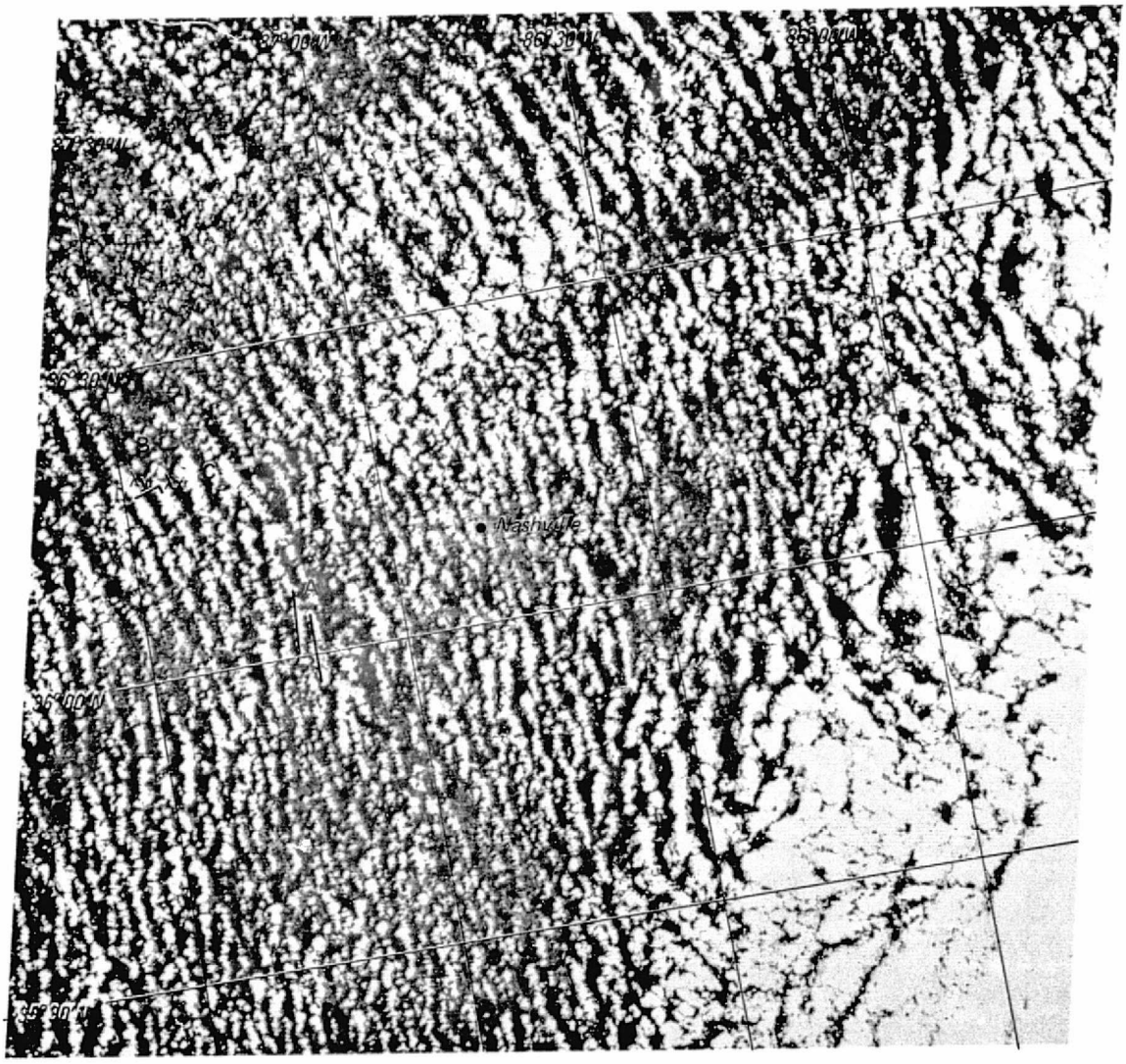

Point A shows two typical cloud streets of moderate length, approximately 25 km. Line B separates an average λ_y measurement. Line C indicates a λ_x distance.

Figure 3-1 Landsat-1 MSS-5 Image (I.D. No. 1284-15552), 3 May 1973, Showing Extratropical Cloud Bands Occurring in Polar Outbreak over Tennessee

609009 609229

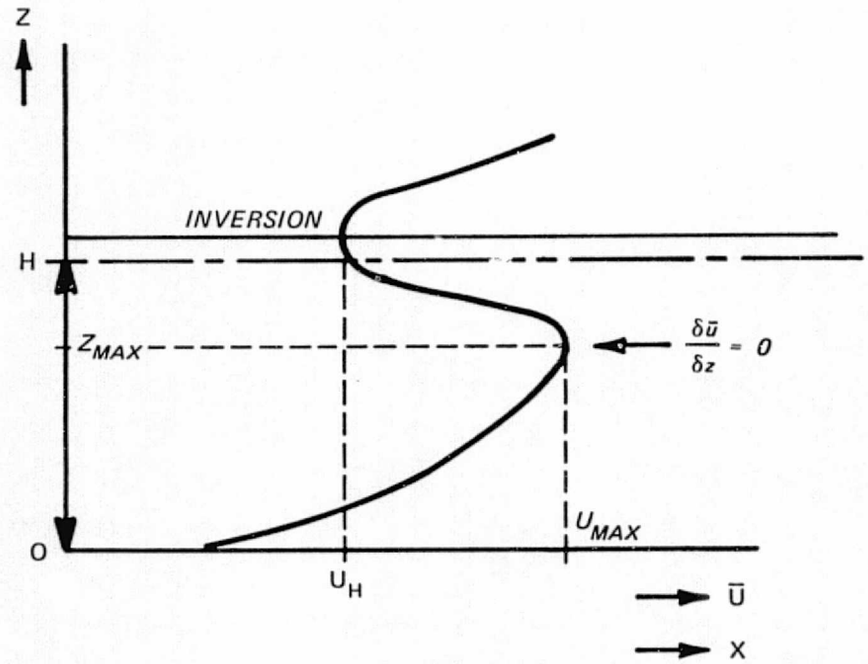

(a)

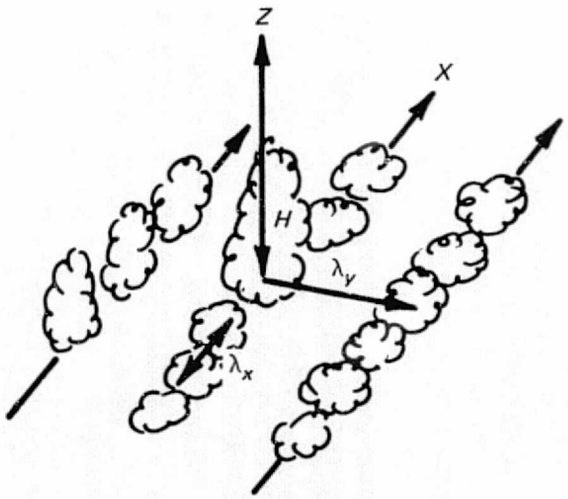

$l = \frac{2\pi}{\lambda_x}$ $m = \frac{2\pi}{\lambda_y}$ $n = \frac{\pi}{H}$

(b)

x shows the direction of flow.

Figure 3-2 Diagram Showing the Variables in Kuettner's Theory of Banded Cumulus Convection: a) Wind Profile, b) Cloud Band Geometry

and back with height, while the frictional component in the boundary layer acts in the opposite way. The balance of these forces causes the wind direction to be more or less uniform with height. The curved wind velocity profile which is regularly observed under these circumstances owes its existence to a wind increase with height dominating the lower portion of the convective layer and a thermal wind decrease with height which is prevalent in the upper portion, again under balance of forces. These conditions are reasonably well met under the semisteady state of the synoptic-scale flow.

As discussed by Kuettner (1959), cloud banding is often associated with relatively strong winds in a rather shallow convective layer. In southerly flows originating over relatively cold water, cloud streets may form 50 to 100 km inland. In those cases, the vertical wind profile shows less uniformity both in curvature and wind direction. Near the tropics, banded cloud patterns sometimes form in weak windfields. Also, Kuettner points out that cloud streets propagate upwind, and that 95 percent of the time their orientation relative to the direction of the average wind in the layer is between -30° and +30°. The elements in the street drift faster than the street itself, and the life cycle of an individual cloud street is on the order of an hour.

The vertical temperature lapse rate in the convective layer is close to dry adiabatic throughout its depth, and the layer is topped by an inversion. Since the underlying surface is much warmer than the air, convection below the clouds is well organized. The flow pattern inside cloud streets, though, has not yet adequately been measured and quantitative information about the downwind motions in the cloud-free regions is nonexistent. Theory suggests helical motions with horizontal divergence towards both sides of the upper portion of the cloud streets. The symmetrical inflow underneath the cloud base which was expected to show up in the surface wind pattern has so far eluded detection, perhaps because it is masked by the greater degree of intensity which characterizes the small-scale mechanical turbulence and dry convection in the sub-cloud layer.

Individual cloud streets may be generated by heat sources and sources of moisture (mountains, towns, warm lakes and the like), whereas multiple cloud streets are disturbed by irregularities in the topography.

They are best organized over oceans, polar ice caps in summer, and in the trade-wind regions. Dry "cloud" street circulation patterns are found under the same conditions when moisture is lacking (Konrad, 1970).

A more thorough discussion of the theory of formation of mesoscale cloud bands, including mathematical derivation of the perturbation equations, the relationships between cloud band geometry and average buoyancy, and boundary conditions for cloud bands over sea surface, is given in Appendix A. In order to avoid a rigorous mathematical discussion, any future references made to equations or their related parameters will assume the derivations given in Appendix A.

3.2 Landsat Cases Selected to Study Cloud Bands

From the overall Landsat data sample discussed in Section 2, images displaying mesoscale cloud bands were selected for detailed analysis. These cases, as well as the cases displaying terrain-induced cloud patterns and other mesoscale features discussed in later sections, were initially classified with regard to the synoptic scale surface and upper air patterns. The classification scheme is shown in Section 2.2.

The Landsat cases for which mesoscale cloud bands were analyzed are listed in Table 3-1 according to date, location, terrain type, and synoptic flow pattern; the measured cloud parameters listed in the table are the parameters discussed in Section 3-1; e.g., the spacing of cloud elements in a cloud band and the spacing between the bands. The measurement of these parameters is discussed in the following section. The meteorological conditions associated with these cases are discussed in general in Section 3.4; the analysis of three selected cases is discussed in detail in Section 3.5.

Typical mesoscale cloud band patterns analyzed in this study are shown in Figures 3-3 and 3-4. The Landsat-1 image of 22 April 1974 shown in Figure 3-3 views the area of the Carolina coast. The cloud bands observed in this image are located over the flat terrain of the coastal plain. Also, the sharply defined easternmost limit of the cloud band pattern marks the inland extent of a localized sea breeze.

TABLE 3-1

CLOUD STREET PATTERN CHARACTERISTICS IN RELATION TO TERRAIN AND CIRCULATION TYPES

Date	Location	Time (GMT)	Terrain	Synoptic Type	Flow Direction	Ave. Length (km)	Ave. Range (km)	Parameters		
								λ_x (km)	λ_y (km)	H (km)
7/31/72	VA	15.19	Hilly	-	-	40	30-50	1.5	2.0	-
6/17/73	MA, RI	15.04	Hilly	NWC	N	50	40-60	1.9	4.1	2.1
8/7/73	OH	15.41	Hilly	CWT	NW	12	10-15	2.0	3.0	1.4
8/2/73	IN, TN, AL, MS	15.59	Flat	WC	WSW	40	20-50	1.4	3.0	4.0
8/24/73	Houston, TX	16.24	Flat	CWR	SSW	28	20-50	1.4	2.5	2.1
5/3/73	TN	15.55	Hilly	NWC	NW	33	15-70	1.8	3.8	2.5
5/3/73	KY	15.55	Hilly	NWC	NW	67	40-120	1.4	4.5	5.8
5/3/73	TN, AL	15.55	Hilly	NWC	NW	29	15-55	1.4	3.0	1.8
5/3/73	KY	15.55	Hilly	NWC	NW	51	20-110	2.2	3.8	-
7/20/74	NY	15.00	Hilly	WC	N	45	40-70	2.5	4.1	1.8
1/17/74	ME Coast	15.00	Sea	WC	N	95	80-100	2.3	3.9	1.4
8/21/74	central TX	16.00	Flat	SA	S	19	5-40	1.0	3.0	1.7
4/22/74	NC	15.00	Hilly	SWA	SW	32	10-70	2.5	4.0	1.6
4/22/74	NC coast	16.00	Flat	SWA	SW	43	40-100	2.7	4.0	1.6
8/22/74	MN	16.28	Flat	CWT	NW	45	20-80	1.0	4.0	-
7/18/75	LA	16.00	Flat	SA	S	27	20-45	1.8	4.2	1.7
6/30/75	MI	16.00	Hilly	SWA	SW	74	60-80	1.7	3.1	1.2
6/30/75	WI	16.00	Flat	NWC Front	NW	74	40-100	1.0	1.2	1.4
7/3/75	KS	16.00	Flat	SA	SE	30	20-50	2.0	2.5	1.0
7/12/75	OH	16.00	Flat	NWC	NW	30	30-50	3.5	8.0	4.2
7/18/75	east TX	16.00	Flat	SA	S	39	20-30	1.5	2.6	1.1
7/4/75	OK	17.00	Flat	CWR	SE	45	20-60	1.5	2.5	1.4
7/4/75	SW TX	17.00	Flat	SA	S	33	25-60	1.8	4.2	1.6
7/4/75	central TX	17.00	Flat	SA	S	18	5-40	2.0	2.5	1.5
7/4/75	SE TX	17.00	Flat	SA	S	30	8-35	2.0	2.5	1.3
7/3/75	ME	15.00	Hilly	CF & NWC Front	NW	25	10-40	1.8	2.5	_
7/3/75	KS	16.00	Flat	SA	S	32	10-50	2.0	2.5	1.0
7/25/75	FL	15.15	Flat	CWR	N	20	10-30	1.4	4.2	1.6

λ_x is the spacing of the cloud elements in a row

λ_y is the spacing of the rows

H is the height of the cloud tops above the surface

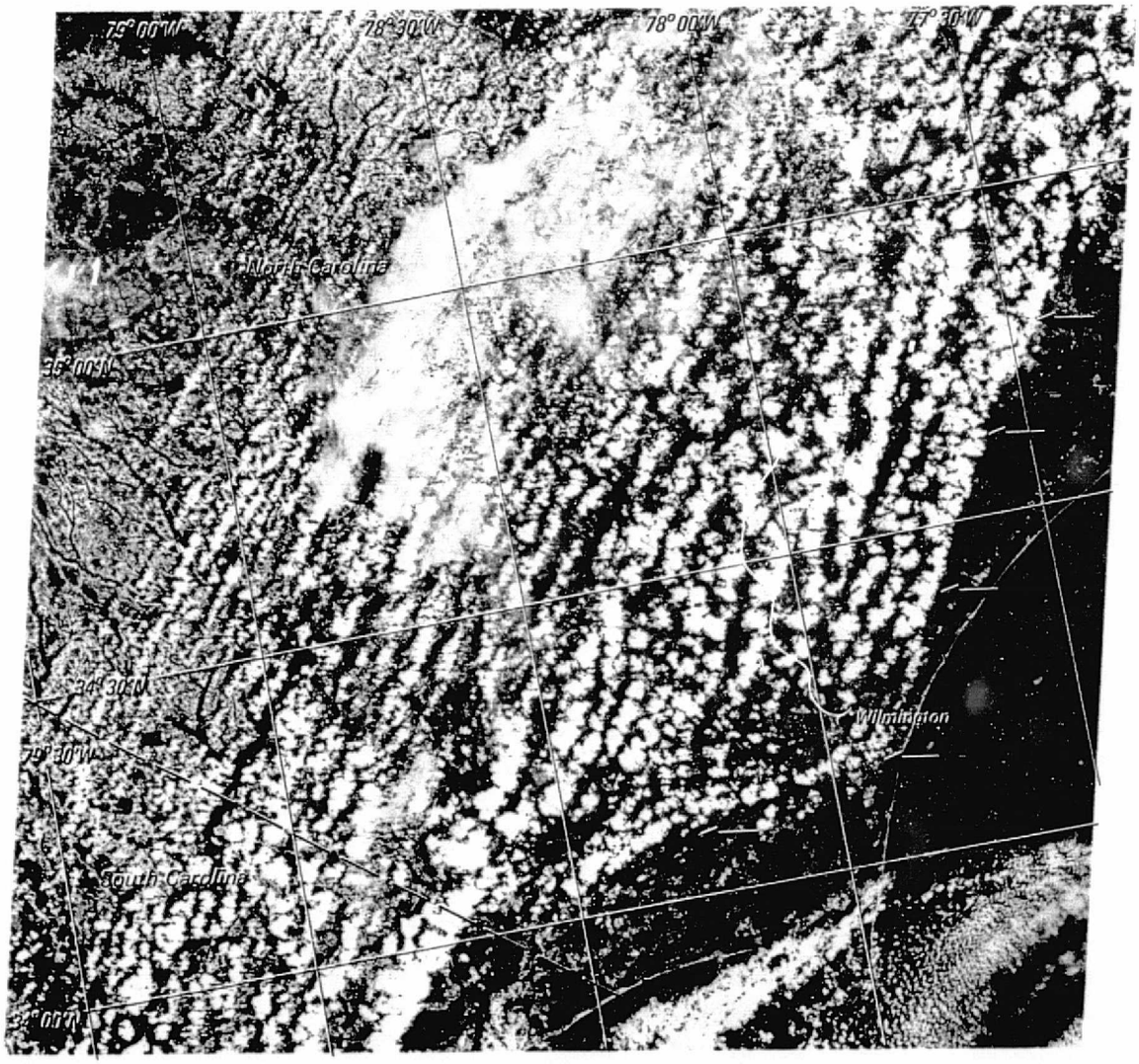

Arrows indicate the sharply defined easternmost limit of the cloud band pattern, marking the inland extent of a localized sea breeze.

Figure 3-3 Landsat-1 MSS-5 Image (I.D. No. 1638-15150), 22 April 1974, Showing Cloud Band Located over the Flat Terrain of the Carolinas' Coastal Plain

609006
609228

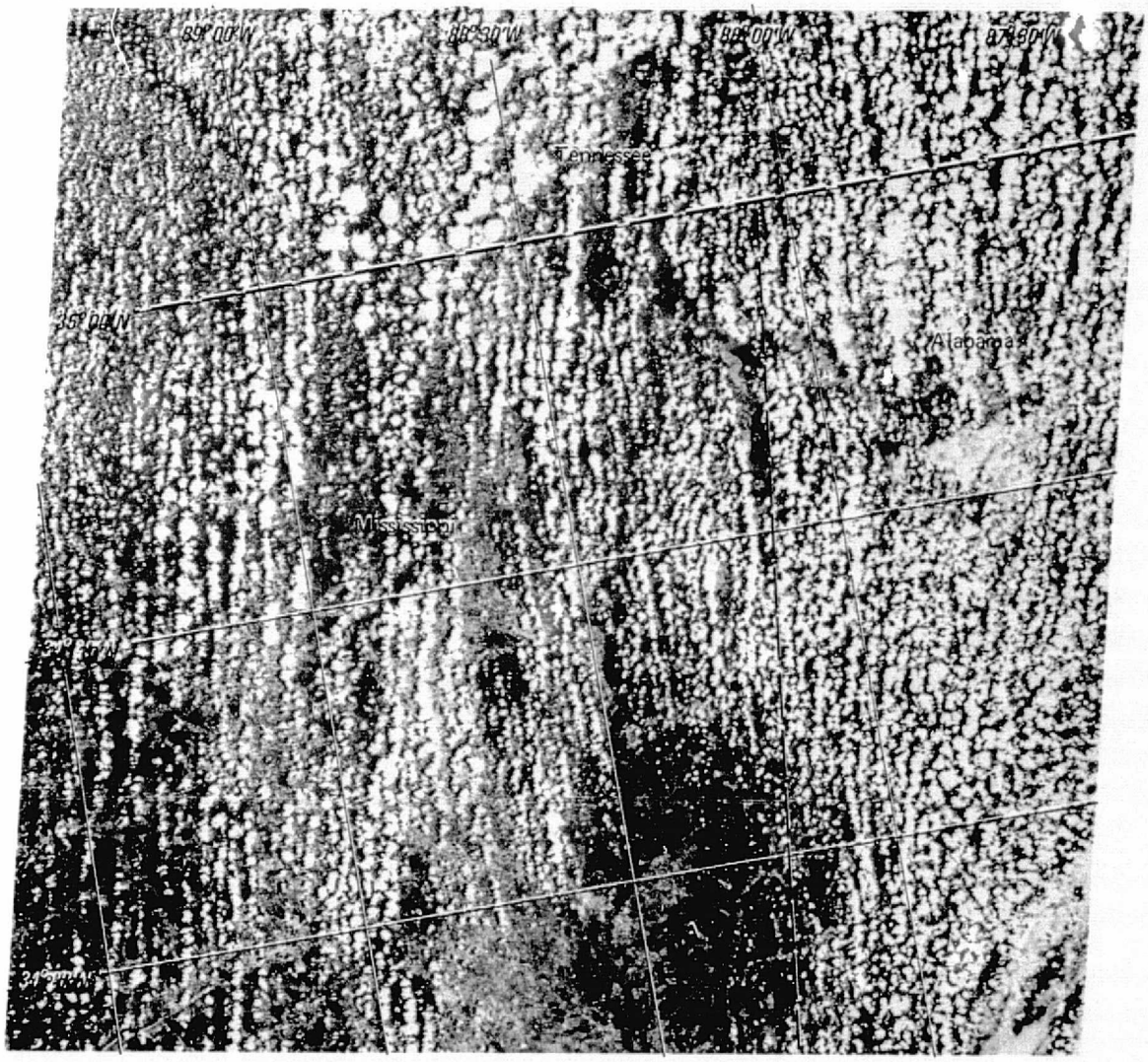

The cloud-free Point A near the bottom-center of the frame is flatter terrain at lower elevation, north of Columbus, Mississippi.

Figure 3-4 Landsat-1 MSS-5 Image (I.D. No. 1375-16003), 2 August 1973, Showing Cloud Bands Located over the Mostly Hilly Terrain of the Tennessee, Alabama and Mississippi Border Region

The example shown in Figure 3-4 is the Landsat-1 image of 2 August 1973 viewing the border region of Tennessee, Alabama and Mississippi. The cloud bands observed in this scene are located over mostly hilly terrain. The cloud-free area near the bottom center of the frame is flatter terrain north of Columbus, Mississippi.

3.3 Measurement of Cloud Band Parameters

Cloud parameters, such as the spacing of bands and cells, cell diameter and cloud top height, were measured from the satellite images using the procedures described in Section 2. To determine cloud height, it was found that during the summer and over low latitudes, the elevation of the sun was often close to 60 degrees. The geometry of the incident radiation upon simple pyramidal, trapezoidal, and rectangular cloud models shows that measurements of the length of the cloud shadows, whether taken from the center or from the edge of the cloud, are subject to error, unless the cumulus tower closely resembles a cone of which the angle between the diameter of the base and slant height is equal to or larger than the sun's elevation. The error increases with departure from a pyramidal or conical shape and with increasing diameter to depth ratio.

Despite the difficulties in measuring cloud height, analysis of the measured cloud parameters revealed that, in most instances, increases in the spacing between cumulus cells in a cloud band correlate well with increases in cloud depth and spacing between cloud bands. The ratio of the band spacing to the cell spacing remained generally between 1.2 and 2.5, and the ratio of band spacing to cloud depth remained usually between 2 and 3. This latter ratio agrees well with that indicated by Kuettner (1959, 1971), Konrad (1968), and Angell et al (1968). Where the theoretically derived and observationally confirmed ratio of cloud street spacing to layer depth ($2.0 < \lambda_y/H < 3.0$) was not found, the computed cloud top heights were assumed to be in error and omitted from the analysis. Instead, H was set at $0.4\ \lambda_y$ (where H is the cloud layer depth and λ_y the cloud street spacing).

Information from the nearest rawinsondes was used to deduce the average temperature $\overline{T}$, the vectorially averaged wind direction $\overline{D}$, and the wind speed $\overline{U}^{H}$ over the depth for the conditionally unstable layer.

This depth was also compared with the cloud top heights determined directly from the Landsat images.

Careful analysis of the pressure field over the viewed area was attempted where possible. A problem experienced with almost all cases was a lack of the detailed meteorological data needed to obtain accurate mesoscale analysis; in many cases, therefore, cloud characteristics had to be compared with flow characteristics from rawinsondes a considerable distance away in both space and time. Conventional ground truth is often not adequate to obtain the necessary information for accurate comparisons with the detail that can be mapped from Landsat images.

3.4 Summary of General Meteorological Conditions Associated with Cloud Band Patterns Observed in Landsat Data

The review of numerous Landsat-1 and Landsat-2 images of 1973, 1974 and 1975 has provided some 25 excellent examples of low-level convective cloud band (street) patterns located over various regions of the United States, extending from the East Coast to the Midwest. Of this data sample, 24 occurred during the late spring or summer months; the exception was a wintertime occurrence off the Maine coast where cold Arctic air was being transported over warmer ocean water.

Examination of the late spring and summer meteorological conditions associated with the cloud street patterns has shown two generally preferred synoptic patterns, one for the region of the northeastern and north central part of the country, and an entirely different pattern for the region of the Southeast and Gulf Coast states.

The cloud street cases located over the North were almost entirely associated with the injection of cooler, dryer, unstable polar air following recent cold front passage at the surface and a trough located just east of the cloud bands at 850 mbs. The wind profiles were characterized by slight variations of wind direction (less than 20°) with height and a low-level maximum wind speed near the 850 mb level. The configuration of cold surface anticyclones to the west of the cloud streets and the upper-level lows just to the north and east suggest an overall decrease of pressure gradient with height and a reversal of this gradient near the 700 mb level. These findings are in agreement with earlier observations summarized by Kuettner (1971).

The associated horizontal temperature gradient (thermal wind) across the flow would make the wind back with height, but friction in the boundary layer would cause the wind to veer with height. The balance of these forces causes the wind direction to be more or less uniform with height. The curved wind profiles owe their existence to a frictional wind increase with height dominating the lower portion of the layer and a thermal wind increase with height which is prevalent in the upper portion, again under balance of forces.

Cloud street patterns observed in the Landsat images from the Southeast and Gulf Coast states during the spring and summer seasons were associated with an entirely different meteorological regime. In these instances, a south to southwesterly flow of moist maritime air located at the trailing edge of surface anticyclones was the predominant meteorological regime. Once again, examination of the vertical wind profiles revealed curvature with a low-level maximum wind near the 1,500m level and only slight variations in direction with height. Also, a steady decrease in moisture with height was evident, suggesting that dryer air associated with the upper-level anticyclones located to the east was being transported westward over the moist surface layer.

Analysis of the vertical temperature lapse rate in the convective layer for both the northwesterly and southerly wind flow regimes shows that it is close to dry adiabatic throughout its depth. The convective layer was topped by drier and more stable air. In about half of the cases, the transition was sharp and accompanied by a subsidence inversion. Since the underlying surface was much warmer than the air, convection was well organized.

Depending on the horizontal extent of the low-level flow, banded cloud patterns were found to extend up to a thousand km along the direction of the mean wind. The width of the cloud street pattern was up to several hundred km. The individual cloud rows which were sometimes found to be more than 100 km long were aligned in the direction of the flow with the cells propagating upwind.

The analysis of three selected cases of cloud banding is presented in the following section.

3.5 Case Study Analysis of Mesoscale Cloud Bands Seen in Landsat Images

3.5.1 Case 1: Southern New England, 17 June 1973

A Landsat image, displaying conspicuous cloud banding at 1500 GMT over Massachusetts, Connecticut and Rhode Island, is shown in Figure 3-5. The cloud bands occurred in a strong north to northeast flow between a large high pressure area over northeastern Canada and a low over Newfoundland. The depth of the convective layer varied from 700m above the terrain near Kennedy Airport to 1,500m near Portland, Maine (see composite upper air soundings in Figure 3-6). The diameters of the individual cumulus elements ranged from 500m in areas of incipient moist convection to 3,000m in the deepest parts of the cloud layer. The corresponding spacing of the cloud bands ranged from 500 to 8,000m.

Over most of the terrain the cloud streets preserved their general characteristics, except in the region over the Berkshire Mountains which extended throughout almost the entire depth of the convective layer and caused disfigurations with a more or less dappled appearance. Distortions of the cloud pattern also occurred over the Boston area, probably as a result of a sea breeze effect. Note that where the flow was perpendicular to the coastline, small cloud streets merged into larger ones. Over most of the area, the alignment of the cloud bands was not exactly parallel. Where individual elements grew larger and λ_x increased, cloud bands tended to diverge, thereby conserving a quasi constant ratio of λ_y/λ_x. The cloud street characteristics for this case are summarized in Table 3-2.

Problems encountered in determining the depth of the convective layer for this case were twofold. Since the elevation of the sun was 61 degrees, and the length of the shadow was measured from the center of the cloud element to the shadow's edge, the height of the cloud tops was overestimated. Comparison of the ratio H/λ_y deduced from rawinsonde data (Table 3-2) with Equation 1 (Section 3.1) suggests that over land, the depth of the cloud layer may have been underestimated by the soundings which were taken mostly over coastal stations. Only one of the four soundings, namely Albany, was taken over land, but it was taken on

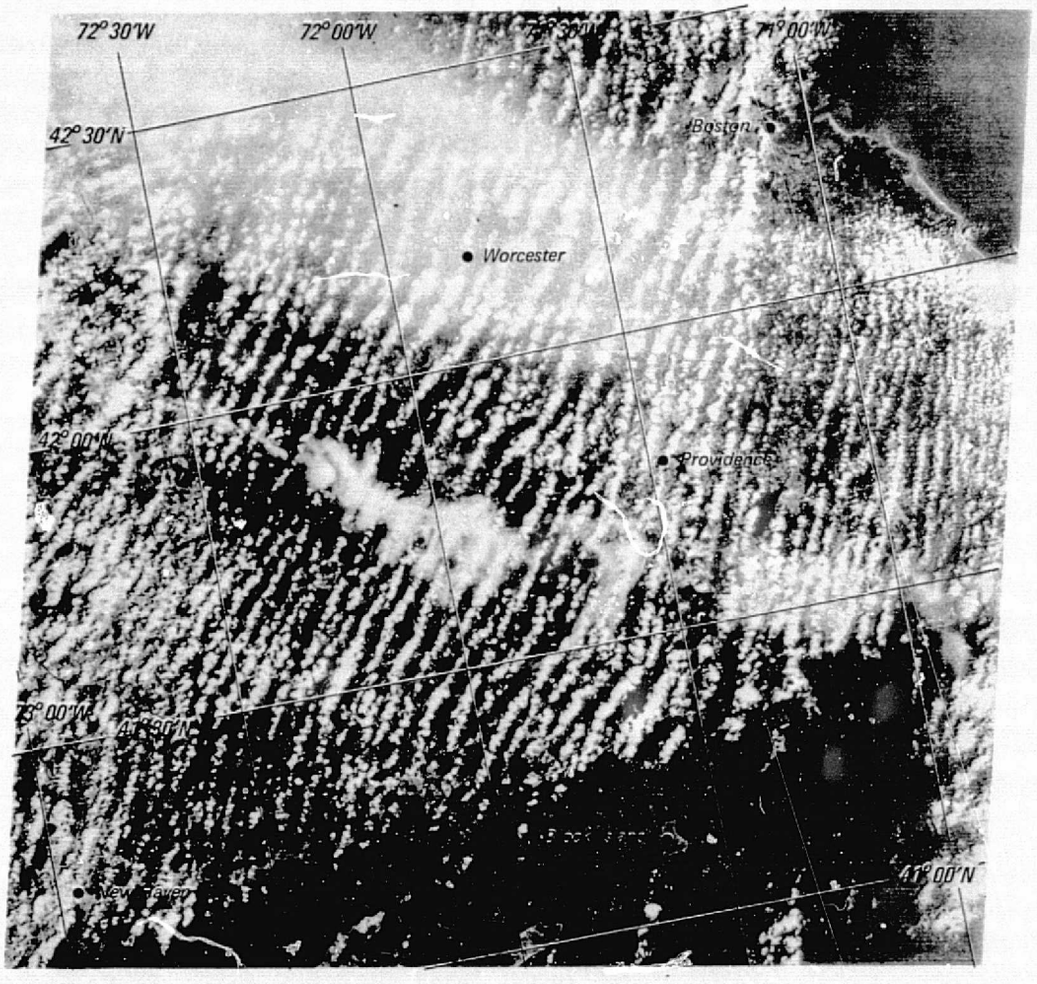

Figure 3-5 Landsat-1 MSS-5 Image (I.D. No. 1329-15014), 17 June 1973, Showing Cumulus Cloud Banding over Southern New England

609006
609224

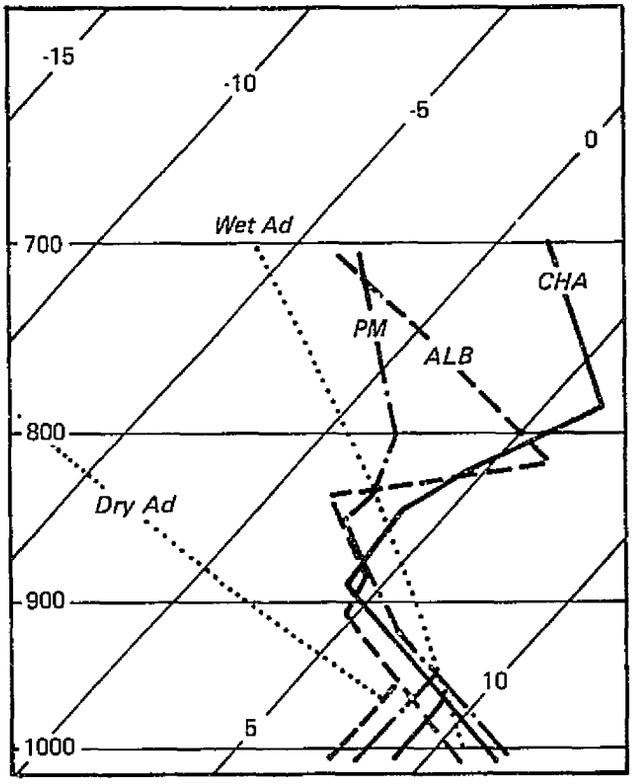

ALB is Albany, PM is Portland and CHA is Chatham, Mass.
Pressure is in mbs and temperature in °C.

Figure 3-6 Upper Air Soundings, 17 June 1973, at 0600 GMT

TABLE 3-2

CLOUD STREET CHARACTERISTICS, 17 JUNE 1973 CASE

Range	Parameters					Comparative Ratios		
	$\overline{D}$ (deg)	λ_x (km)	λ_y (km)	H_s (km)	H (km)	$\frac{\lambda_y}{\lambda_x}$	$\frac{\lambda_y}{H_s}$	$\frac{\lambda_y}{H}$
Average	35	1.9	4.1	1.3	2.1	2.1	3.1	1.8
Maximum	55	3.0	8.0	1.5	3.6	2.5	5.3	2.2
Minimum	20	0.4	0.5	0.7	0.9	1.2	0.7	0.6

TABLE 3-3

COMPARISON OF FLOW PROPERTIES COMPUTED FROM

CLOUD CHARACTERISTICS WITH GROUND TRUTH; 17 JUNE 1973 CASE

Range	Parameters						
	$\overline{D}$ (deg)	$\overline{D}^{H}_{obs}$ (deg)	D_{geo} (deg)	$\overline{U}^{H}$ ($m\ sec^{-1}$)	$\overline{V}^{H}$ ($m\ sec^{-1}$)	V_{geo} ($m\ sec^{-1}$)	V_{max} ($m\ sec^{-1}$)
Average	35	(15)	(25)	19.3	(14)	(13)	(17)
Maximum	55	(19)	(40)	23.0	(17)	(16)	(19)
Minimum	20	(7)	(10)	-	(10)	(11)	(12)

the western side of the Berkshires where the flow was weaker and probably not representative. Despite these regional differences, each of the four rawinsonde stations reported a curved vertical wind profile with low-level wind speed maxima in the upper part of the cloud layer.

Comparison of the alignment of the cloud bands with the direction of the average wind in the layer shows a deviation of the cloud band direction 15 degrees to 30 degrees east of the mean wind (Table 3-3) but less than 15 degrees to the right of the direction of the geostrophic wind. It should be noted that the wind profiles at the four rawinsonde stations were reported at 1200 GMT whereas the time of the pressure analysis (V_{geo}, in Table 3-3) coincides with that of the Landsat observation at 1500 GMT.

The average wind speed, $\overline{U}^H$, computed for the data in Table 3-3 using the equations and the assumptions discussed in Appendix A, is compared with the average wind speeds at the rawinsonde stations and the geostrophic wind in Figure 3-6. In this case, the modified Kuettner model systematically overpredicted the vertically averaged wind speeds. Possible reasons for this discrepancy are the uncertainties in the assumed wind profile, characterized η, the instability β and the depth H of the convective layer as discussed in Appendix A. For the smallest cloud streets, Equation 3 (see Appendix A) did not have a solution; these cloud bands were probably still in the growing stage.

3.5.2 Case 2: New York - Pennsylvania, 30 July 1974

Another case of cloud banding is shown in Figure 3-7. In this case both banded cloud patterns and solitary mountain-wave-induced cloud rows were observed in the same layer. Cloud band patterns are most conspicuous north of Utica and over the hills of southwestern New York state and northeastern Pennsylvania. Skies are completely clear over the Hudson River valley and the Catskill Mountains; extensive cloud cover exists over the Massachusetts-Vermont Berkshires and north of Albany, but these clouds are rather poorly organized.

The cloud banding in this case occurred in a northerly low-level flow between a high over central Canada and a low over Nova Scotia. According to the soundings from Buffalo, Albany, Portland, Maine and New

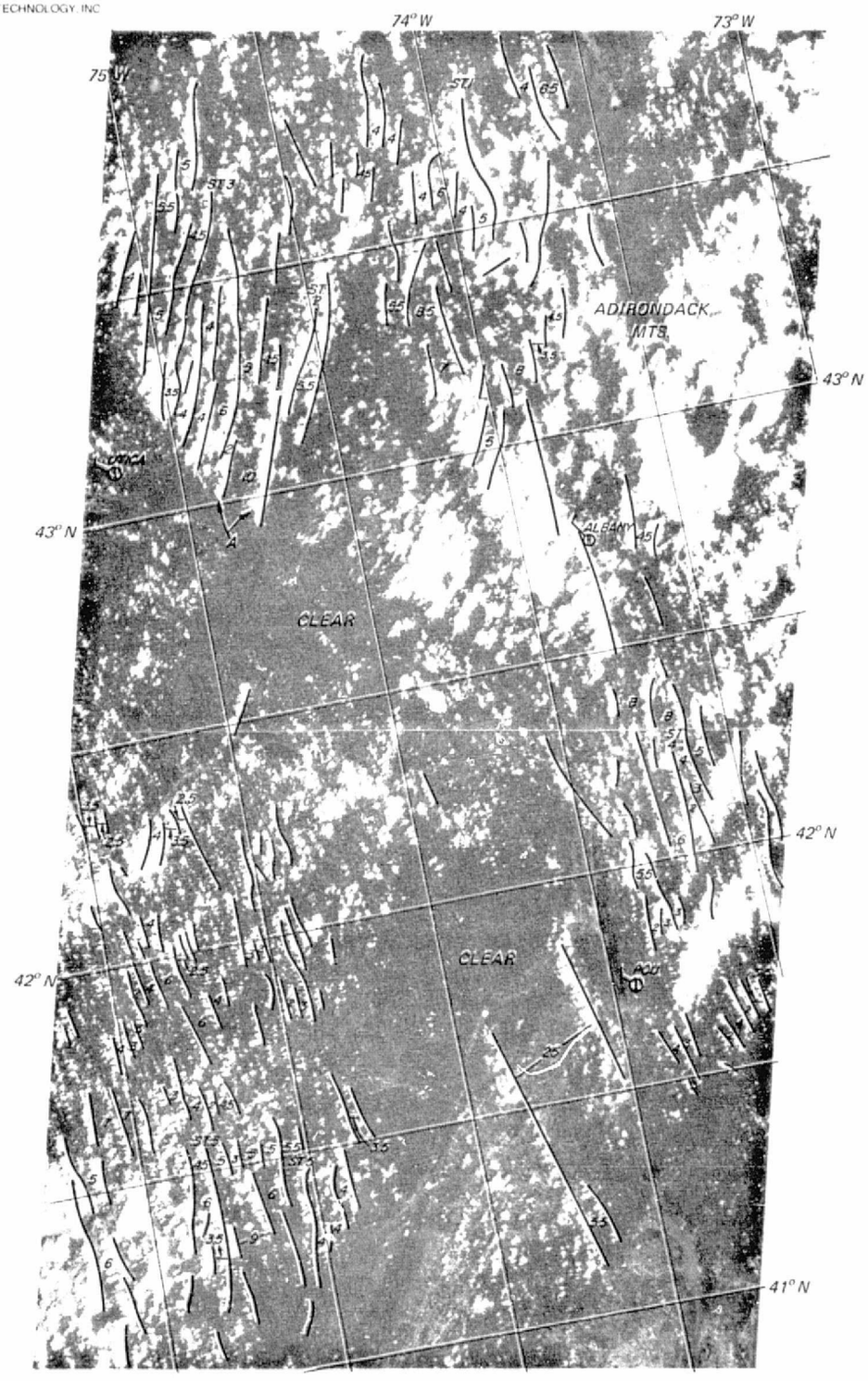

Point A shows sharp end to the mechanically-induced cloud streets as they near the valley plain. Numbers indicate distances between cloud streets, in kilometers.

Figure 3-7 Landsat-1 MSS-5 Images (I.D. Nos. 1727-15041 and 1727-15043), 20 July 1974, Showing Cloud Banding, as well as some Cloud Rows that Appear to be Terrain-induced, over the New York and Pennsylvania Area

609004
609003

York City, the unstable layer was 2 to 3 km deep. The winds over Albany (near the cloud streets) unfortunately were not reported. Elsewhere none of the available wind profiles shows the unidirectional flow with a low-level wind maximum required by the Rayleigh-Kuettner theory. Instead, the winds were steadily backing with height from north to west with maximum speeds between 40 and 50 knots, well above the 500 mb level. The lack of curvature in the vertical wind profile suggests values of U'' (see Appendix A) close to zero and even positive, allowing no steady-state solutions to support the theoretical results of Equation 3. Yet, in the real atmosphere, cloud banding was evident. Assuming that wind profiles with positive curvature may have been present locally in the areas of conspicuous cloud banding, one would arrive at the results presented in Table 3-4. As can be expected, on the basis of the reported vertical wind profiles, there was fairly poor agreement between wind direction and speed predicted by the Rayleigh-Kuettner theory and ground truth.

Generally, the alignment of the cloud streets departed considerably from that of the geostrophic wind (Figure 3-8). In some places, the cloud streets ran almost perpendicular to the isobars. In fact, except for the region north of Utica, the agreement between the direction of the surface wind and the orientation of the cloud streets is much better than the agreement of cloud orientation with any other winds. Note that major assumptions in the Rayleigh-Kuettner theory were not justified in this case, namely uniform terrain, unidirectional flow and a low level wind maximum. Also, there is some evidence that the mechanisms that triggered the convection were not uniform either.

In the cloudy regions over high ground, cumulus convection seemed to be rooted in the planetary boundary layer where wet bulb potential temperatures and convective condensation levels ranged from 15°C and 900m in the Adirondacks to 17°C and 1,200m over southwestern New York state and northeastern Pennsylvania. The soundings of Buffalo and Albany suggest that in those regions, cloud bases were above the level of free convection (850 mb, 10°C) for the areas in which the radiosondes were released. In the lower parts of New York state, where the wet bulb potential temperature varied between 13° and 15°C, dry convection did

TABLE 3-4

COMPARISON OF FLOW PROPERTIES DERIVED FROM CLOUD STREET CHARACTERISTICS WITH GROUND TRUTH

20 JULY 1974 CASE

Cloud Street	Parameters									
	L (km)	H_s (km)	λ_x (km)	λ_y (km)	$\bar{D}$ (deg)	D_{geo} (deg)	D_{850} (deg)	$\bar{U}'$ ($msec^{-1}$)	V_{geo} ($msec^{-1}$)	V_{850} ($msec^{-1}$)
1	42	1.7	2.6	4.2	360	360	350	14.8	12.0	13.0
2	35	1.8	2.4	5.0	030	355	350	17.1	12.0	13.0
3	57	1.9	2.8	4.4	025	340	350	17.0	12.0	13.0
4	42	1.5	2.8	5.6	355	350	350	13.0	20.0	13.0
5	42	1.6	1.6	4.2	005	010	350	16.0	21.0	15.0
6	32	1.5	1.1	5.0	360	350	350	21.0	21.0	15.0

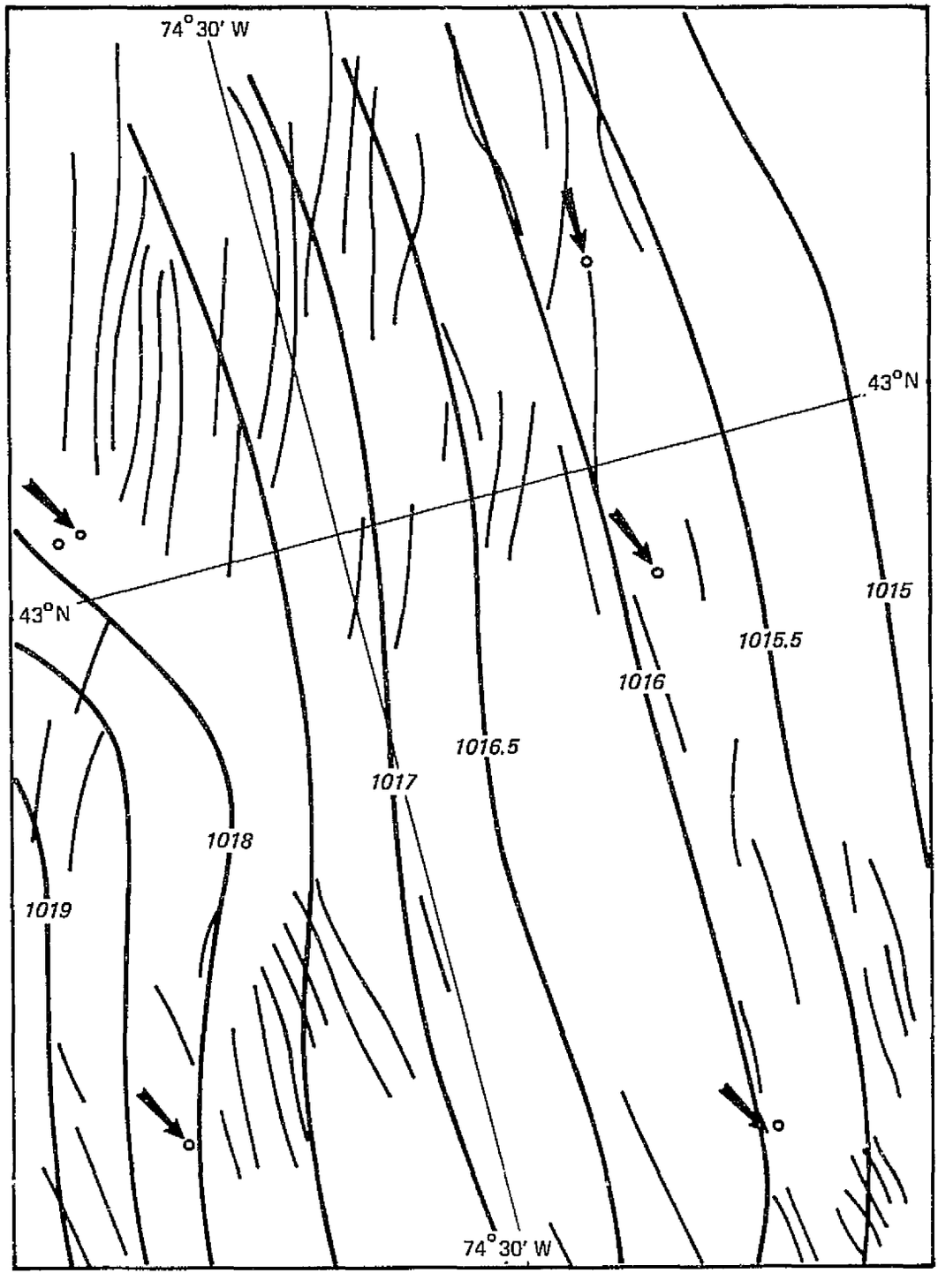

Pressure is in mbs. Arrows indicate the direction of the average wind in the unstable layer.

Figure 3-8 Diagram Showing the Relationship between Alignment of Cloud Bands in Figure 3-7 and Surface Isobars, 20 July 1974 at 1500 GMT

609120

not reach that level, and the sky remained clear except for two conspicuous cloud rows that seemed to be triggered by two peaks in the Catskills. Lakes to the west of these peaks could have provided the necessary moisture for the cloud development.

The height of the cloud tops in the Catskills area, computed from their shadows, was 2,300m, and the cloud base was determined to be at 1,200m. The sounding of Poughkeepsie, near the cloud streets, indicated that any convection over that area would have to be triggered either by a heat source or by mechanical lifting. Since the mountain peaks are 800 and 900m high, both conditions were easily fulfilled. Subsequent cumulus clouds forming the 70 km cloud street rows were clearly not rooted in the boundary layer and must have been induced by gravity-inertial waves. A full discussion of wave clouds is given in Section 5.

The mountain-wave approach, applicable only for statically stable atmospheres, would provide the cloud and airflow characteristics found in Table 3-5. The geostrophic wind V_{geo} and the 850 mb wind are tabulated for comparison. A complication here is that the atmosphere was absolutely stable with respect to surface-induced convection, but conditionally unstable with respect to mountain-induced heating, and absolutely unstable with respect to lift above the level of free convection. Because of the ambiguity in the choice of either upward buoyancy force, $g\beta$, or gravitationally (restoring) force, $g\sigma$, dictated by the Rayleigh-Kuettner and mountain wave models, respectively, the hybrid-wave-convective clouds near Poughkeepsie are unsuitable for wind computation by simple techniques. However, where conspicuous isolated cloud streets or wave trains coexist with the more common banded low-level cumulus patterns, the atmosphere is probably marginally unstable with respect to deeper convection.

3.5.3 Case 3: Coastal Maine, 17 January 1974

A Landsat image displaying cloud bands developing over the ocean off the coast of Maine in the winter is shown in Figure 3-9. At the time of this satellite observation, cold arctic air was flowing southward at the eastern flank of a massive area of high pressure centered over the Hudson Bay. Over land, the air was relatively clear, but 10 to

TABLE 3-5

CLOUD AND AIRFLOW CHARACTERISTICS

20 JULY 1974 CASE

λ(m)	Parameters			
	$\sigma(m^{-1})$	$\bar{U}(m\ sec^{-1})$	V_{geo} $(m\ sec^{-1})$	$V_{850\ mb}$ $(m\ sec^{-1})$
3,000	1.4×10^{-5}	5.6	12	10
3,600	1.4×10^{-5}	6.7	12	10

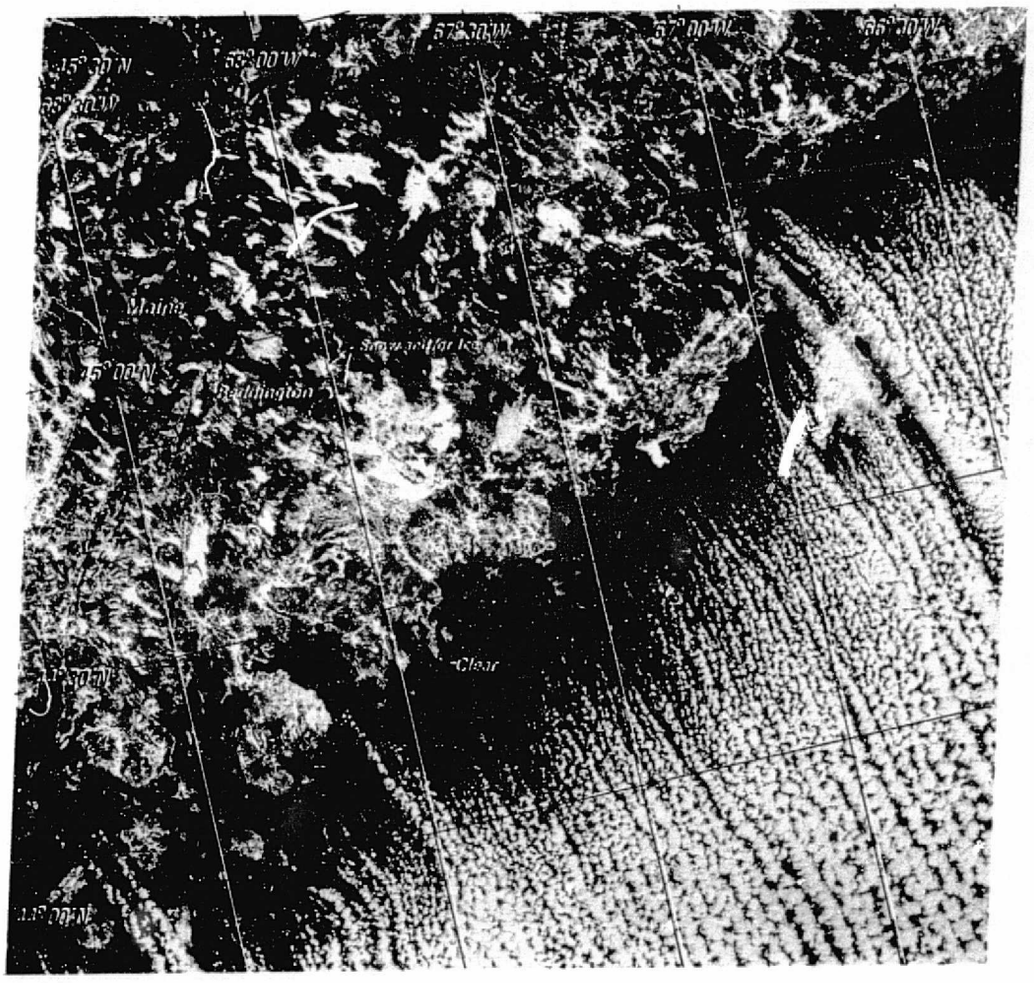

Figure 3-9 Landsat-1 MSS-5 Image (I.D. No. 1543-14453), 17 January 1974, Showing Cloud Bands Developing over the Ocean off the Coast of Maine

15 km away from the coast of south Maine, bands started to develop over open water. The air left the continent with temperatures close to -10°C whereas the water temperature, according to the Marine Climatic Atlas of the World, could have risen from 0°C near the coast to 5°C at positions near the bottom right of the photograph. Surface wind reports from two ships near the area indicate wind speeds on the order of 15 knots. Under these circumstances, a large heat flux develops upwards from the sea surface.

The large-scale flow pattern was steady enough to allow space-to-time conversion. The Landsat image, therefore, can be viewed as depicting the growth of convection from small wisps of cumulus via closely packed narrow cloud streets into large bands of well developed cells during a time span on the order of one-half hour. Whereas most cloud bands were 3 to 5 km apart and of the same size, a pattern of larger and longer cloud rows with spacings of 20 to 40 km seemed to be superimposed.

Closer inspection of the satellite image reveals two dominant modes of cloud band growth, namely either increase in size and spacing of existing bands, or merging of smaller bands into larger bands. In about 16 locations, pairs of cloud streets seemed to move farther apart though their elements grew only slowly. At a critical spacing λ_y, for which λ_y/λ_x is about 2.5, a third cloud street developed in the clear space between the first pair. Only on three occasions did the reverse happen.

In 25 of the bands, two cloud streets merged into one; this occurred mostly during the initial stages of development. In seven bands, the middle cloud street disappeared after the elements in the two adjacent streets had grown to twice their original size. As a result of this growth, the ratio λ_y/λ_x jumped in several places on the image from less than 2.0 for three adjacent cloud rows to about 3.0 for the remaining pair. For the longest bands, which showed more or less steady-state conditions, λ_y/λ_x varied only from 1.4 to 1.7. These were assumed to fulfill the conditions under which the assumptions for the Rayleigh-Kuettner model are justified. Since the depth of the cloud rows could not be determined from the Landsat photograph, λ_y/H was assumed to be 2.5 for the purpose of wind speed computations.

The results are incorporated in Table 3-5. Though an average wind speed of 7.5 m sec^{-1}, combined with a surface wind parameter of 5 m sec^{-1}, compares favorably with the ship reports, direct verification of the flow characteristics within the area with cloud bands was not possible. In Appendix A, statistical relationships are proposed that may improve estimates of wind speed in the convective layer over open sea.

3.6 Discussion of Results of Cloud Band Analysis

The results of the detailed analysis of the three cases discussed above and of other cases are summarized in Table 3-6. This table presents the cloud pattern characteristics in relation to terrain features and circulation types. Cloud street measurements are averaged over the area covered by the photographs; bars indicate averages over the depth of the convective layer. Frequency distributions of cloud street length L, spacing λ_y and ratio of λ_y/λ_x are shown in Figure 3-10.

The sample is too small to determine whether cloud streets in the northerly flow have different characteristics from those in the southerly flow. If there are any significant differences, they do not show up in the histograms. However, comparison of the maximum length of cloud streets over hilly terrain with that over flat terrain seems to show a slight shift towards longer cloud streets in flat areas. Due to the uncertainties in the height computations from shadow length and the sun's elevation, heights were excluded from the frequency distributions.

Cloud streets appear to be linked to rather shallow convective layers. In a few cases in which showers developed at the downwind part of cloud streets, the pattern became disturbed, probably partly due to penetration of the cloud tops into a layer with a different wind regime and partly due to an increase of kinetic energy in precipitation-initiated downdrafts. In two cases, namely on 20 July 1974 and 25 July 1975, cloud streets were not associated with a curved wind profile; these cases are discussed separately. In all other situations, there was a distinct wind maximum in the convective layer.

Comparisons of average wind direction and speed in the convective layer, deduced from the nearest rawinsonde observations with those computed from cloud street configurations, are shown in Figure 3-11. Only in three cases could geostrophic winds be evaluated from surface

TABLE 3-6

COMPARISON OF FLOW CHARACTERISTICS DERIVED FROM CLOUD STREET FEATURES WITH GROUND TRUTH

Date	Time (GMT)	Location	$\bar{D}$ (degrees)	$\bar{D}_{RS}$ (degrees)	D_{geo} (degrees)	λ_x (kilometers)	λ_y (kilometers)	H_s	$\bar{T}$ (°K)	$\bar{\beta}$ (10^{-6})	$\bar{U}_{5.4}$	$\bar{U}_{RS}$ (m sec^{-1})	$\bar{U}_o$
6/17/73	15.00	MA-RI	35	15	27	1.9	4.1	2.1	284	0.8	19.3	(14.0)	14.7
1/17/74	15.00	Off ME	335	-	-	2.3	4.1	1.5	265	0.3	7.5	-	2.9
4/22/74	15.00	NC	207	230	-	2.1	3.9	1.4	285	1.0	11.8	(12.2)	7.2
4/29/74	16.00	AL	200	-	-	1.6	2.9	1.2	294	1.0	12.0	-	7.4
6/20/74	15.30	NY	0.3	349	354	2.5	4.1	1.8	283	1.1	16.0	(10.0)	11.4
8/21/74	16.30	central TX	184	165	-	1.5	3.2	1.3	295	1.0	12.7	(10.0)	8.1
6/30/75	16.00	WI-MI	202	222	-	1.7	3.1	1.2	290	1.0	12.0	(7.4)	7.4
7/03/75	16.30	central TX	170	157	-	1.1	2.4	1.0	296	0.8	9.0	(17.8)	4.4
7/03/75		KS	148	125	-	2.0	2.5	1.0	299	1.45	10.4	(5.8)	5.8
7/04/75		OK	160	140	-	1.5	2.5	1.4	300	1.0	15.8	(9.8)	11.7
7/08/75	15.15	NY-PA	239	237	225	1.5	3.2	1.3	290	0.8	10.0	(10.0)	5.4
7/12/75	15.30	IN-OH	209	206	-	1.8	3.6	1.9	286	0.8	18.8	(11.8)	14.2
7/18/75	16.00	TX-LA	200	195	-	1.8	4.2	1.7	292	1.1	17.0	(19.8)	12.4
7/25/75	15.15	FL	330	016	-	1.4	4.2	1.6	294	1.1	18.4	(1.8)	13.8
8/24/75	16.45	NB	190	189	-	1.4	2.7	1.3	290	0.8	12.1	(6.1)	7.5
8/15/75	15.19	WV	-	-	-	1.3	2.8	1.1	291	0.7	9.7	-	7.3

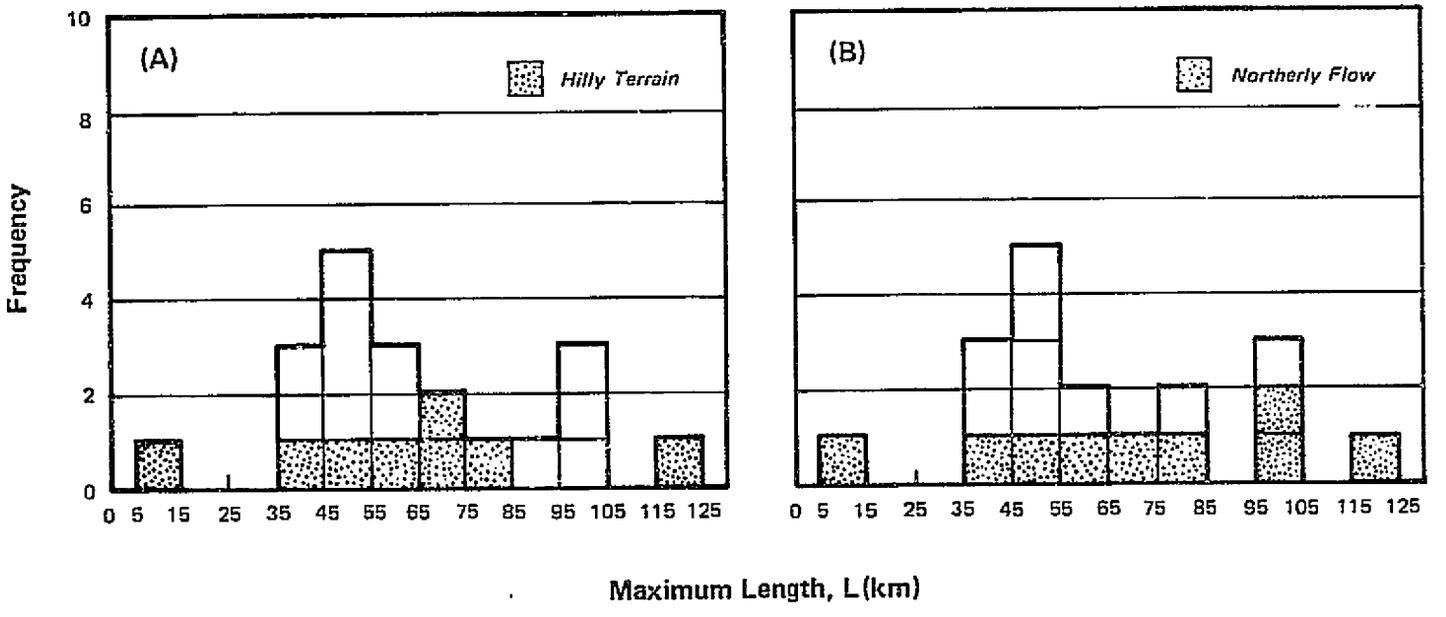

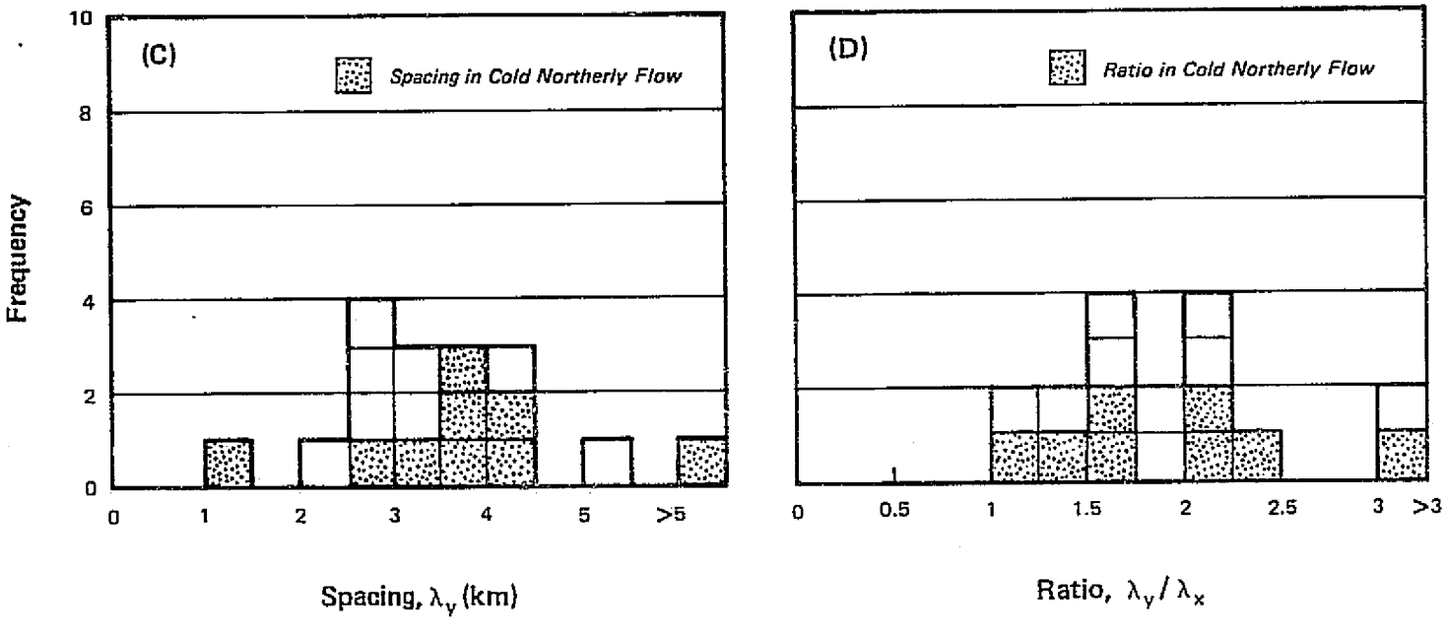

Figure 3-10 Frequency Distributions of Cloud Band Parameters Measured from Landsat Data Sample

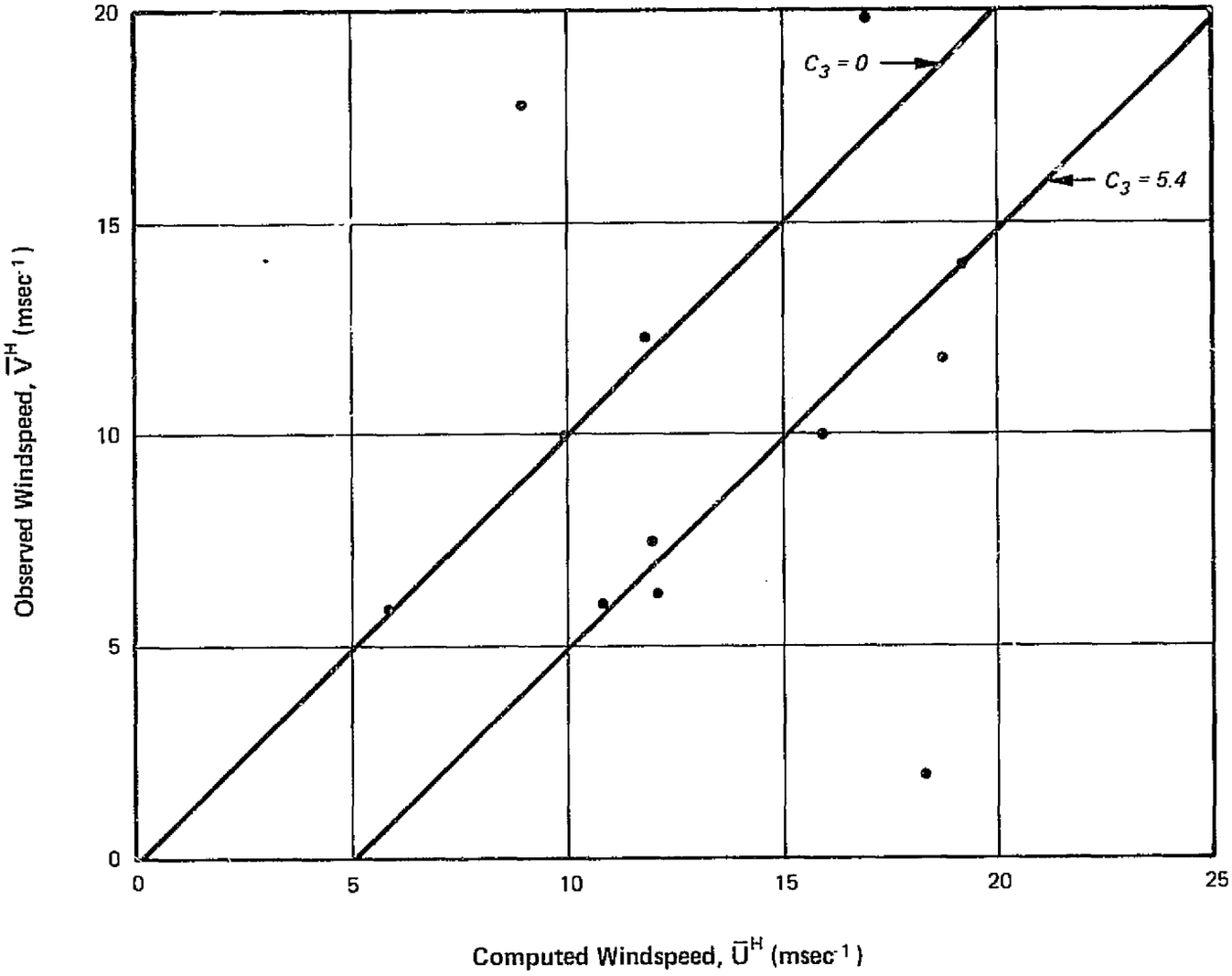

$\bar{U}$ was evaluated for c_3=5.4 m sec^{-1} and c_3=0 where c_3 is a measure of the surface wind (see Equations 6 and 7a in Appendix A).

Figure 3-11 Comparison between Average Wind Speed in the Convective Layer Computed from Cloud Band Configurations in Landsat Imagery

reports. The orientation of the cloud streets, averaged over the area covered by the Landsat images, falls within 20 degrees of the average wind direction in the convective layer; apparently they were aligned a little to the right of the mean wind.

Since the computations of the average wind speed $\overline{U}$ in the convective layer are sensitive to the value assumed for C_3 a measure for the surface wind, (see Equations 6 and 7a, Appendix A), $\overline{U}$ was evaluated for $C_3 = 5.4$ m sec^{-1} and $C_3 = 0$, respectively. The two values have been entered on either side of the column of $\overline{U}_{RS}$, the mean wind derived from rawinsonde observations. Generally, values for $\overline{U}_{RS}$ fell outside the margins set by the assumed values for C_3, but in view of the assumptions inherent in the Rayleigh-Kuettner model and the fact that ground truth did not coincide in space and time with the Landsat observations, the agreement between $\overline{U}$ and $\overline{U}_{RS}$ is encouraging.

Although at this time, it is not possible to give a more precise assessment of the feasibility of evaluating wind field characteristics in the convective layer from cloud band configurations on single Landsat images, it can be stated that the average wind direction can be estimated to within 20 degrees of the orientation of the cloud bands and the mean wind speed in the convective layer at least to within a factor of two, or eight meters per second, whichever is less.

In two cases, more serious discrepancies were found. In the case of 3 July 1975, the discrepancy may be due to the fact that radiosonde observations were only available from coastal stations, some 300 km away from the area of cloud banding over central Texas. The other discrepancy was found in the case of 25 July 1975, in which the orientation of cloud streets observed over south central Florida was entirely incompatible with the winds observed over Miami. Since the cloud streets were aligned parallel to the coast, specific terrain features may well have modified the low-level flow to the extent of making the Miami sounding entirely unrepresentative for the area of study.

4. TERRAIN-INDUCED CLOUDS

The deformation of airstreams by hills and mountains is often visibly revealed in a variety of orographic clouds whose form and characteristics tell a great deal about the nature of the airflow. In particular, such clouds not only indicate the location of ascending currents but to some extent the regions of turbulence as well. A considerable number of the examined Landsat images displayed evidence of terrain-induced mesoscale cloud features. These cases were analyzed and compared with the theory of wave cloud formation, in the same manner as was done for cloud bands, which was described in the previous section. A discussion of the theory of flow for terrain-induced clouds is given in Appendix B.

4.1 Description of Terrain-Induced Cloud Types

Orographic clouds fall naturally into certain distinct types, including cap clouds, banner clouds, rotor clouds, and lenticular clouds. Cap clouds comprise the simplest examples of forced ascent leading to saturation and cloud formation. The most important cap clouds are the cloud sheets which form over extensive mountain ranges with a base near or below the mountain tops. Some of these are present where cloud streets become distorted over higher terrain; others form in stable air. The most extensive cap clouds produce prolonged precipitation over mountain ranges. More rarely, when the mountain shape is simple and regular and the airflow is smooth, the cap cloud may take the form of a symmetrical lenticular cloud or that of a stack of shallow lenticulars resting on the mountain top.

Banner clouds are a feature of steep-sided isolated mountain peaks. These appear as a pennant of cloud to the lee of the peak and their formation is mainly due to the pressure reduction associated with the horizontal deformation of the air flow around the peak.

Rotor or roll clouds appear in the crests of strong mountain wave systems as large stationary rolls having the appearance of a line of cumulus or stratocumulus parallel to and downwind of the mountain crests. The base is usually near the level of the crest while the top may be several thousand feet higher. The rotation of these clouds

is due to the large positive vertical windshear through the cloud. Rotor clouds indicate very large amplitude lee waves and are associated with occasionally violent turbulence. In severe cases the airflow sweeps down the lee slope and rises steeply towards the rotor cloud, sometimes carrying a wall of dust from the lower lee slopes into the cloud. Roll clouds are usually confined to the first lee wave immediately downwind of the mountain crests. If a train of lee waves of sufficient amplitude develops, there may be a series of two or more roll clouds spaced out and oriented downwind parallel to each other and to the crest line.

Lenticular clouds are visual evidence of wave motions in the airflow over and to the lee of hills and mountains. Orographic lenticulars are mostly indicative of laminar smooth flow as is shown by their characteristically smooth outlines. They form where the air is lifted above its condensation level in the crests of standing waves. The cloud is continuously regenerated at the upwind edge and dissipated at the downwind edge.

Both wave and rotor clouds are better developed for steep slopes to the lee of a mountain than for gentle ones. Isolated hills produce less influence than long ranges of similar cross-section. The curvature of the crest line of a ridge when viewed from above seems to favor marked waves when it has a concave shape towards the oncoming air stream rather than a convex shape. Also, there may be interference between the flow above particular mountains and the lee waves due to other features upstream. This, of course, results in damping or amplification according to the phase relationships involved.

The equations and assumptions in this chapter are formulated from Appendix B, in which a theoretical exercise pertaining to wave cloud formation is discussed.

4.2 Analysis of Terrain-Induced Clouds Seen in Landsat Imagery

4.2.1 Summary of Landsat Cases Displaying Terrain-Induced Clouds

In the Landsat data sample, 15 images show conspicuous wave cloud patterns. These cases have been related to terrain features and circulation types in the same manner as the cloud band discussed in the

previous sections. The wave cloud characteristics are shown in Table 4-1. An example of a Landsat image displaying terrain-induced clouds is shown in Figure 4-1.

In three cases, wave clouds were viewed over flat terrain without any apparent connection to mountain ridges (Virginia, 31 July 1972; Texas, 20 April 1973; and near Detroit, 26 April 1974). These are probably the result of localized strong windshear within a relatively shallow layer (Kelvin Helmholz waves), although no concrete evidence for this shear can be found in the relatively widely spaced upper wind measurements by the nearest rawinsonde stations.

The analysis of three cases of wave clouds is described in detail in the following section.

4.2.2 Case 1: Eastern New England, 13 March 1974

The Landsat image shown in Figure 4-2, taken at 1450 GMT over Maine, shows a distinct pattern of wave clouds. The height of these clouds was estimated to be approximately 1,500m above the terrain. At the time of the satellite observation, a strong low-level flow from north to northwest existed in which the temperature lapse rate was conditionally unstable; the lapse rate became more stable above 800 mb, but without a sharp transition to the somewhat drier air aloft that was advected from a more westerly direction. North of the St. Lawrence River, snow showers were falling from an extensive cloud deck, whereas over the New England states, cloudiness was patchy with stratocumulus, altocumulus and some cirrus. Near the Atlantic coast, skies were mostly clear. It is of interest that neither the altocumulus nor the cirrus was apparently influenced by the wave motions in the lower layer of the atmosphere.

In this case, meteorological observations showed that the vertical wind profile curved with a maximum of 22 m sec^{-1} at the 1,500m level (Figure 4-3). Since the air in the lower part was dry, any helical circulations caused by surface heating did not show up in the form of banded cloud patterns. The wavy stratocumulus clouds visible on the Landsat image could be traced back to their origins: Saddleback Mountain (1,250m), Mount Abraham (1,230m) and Sugarloaf Mountain (1,280m); hence these were mountain induced rather than convective clouds.

TABLE 4-1

WAVE CLOUD PATTERN CHARACTERISTICS IN RELATION TO TERRAIN AND CIRCULATION TYPES

Date	Location	Time	Terrain	Synoptic Type	Flow Direction	Width (km)		Wave Length (km)	Height above Terrain (km)
						Average	Range		
7/31/72	Virginia	15.19	Flat	CWT	SW	200	180-250	2.5	1.4
4/5/73	Wash.State	18.21	Wenatchee Mts.	WA	W	23	5-40	22.0	7.4
4/6/73	Conn.	15.22	Taconic Range	WA	NW	37	23-60	13.8 & 16.0	1.8
4/22/73	Kansas	16.35	Rocky Mts.	SWC	SW	6	4-10	2.0	1.1
4/20/73	Mex. Gulf	16.26	Sea	CWT	SW	8	9-25	2.5	-
4/20/73	Texas coast	16.26	Flat	CWT	SW	14	5-20	3.0	-
5/8/74	Vermont	15.00	Green Mts.	WS	W	33	30-50	4.5 & 5.0	1.6
5/13/74	Maine	15.00	Saddleback Mts.	NC	N	20	10-24	6.7	1.3
3/14/74	Maine	15.00	Monadnock Mt.	NWC	NW	40	10-70	5.0 & 6.0	1.8
4/26/74	near Detroit	15.00	Flat	NWA	NW	45	10-15	5.0	1.6
4/11/74	Utah	17.00	Oxford Peaks Rocky Mts.	NC	NNW	40	20-26	10.5	1.0
4/11/74	West Utah	17.00	Granite Pk.	NC	NNW	60	30-80	6.0 & 8.0	1.4
7/4/74	NH-ME	14.49	White Mts.	NWC	NW	10.3	8-11	5.0	1.7

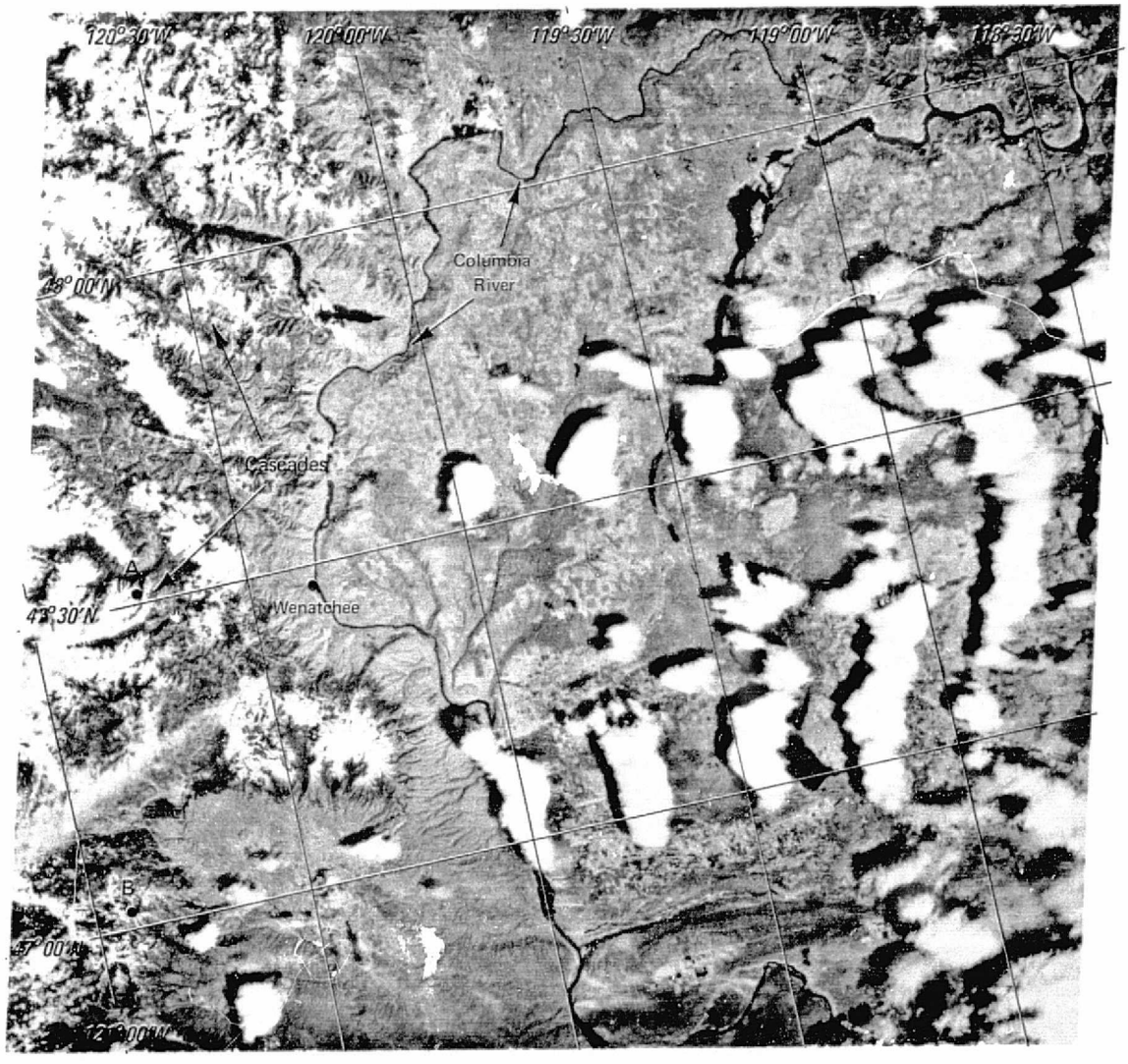

Points A and B are sources of wave cloud activity off mountains.

Figure 4-1 Landsat-1 MSS-5 Image (I.D. No. 1256-18212), 5 April 1973, Showing Terrain-induced Clouds Located over the Columbia Basin Area of Washington. The Cascade Range West of the Columbia River Induced this Wave Pattern

609000
609222

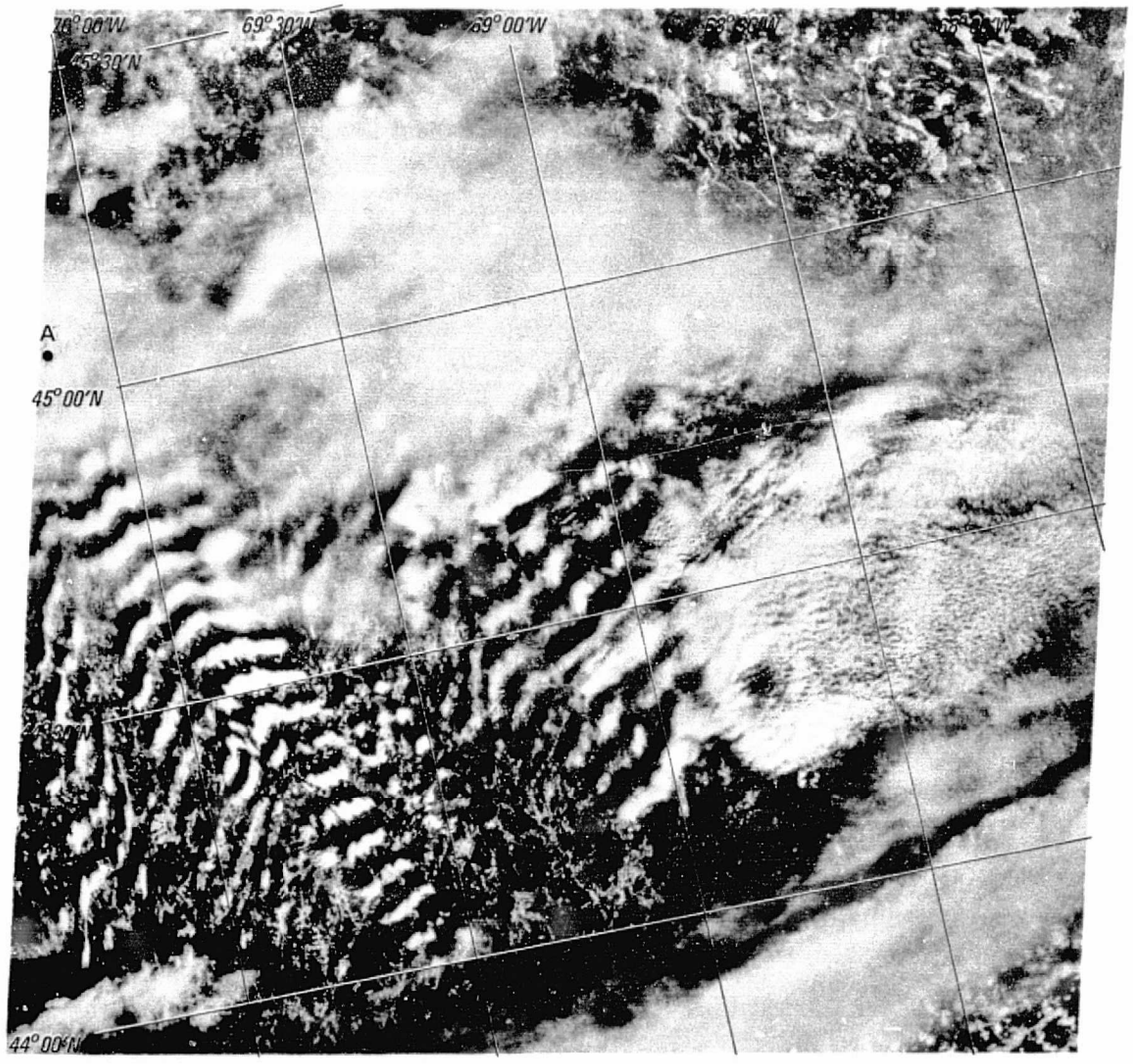

Point A represents a source of one rather long wave cloud covering over 200 km.

Figure 4-2 Landsat-1 MSS-5 Image (I.D. No. 1598-14500), 13 March 1974, Showing Distinct Pattern of Wave Clouds over Maine

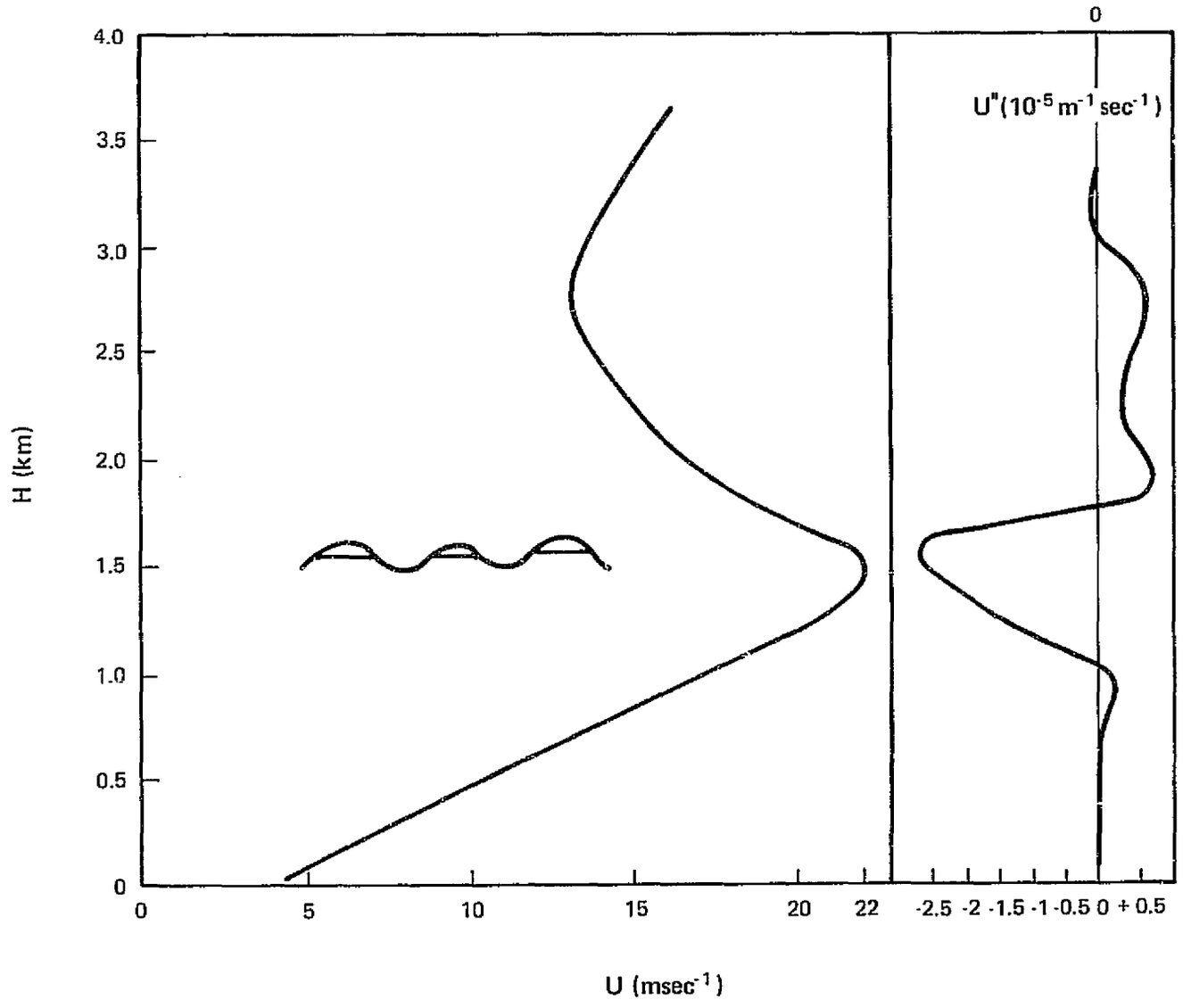

Figure 4-3 Diagram Showing Vertical Wind Profile (U) and Curvature (U") for Portland, Maine at 1200 GMT, 13 March 1974

The wave trains visible in Figure 4-2 contain up to 18 crests over a distance of 120 km, with the average wavelength being 6.7 km; initially, the crests are about 20 km long, and they diminish to 5 km before they disappear. There is no evidence of rotor clouds, nor is there any other sign of cumulus convection. This suggests a slow drying of the atmosphere due to subsidence. The wave parameter $F = g\bar{\sigma}/\bar{U}^2 - U''/\bar{U}$ (see Equation 2, Appendix B) is definitely positive between the 1,000m and 1,500m levels. It becomes smaller above 1,500m and probably changes to negative in the mid-troposphere. Solutions of Equation 2 for $\bar{U}'' = 0.6 \times 10^{-5}$ m sec^{-1} and $\overline{g\sigma} = 1.9 \times 10^{-5}$ m sec^{-2}, obtained from the 1200 GMT sounding at Portland, Maine would put the vertically averaged wind speed in the range of 7-14 m sec^{-1} for the observed wavelength of 6.7 km. The average wind speed determined from the sounding was roughly 15 m sec^{-1}.

4.2.3 Case 2: Central New England, 14 March 1974

A Landsat image taken one day later than the image of Figure 4-2 is shown in Figure 4-4. This image, therefore, covers the area just to the west of the area viewed on the preceding day. On 14 March, a large high pressure area originally over the Hudson Bay had moved southeastward while developing a ridge over the Great Lakes region. This resulted in a decrease of the northwesterly flow and of the cloudiness over the New England area. A layer of slightly more stable air above 800 mb had developed into a strong subsidence inversion (Figure 4-5).

Wave clouds were again predominant over western Maine and New Hampshire, but the pattern is somewhat more disorganized than in the previous case. Wave trains could be traced back to Mt. Dunstan (860m), Monadnock and White Mountain ranges. Wavelengths ranged from 5 to 6 km. The fuzzy appearance of some clouds in the vicinity of the Presidential Range suggests that these were causing precipitation in the form of snow.

The wind profile over Portland, Maine shows little curvature, suggesting that in the lowest 1,500m, U'' was close to zero. The average static stability β was 7×10^{-6} m sec^{-2}; hence the wave parameter F was positive. $\bar{U}$ is thus computed to be 6 to 8 m sec^{-1} (See Appendix B, Equation 4a). The observed average windspeed in the layer was

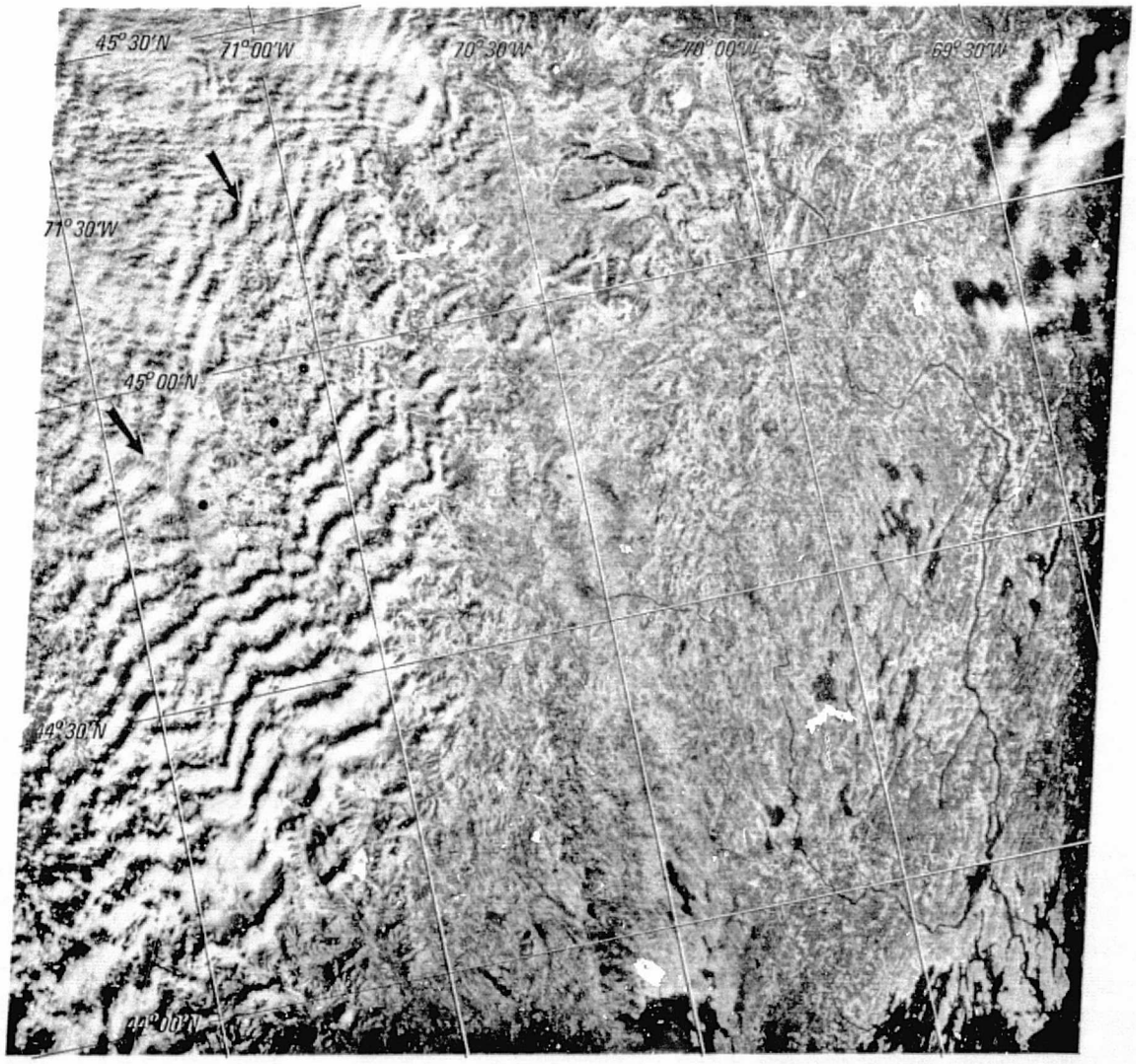

The near-infrared band was chosen in this instance because wet snow cover, which appears bright in the MSS-5 band, appears considerably darker in the MSS-7 image, thus allowing better definition of the cloud pattern. Dots represent several wave cloud sources, arrow represents upper level wind direction.

Figure 4-4 Landsat-1 MSS-7 (near-IR) Image (I.D. No. 1599-14554), 14 March 1974, Showing Wave Clouds over Northern New Hampshire

609001
609226

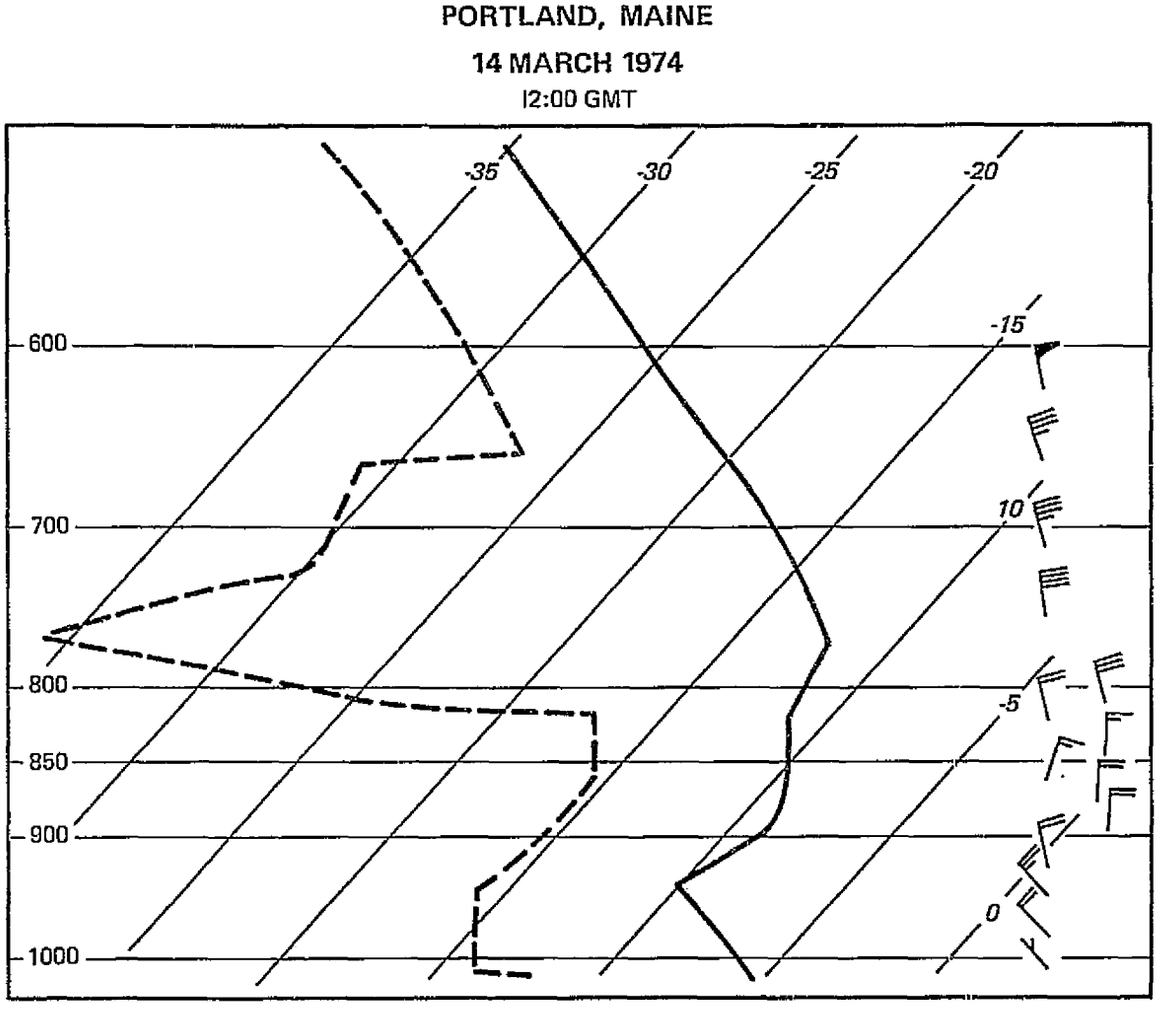

Pressure is in mbs and temperature in °C.

Figure 4-5 Adiabatic Diagram for the Portland, Maine 1200 GMT Rawinsonde Data of 14 March 1974

8.5 m sec^{-1}. This case illustrates the real possibility of finding mountain waves at relatively low levels in cold northerly flows. In these situations wave clouds are confined to a shallow layer of conditionally unstable air near the surface and do not seem to propagate upwards far enough to disturb any overlying altostratus or cirrus clouds.

4.2.4 Case 3: Southern New England, 6 April 1973

A Landsat observation at 1502 GMT, 6 April 1973, shows a dissipating wave pattern over southern New England (Figure 4-6). At this time, wave clouds were occurring in westerly flow between a low-pressure area over Nova Scotia and a high-pressure system over the southern United States.

Comparison of the heights of the clouds over the terrain determined from the cloud shadows along with the depth of the moist conditionally unstable air shows that the waves formed at, or below, the inversion at 2 km above the surface, that separated this layer from dryer, more stable air aloft (Figure 4-7). The waves may have been induced by the Taconic range and the southern Berkshire Mountains. In the lowest 2 km, the wind gradually increased with height and veered slightly between west and northwest. The average curvature U" of the vertical wind profile was close to zero; the average static stability parameter $\overline{g\sigma}$ close to 10^{-4} $msec^{-2}$ (Appendix B). Average wind speeds of 22 to 25 $msec^{-1}$ were computed from Equation 4a for the observed wavelengths of 13 to 16 km; the average wind speed in the 2 km deep layer obtained from rawinsonde data ranged from 14 to 18 $msec^{-1}$.

Of interest is a rapid transition from wave clouds to scattered small cumulus clouds over southern Connecticut and Rhode Island. Below and near these convective cells, the average static stability was certainly negative, causing the wave parameter F in Equation 2 (Appendix B) to change sign somewhere in that area. The simple wave theory, then, would not provide a real solution for the wavelength λ; the complete disappearance of the waves seems to confirm this. Note also that the wavelength did not diminish; this result suggests a rapid damping of the vertical oscillations in the flow.

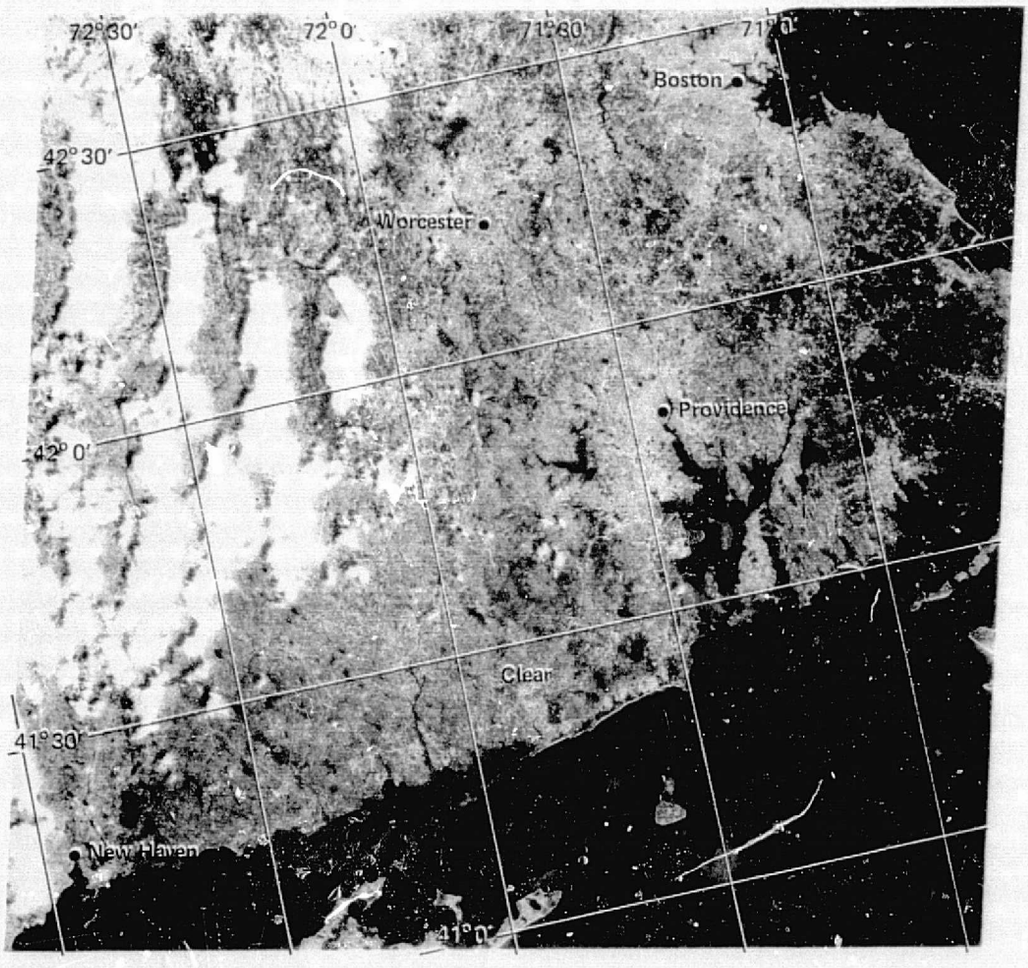

Figure 4-6 Landsat-1 MSS-5 Image (I.D. No. 1257-15021), 6 April 1973, Showing a Dissipating Wave Cloud Pattern over Southern New England

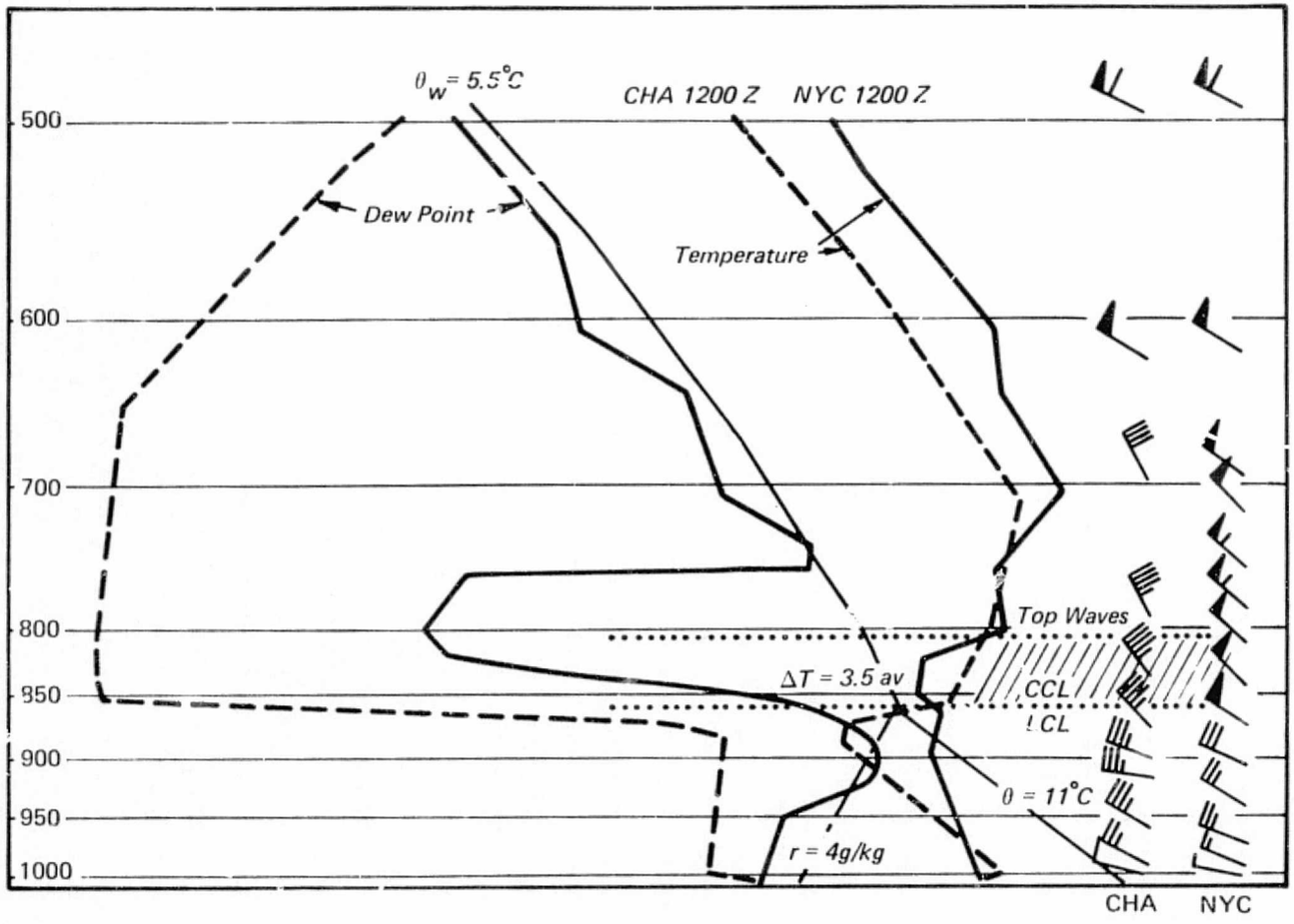

Figure 4-7 Adiabatic Diagrams Showing Temperature, Dew Point and Winds at Chatham, Mass., and New York City, 1200 GMT, 6 April 1973

4.3 Discussion of the Results of the Analysis of Terrain-Induced Clouds

In the analysis of terrain-induced clouds, in only one case (5 April 1973, Washington State) did the wave clouds show the classical pattern described in Alaka (1968). All remaining cases are relatively shallow waves at heights of less than 2 km above the terrain in cold low-level airflows, many of which showed a curved vertical wind profile with a distinct wind speed maximum within the cold flow. Moreover, the waves occurred over, or could be traced back to relatively low mountainous areas in which the highest tops did not extend above 1,500m. In the cases analyzed, the observed wave cloud characteristics did not correspond as closely with those computed from the windfield as had been reported in some of the earlier studies (Alaka, 1968).

Comparisons of average wind speed $\bar{U}$ in the layer below the wave cloud tops, deduced from the nearest rawinsonde observations, with those computed from the spacing of the wave clouds are shown in Table 4-2. In the first two cases $\bar{U}$ could be computed from Equation 4 ($\bar{U}_1$) as well as from Equation 4a ($\bar{U}_2$) as the negative curvature U'' of the wind profile dominated in Equation 4. Apparently, incorporation of the static stability, σ, and curvature, U'', in this equation leads to overestimation of the average wind speed; neglect of σ produces wind speeds below those observed by rawinsondes, showing that both quantities need to be known with greater accuracy.

In all other cases the ratio H/λ did not permit direct computation of the wind speed from wave cloud spacing and depth alone. Also, U'' was rather small in comparison with σ so that only Equation 4a of Appendix B was used to derive the wind speed.

Generally spacing λ and height H of the wave clouds were poor predictions of the flow characteristics as was the static stability σ. What can be said, though, is that winds are likely to be strong in northerly flows for which $H/\sigma < 0.2$, and there may be a distinct wind maximum below the wave crests. In this case, solutions of Equation 2 indicate that static stability is of secondary importance for the development of waves in the 10 to 20 km wavelength category even if it departs much from zero. However, since airmasses flowing from the north tend to have a marginally stable vertical temperature lapse rate,

TABLE 4-2

COMPARISON OF WIND SPEEDS COMPUTED FROM WAVE CLOUD CHARACTERISTICS WITH ATMOSPHERIC PARAMETERS

Date	Time	Wave Cloud Characteristics		Terrain Characteristics			Atmospheric Parameters			Computed Wind Speeds	
		(km)	n	Z_m	B_m	l (km)	$\bar{\sigma}$ (10^{-5})	H_S	$\bar{U}_{RS}$	$\bar{U}_1$	$\bar{U}_2$
4/6/73	15.02	16.0	-	-	-	-	1.0	1.8	14.0	22.0	11.0
4/6/73	15.02	13.8	-	-	-	-	2.0	1.5	18.0	25.0	10.8
3/13/74	14.50	6.7	18	1.26	3.0	3.0	1.2	1.8	15.0	7.0-14.0	-
3/14/74	14.55	5.0	9	0.95	1.2	5.0	0.7	1.6	8.5	6.0-8.0	-
5/8/74	15.00	5.0	10	0.9	5.0	20.0	0.6	2.1	7.5	6.0	-
5/8/74	15.00	4.5	10	0.8	4.0	17.0	1.5	1.3	7.5	10.0-12.0	-
7/4/75	14.49	5.0	9	1.1	1.5	15.0	0.5	1.7	5.0	5.6	-

n is the number of waves in the wave train.

Z_m is the height of the mountain tops.

B_m is the mountain half-width measured towards the downwind side.

$\bar{\sigma}$ is the static stability $(\overline{\Gamma_d - \Gamma_e})\bar{T}$; Γ_d is the dry adiabatic lapse rate; Γ_e is the environmental lapse rate.

vertical displacements in these airmasses require little energy. This could mean that rotor currents and severe turbulence (with or without visible clouds) may be found below the crests of the waves.

5. OTHER MESOSCALE CLOUD FEATURES OBSERVED IN LANDSAT IMAGERY

During the initial examination phase of the Landsat data base, a number of other interesting mesoscale cloud features were noted, including cumulonimbus thunderstorm cells associated with prefrontal squall lines, cumulus congestus cloud rows over coastal waters aligned parallel to the coast, altocumulus cloud layers, and large-scale convective cloud bands located over mountainous terrain. Some of these mesoscale features are described in the following section

5.1 Cumulonimbus Cells - New England and Florida

A total of eleven Landsat cases in which cumulonimbus cells were observed were selected for analysis of cloud heights, cloud diameters, flow direction, associated terrain, and comparison with correlative meteorological conditions. These cases are listed in Table 2-5. Examples of cumulonimbi observed in Landsat imagery are shown in Figures 5-1 and 5-3.

The Landsat-1 image of 28 August 1973, shown in Figure 5-1, views a massive cumulonimbus cell located over central New Hampshire. The cirrus anvil of the cumulonimbus covers an area nearly 140 km long; the cirrus has advected well east of the convective portion, which comprises only the westernmost third of the cloud. Analysis of the corresponding radar microfilm for this date (supplied by the AFGL Radar Site, Sudbury, Massachusetts) confirms this. The precipitation area observed on the radar film at the time of satellite observation (1500 GMT), shown in Figure 5-2, is located within the extreme western end or convective portion of the cell. Information documented in the August 1973 Storm Data and Unusual Weather Phenomena data booklet (NOAA Publication), indicates that Auburn, New Hampshire, located just east of Manchester, experienced 1-inch hail 1 1/2 hours after the time of this Landsat image. Also, another cumulonimbus cell located to the south over western Massachusetts and eastern New York State (northern limit of this cell is observed in the lower left portion of Figure 5-1) is reported to have caused a large tornado about two hours later. The tornado moved across the New York border into western Massachusetts and leveled a large truck stop complex in West Stockbridge killing four people; in addition, several homes and thousands of trees were also reported to have been destroyed.

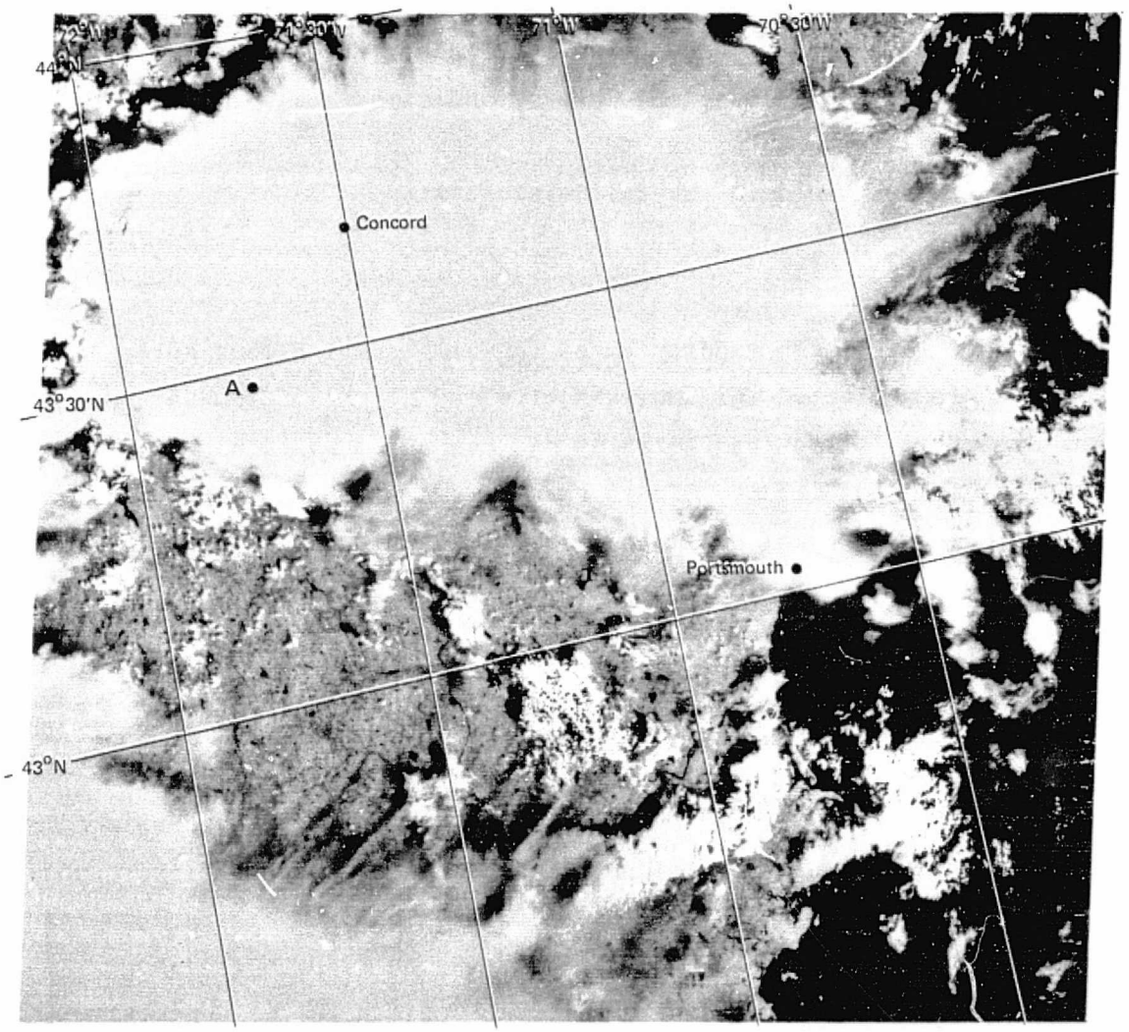

The cirrus anvil covers an area approximately 140 km in length. This Cb produced severe weather, with one-inch hail, about an hour after the satellite observation. Point A indicates region of most severe weather at time of photograph.

Figure 5-1 Landsat-1 MSS-5 Image (I.D. No. 1401-15001), 28 August 1973, Viewing a Massive Cumulonimbus Cell over Central New Hampshire

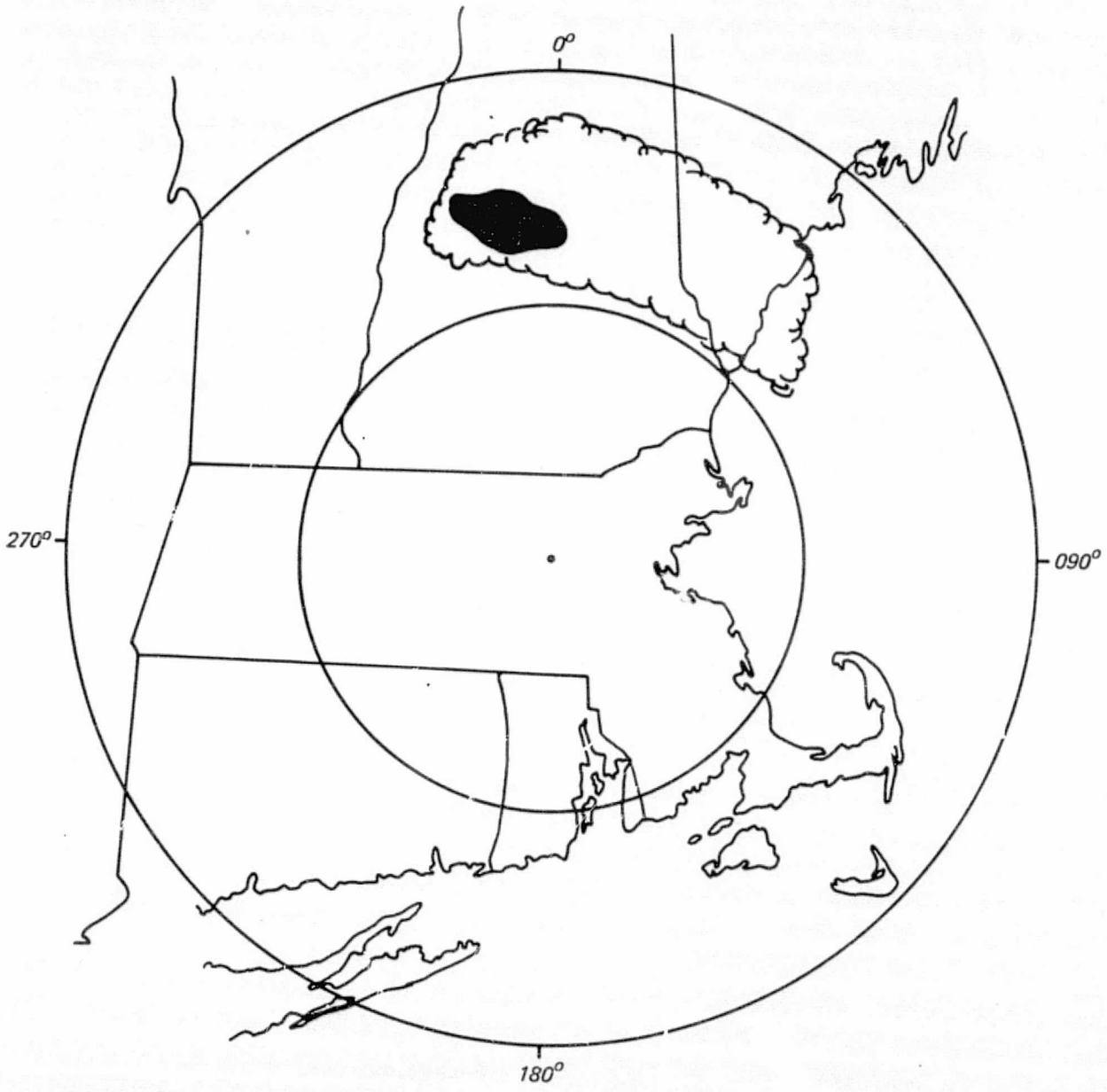

Figure 5-2 Comparison between Area of Cumulonimbus Cell and Cirrus Anvil Seen in Landsat Image (Figure 5-1) and the Actual Precipitation Area Measured by Radar at the Time of the Satellite Observation

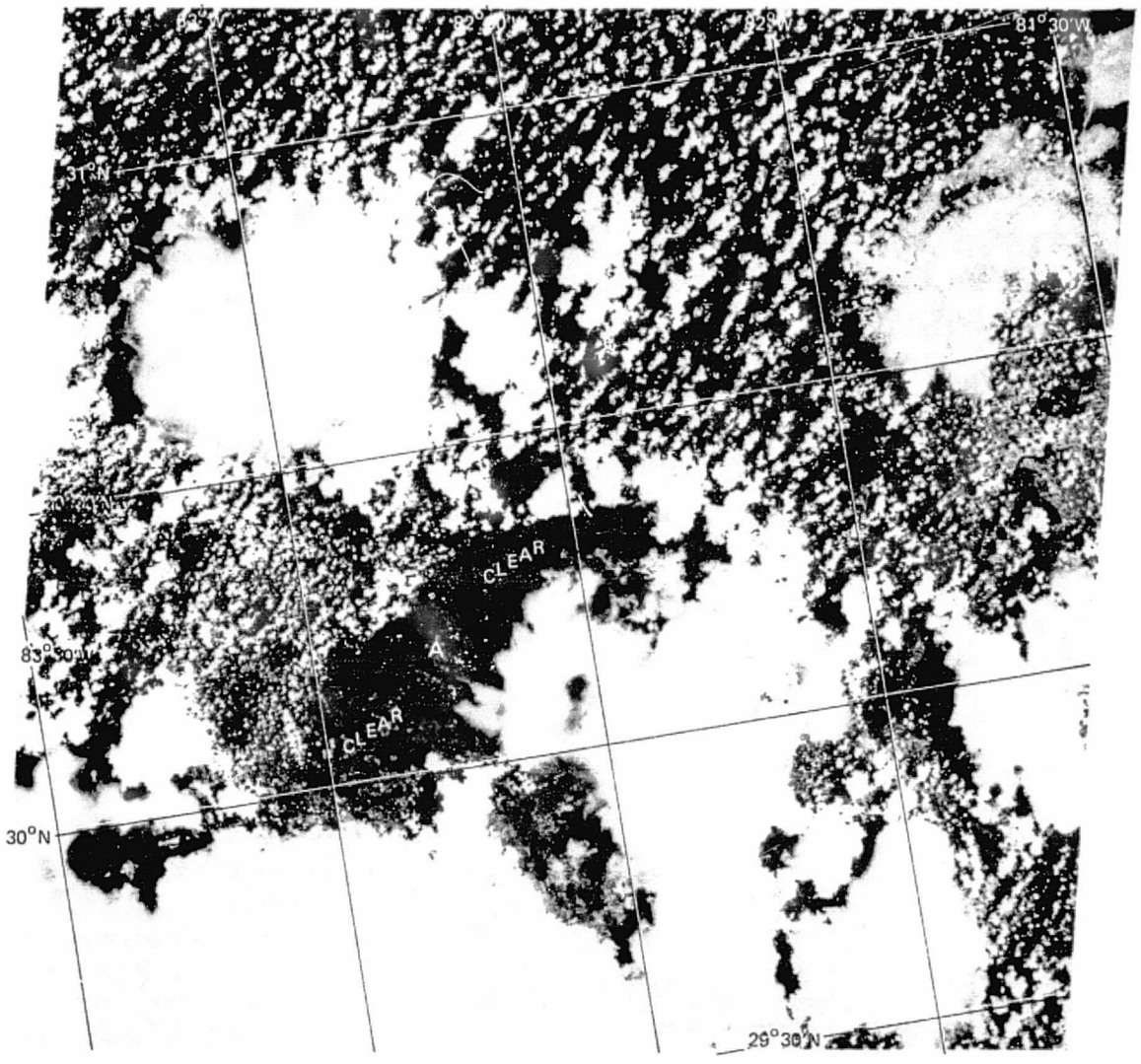

An area of suppressed convection, apparently resulting from the cold air outflow of the Cb cells, is seen near the center of the image (Point A).

Figure 5-3 Landsat-1 MSS-5 Image (I.D. No. 1388-15325), 15 August 1973, Showing Three Different Scales of Convective Cells over Northern Florida

The correlative meteorological surface data at 1500 GMT showed a cold front oriented east-west across northern New England. Cooler, dryer air was progressing slowly southward on a moderate northwesterly flow and displacing much warmer tropical air (temperatures some 10°C higher), which had been established in southern New England. The cumulonimbi observed in the Landsat data were therefore associated with an intense squall line moving southeastward across New England ahead of the cold front.

Another example of convective cells is given in Figure 5-3. In this case, the Landsat image of 15 August 1973 shows three different scales of convection over northern Florida. The smaller elements are cumuliform convection with tops at 2 to 3 km above the terrain; intermediate size cells are cumulonimbus clouds in the growing stage, (15 to 20 km across) with tops up to 22 km high; the largest cloud cells are cumulonimbus having diameters of 40 to 60 km. These cumulonimbus clouds formed in accelerating confluent flow. Over the cloud area, the winds at 850 and 700 mbs were 7 m sec^{-1} from directions of 240 to 250 degrees; surface winds were generally weak.

Of interest is a decaying cumulonimbus in the center of the satellite image. To the northwest of this cell, a 70 km long and 30 km wide clear area indicated suppressed convection; in fact a small mesoscale high has developed. Its major axis is about parallel to the 850 to 700 mb wind direction. On part of its outer boundary there is a sudden transition from no clouds to well-developed cumulonimbus. Apparently, the cloudless area delineates cold outflow from the decaying cumulonimbus. This cold outflow occurred on the left hand side of the old storm (looking in the direction of motion) and lifted the warmer air in advance of its outer edge.

5.2 Offshore Convective Cloud Bands - North Carolina

The Landsat-1 image of 4 October 1973 shown in Figure 5-4 reveals cloud formations east of Cape Hatteras, North Carolina within a weak westerly flow throughout most of the troposphere. The irregular convective cloud pattern suggests the presence of medium-level convection and an atmosphere which is convectively unstable with respect to vertical

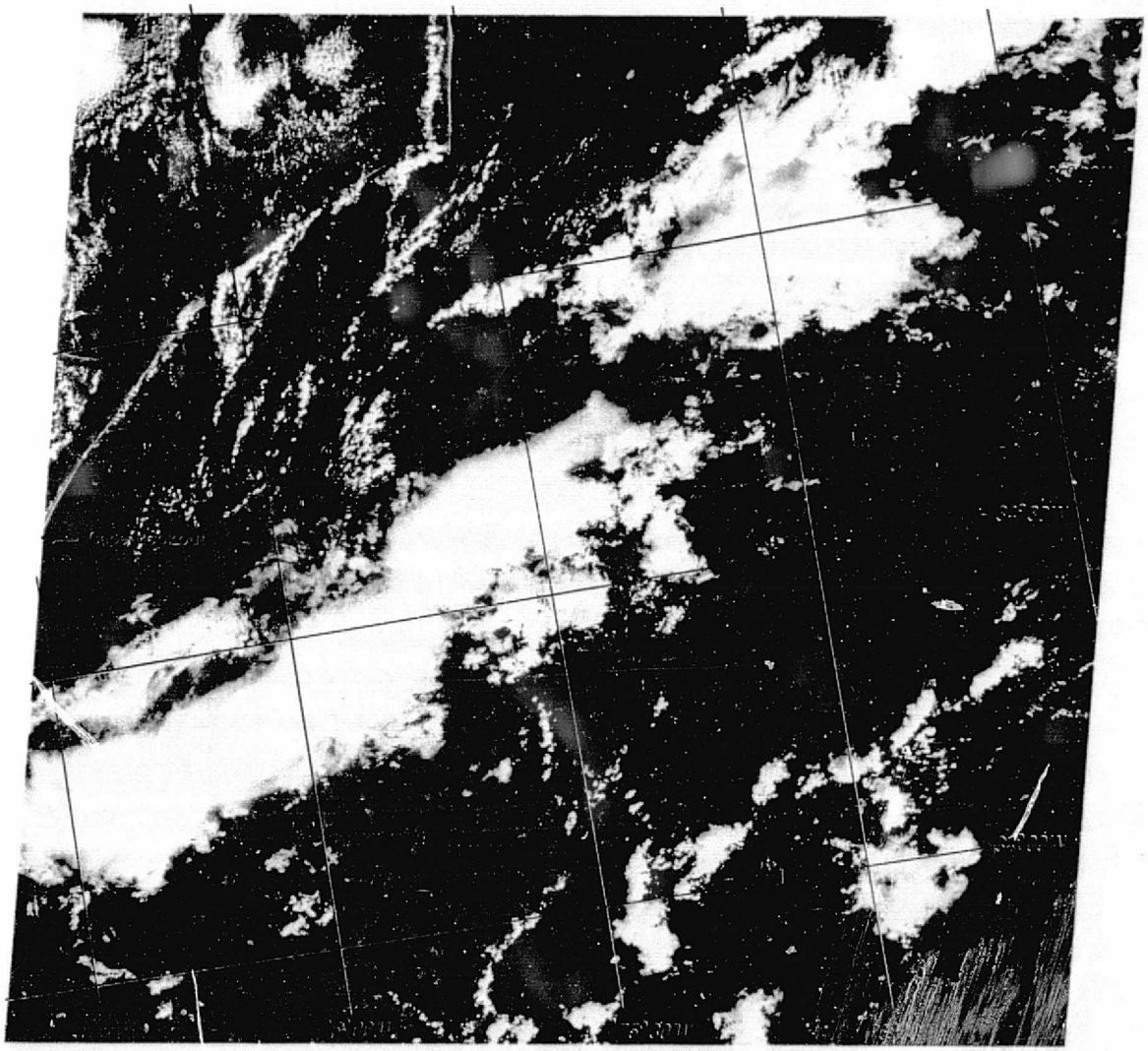

Figure 5-4 Landsat-1 MSS-5 Image (I.D. No. 1438-15074), 4 October 1973, Viewing Convective Cloud Formations over the Ocean Just East of Cape Hatteras

lift. However, rawinsonde observations were unavailable to confirm this, and it was not possible to discern the cloud shadows over the darker ocean water. Cloud rows aligned parallel to the coastline suggest an incipient sea breeze circulation, an effect which is plausible in late morning and in weak synoptic scale circulations. The larger band of deeper convective clouds in the dissipating stage may well be the visible remains of a disappearing land-sea-breeze convergence zone. The land breeze, then, would have extended 60 km offshore. Due to lack of ground truth, this interpretation, though plausible, remains highly speculative.

5.3 Large-Scale Convective Cloud Bands Over Mountainous Terrain

Figure 5-5 shows the Landsat-1 image of large-scale convective cloud bands over northeastern Colorado and southern Wyoming on 26 April 1974. This image reveals that convective cloud bands do occur over higher elevation terrain. In this case, they are aligned in the direction of the wind, which was reported as southwesterly 15 to 25 m sec^{-1} at 500 mb. There was a weakening frontal zone over the area at this time with scattered showers over the high elevations. The tops of cells extended up to 9 km above the terrain and probably through the entire depth of the troposphere; the smaller cumulus elements were 2 to 5 km wide and 2 to 5 km deep. The cloud bands extended up to 80 km long, with the spacings from 7 to 8 or 15 to 18 km. This would give a spacing to depth ratio of about 3, a little higher than that predicted by the Kuettner theory. Although there are neither surface data nor rawinsonde data available, it is quite conceivable that part of the southwesterly flow was channeled by the valleys and showed Poisseuille or Couette characteristics with a distinct wind maximum a few km above the terrain.

5.4 Altocumulus Cloud Layer - Ohio

The Landsat-1 image of 17 August 1973 shown in Figure 5-6 displays fields of altocumulus floccus and castellanus located in a warm, humid airmass over Ohio. The flow was weak between the west and southwest, increasing to 10 to 15 m sec^{-1} at 500 mb. During the latter part of the day, an upper air trough moved over the area. At the time of observation, no showers or thunderstorms were reported over Ohio, although

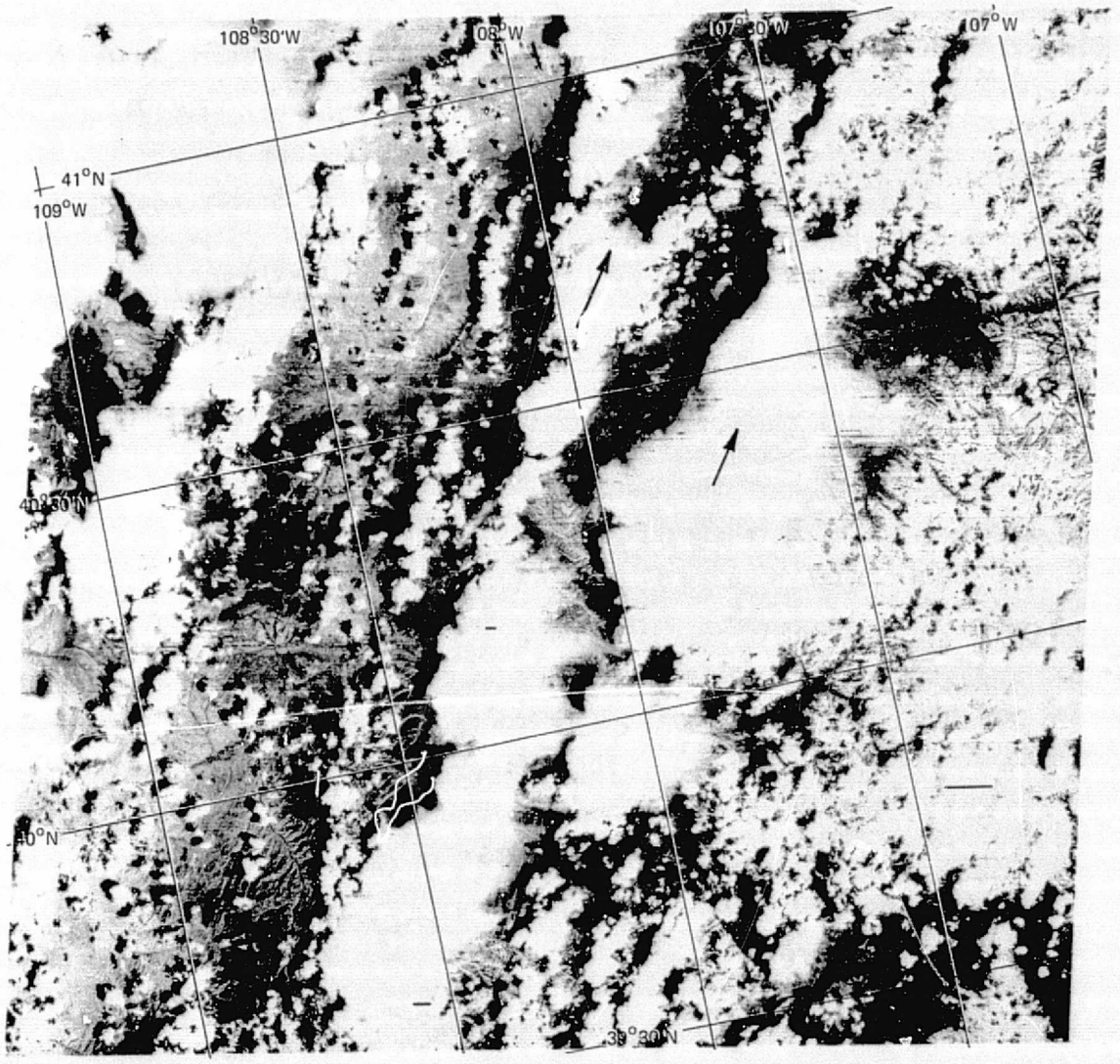

Figure 5-5 Landsat-1 MSS-5 Image (I.D. No. 1642-17193), 26 April 1974, Showing Large-scale Convective Bands over Colorado and Wyoming

609014

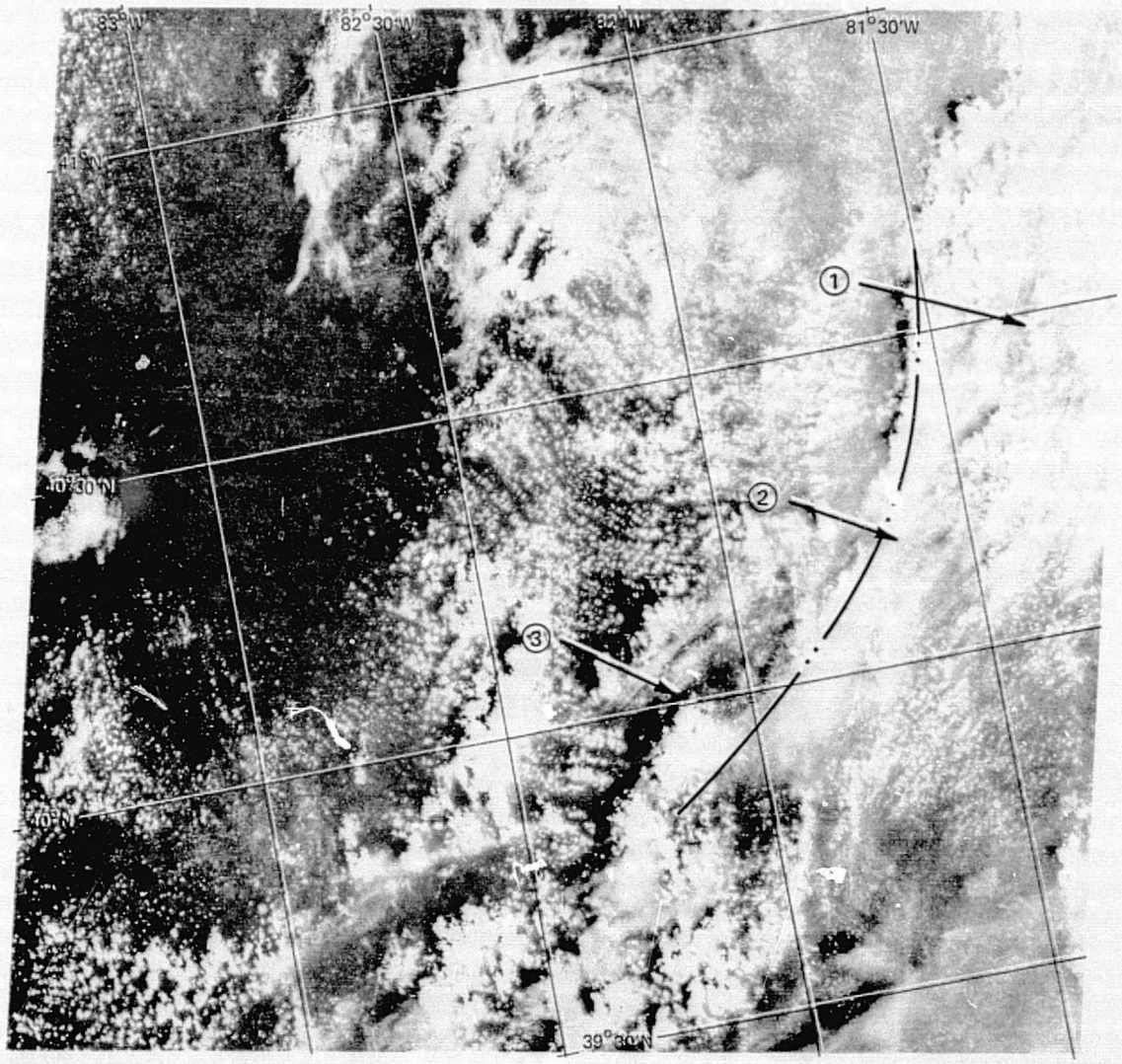

Arrow (2) points to cirrus blowoff downwind from Cb's along squall line while downward motions created from Cb outdrafts form clear areas (arrow (3)).

Figure 5-6 Landsat-1 MSS-5 Image (L.D. No. 1390-15412), 17 August 1973, Showing What Appear to be Fields of Altocumulus Floccus and Castellanus (arrow (1)) over Ohio

some of the larger elements, extending upwards to about 6 km above the haze layer, on which they cast their shadows, may have given brief spells of light to moderate rain. Behind the larger patches of cloud, curved rows of small elements are aligned perpendicular to the flow. These may indicate Kelvin - Helmholz waves in the layer where the wind increases from light variable to 10 or 15 mps from the southwest. Unfortunately, there are no rawinsonde observations to confirm this.

6. CONCLUSIONS AND RECOMMENDATIONS

In this investigation some 50 Landsat images displaying mesoscale cloud features were analyzed. Many other images were examined, but could not be analyzed in detail within the scope of the project. The mesoscale cloud features studied included cumulus cloud bands, terrain-induced wave clouds, and cumulonimbus cells. The conclusions based on the analysis of the cloud band and wave cloud cases are given below in Section 6.1; a discussion of the advantages and limitations of Landsat data for mesoscale cloud research is given in Section 6.2; and recommendations for further study using Landsat data are given in Section 6.3.

6.1 Conclusions Based on Analysis of Mesoscale Cloud Patterns

6.1.1 Cloud Bands

The analysis of cumulus cloud bands was based on the Rayleigh-Kuettner model describing the formation of that type of mesoscale cloud feature. The Rayleigh-Kuettner model lends itself rather well to computation of the average wind speed in northerly flow from the dimensions of the cloud band configurations measured from a Landsat image. In nearly every case examined, the necessary conditions of a curved wind profile and orientation of the cloud streets within 20 degrees of the direction of the mean wind in the convective layer were met. Verification of the results by direct observation was hampered, however, by the incompatibility of the resolution of conventional rawinsonde observations with the scale of the banded cloud patterns measured from the Landsat observations. The comparison seems to be somewhat better in northerly flows than in southerly flows, with the largest discrepancies in wind speed being within 8 m sec^{-1}, or a factor of two. This range may be narrowed down by further statistical evaluation of the most probable shape of the wind profile and relationships among the speed of mean wind, the maximum wind, and the surface wind under cloud banding conditions. This approach is likely to be most successful over oceans where terrain features, which distort the flow patterns in the lowest hundred meters or so, are avoided.

6.1.2 Wave Clouds

The samples of Landsat image used in this study contain surprisingly large numbers of wave clouds associated with northerly flows. These flows are often of the same type as the ones in which cloud bands are observed. The main characteristics are a conditionally unstable vertical temperature lapse rate combined with a curved vertical wind profile and little change in wind direction. When such an airmass is heated from below, helical circulations develop which are perpendicular to the mean wind, and give rise to banded cloud patterns. When the air is forced over a mountain ridge perpendicular to the flow, wave clouds are induced. Some of the images examined show both types of cloud over the same area or hybrid varieties of mountain-induced low-level convection in the form of solitary cloud rows.

In the wave cloud cases, a search for rotor clouds or lee vertices did not provide any positive results. However, a low-level wind maximum in a marginally unstable atmosphere may favor the development of turbulent vortex pairs along the wind maximum. These would be triggered at the downwind slope of the mountain ridge and coincide with the wave crests. Since such vortices, whether visible or not, could have an adverse effect on aircraft safety, their actual presence underneath the wave clouds needs to be verified. Fairly sophisticated physical-mathematical models of cloud streets and mountain waves are well documented in the meteorological literature. However, in spite of the sophistication of mountain wave theory and the successes claimed by earlier investigators, estimates of windspeed from the wave parameter equations compared rather poorly with direct observation. Perhaps the inadequacy of routine rawinsonde observations for computations of static stability and wind profile curvature in marginally unstable flows may account for the discrepancies.

6.2 Advantages and Limitations of Landsat Data

Landsat can view mesoscale cloud features at a more detailed scale than is possible from other satellites; at the same time, since the area covered by a single image is considerably larger than the area that can be viewed from an aircraft, the overall extent of a mesoscale pattern

can often be determined. Thus, mesoscale cloud features can be studied more thoroughly using Landsat than any other existing observational system. This is of particular importance in studies of unusual weather events such as severe storms when far greater detail is needed than that which conventional data can provide.

Moreover, based on the theory of the formation of cloud bands, it is possible to estimate the main characteristics of low-level flow in data-silent areas from the properties of cloud bands only. The pertinent cloud pattern characteristics, such as the spacing between cloud bands, the spacing between the elements in each band, and the cloud top heights, can easily be measured from a Landsat image. The only other information needed is an estimate of the surface temperature, which can be obtained from satellite radiometric measurements or from climatology.

The configuration of the Landsat system is, at this time, suitable only for research purposes. The lack of repetitive coverage and the availability of only an instantaneous observation are serious limitations. Nevertheless, further study using the ever-increasing Landsat data sample will lead to a greater understanding of the atmospheric processes associated with mesoscale clouds, and may lead to improved techniques for forecasting these features, particularly with regard to their effects on aviation. Landsat, although designed to view the earth's surface, is, indeed, another useful tool that can be employed in meteorological research.

6.3 Recommendations for Further Study Using Landsat Data

The analysis presented in the above sections demonstrated the utility of Landsat imagery in the study of mesoscale cloud features. However, temporal and fiscal constraints limited the number of cases studied to a subset of the entire data set available. The analysis was also limited by the difficulty in obtaining coincident ground truth. Further study of the features is thus recommended to utilize the satellites' larger data bank and special measurement networks currently in operation.

Statistical properties of cloud street structure and organization should be derived through the analysis of a more extensive number of images. Such a study would enable verification of the cloud street

characteristics found during these programs and permit a more comprehensive review of the situations where cloud streets occur under conditions significantly different from those predicted by theory. Even though high resolution synoptic data would probably not be available for most of the cases, the use of a statistical approach should eliminate many of the existing uncertainties in the interactions among atmospheric, surface and cloud parameters.

It is also recommended that additional case studies be analyzed over high density networks such as those operated by Project Hiplex. These networks with high spatial and temporal coverage of meteorological parameters provided by special rawinsondes, radars, etc. were not in operation in time for their data to be used in the current study. However, future studies could utilize these measurements with applicable Landsat imagery to provide more in-depth study of cloud banding, wave clouds and severe storm situations.

In addition, the possible application of high resolution imagery to meteorological forecasting should be explored. The case study of 17 June 1973 showed an example of a wind shift line and air mass changes stretching from White Plains, New York to Block Island, Rhode Island. Conventional analyses did no more than hint at such a perturbation, indicating that imagery such as that provided by Landsat shows great potential in improving local weather forecasts. Refinement of the techniques for estimating low-level winds would also provide a useful meteorological tool for obtaining flow patterns over data-silent areas.

REFERENCES

Angell, J. K. D. H. Pack and C. R. Dickson, 1968: A lagrangian study of helical circulations in the boundary layer, J. Atmos. Sci., 25, pp. 707-717.

Barnes, J. C. and C. J. Bowley, 1974: The Application of ERTS Imagery to Monitoring Arctic Sea Ice, Final Report, Contract NAS 5-21802, Environmental Research & Technology, Inc., Concord, MA, 93 pp.

Copeland, G. E., R. N. Blais, G. M. Hilton, and E. C. Kindle, 1974: Detection and measurement of smoke plumes in aerial and satellite imagery, paper presented at 67th Annual Meeting of the Air Pollution Control Association, Denver, Colo., June 9-13, 1974.

Greenwood, L. R., 1974: Environmental surveys, Discipline Summary Report of Proceedings of Third ERTS Symposium, NASA Publication SP-357, Goddard Space Flight Center, Washington, pp. 107-120.

Griggs, M., 1974: A method to measure the atmospheric aerosol content using ERTS-1 data. Proceedings of Third ERTS Symposium, NASA Publication SP-357, Goddard Space Flight Center, Washington, pp. 1505-1518.

Konrad, T. G., 1968: The alignment of clear air convective cells. Proc. Intl. Conf. Cloud Physics, Toronto, Canada, pp. 539-543.

Konrad, T. G., 1970: The dynamics of the convective process in clear air as seen by Radar. J. Atmos. Sci., 27, 1138-1147.

Lyons, W. A. and R. A. Northouse, 1974: Use of ERTS-1 Imagery in Air Pollution and Mesometeorological Studies Around the Great Lakes, Proceedings of Third ERTS Symposium, NASA Publication SP-357, Goddard Space Flight Center, Washington, pp. 1491-1504.

Lyons, W. A. and S. R. Pease, 1973: Detection of particulate air pollution plumes from major point sources using ERTS-1 imagery, Bulletin of the American Meteorological Society, Vol. 54, No. 11, pp. 1103-1170.

Plank, V. G., 1966: Wind conditions in situations of patternform and nonpatternform cumulus convection, Tellus 18, pp. 1-12.

Plank, V. G., 1974: A Photoreconnaissance Technique for Conducting Time-Lapse Studies of the Development and Motions of Cumulus Cloud Popuand Systems, AFCRL-TR-74-0250, Environmental Research Papers No. 428, pp. 69.

Rayleigh, L., 1916: On convection currents in a horizontal layer of fluid when the higher temperature is on the underside. Phil. Mag. (Ser. 6, 32, pp. 529-546).

REFERENCES (Continued)

Rayment, R. and C. J. Readings, 1974: A case study of the structure and energetics of an inversion. Quart. J. R. Met. Soc., 100, pp. 221-233.

Rowland, J. R., 1973: Intensive probing of clear air convective fields by radar and instrumented aircraft. J. Appl. Meteor., 12, pp. 149-155.

Schlichting, H., 1968: Boundary Layer Theory. McGraw Hill, New York, p. 432, 447, 501, 544-559.

Walter, L. S., 1973: Environmental surveys, Discipline Summary Report of Proceedings of Symposium on Significant Results obtained from ERTS-1, NASA Publication x-650-73-155, Goddard Space Flight Center, Washington, pp. 47-56.

APPENDIX A

THEORY OF FORMATION OF MESOSCALE CLOUD BANDS

APPENDIX A

THEORY OF FORMATION OF MESOSCALE CLOUD BANDS

A.1 The Rayleigh-Kuettner Theory of Cloud Bands

The perturbation theory of helical circulations in a shearing windfield is very intricate and requires many assumptions because of the mathematical intractability of the system of basic equations (Brown, 1970, 1972; Kuettner, 1971). From the physical point of view, one can say that the flow is dominated by two forces: thermal buoyancy forces due to heating, and inertial forces that tend to restore the air parcels to their original levels. The second force is associated with the vertical windshear $\frac{\partial U}{\partial z}$ and its gradient $\frac{\partial^2 U}{\partial z^2}$, which, under (fairly valid) assumptions of uniform two-dimensional large-scale flow, can be viewed as vorticity along a horizontal axis perpendicular to the direction of flow. With a shear gradient that diminishes with height, buoyant parcels originating at lower elevations are subject to stronger restoring forces during their ascent than those nearer the wind maximum. The latter are more likely to retain most of their upward momentum and to reach the level of maximum wind. A similar likelihood exists for parcels moving downward from the top of the convective layer. Those which pass through the wind maximum will find some level on the other side at which the horizontal wind component of the environment is the same as their own. For this to be accomplished the loss of parcel momentum due to turbulent exchange must be compensated by buoyancy forces.

How long parcels can retain their identity depends on the rate at which they exchange heat and momentum with their environment. Hence, the diffusivities for heat and momentum which incorporate contributions made e weight and the rate of evaporation of condensation products pl important part in the system of equations. Also, since the resistance of the shearing flow to a superimposed thermally driven circulation is smallest in a plane perpendicular to the mean wind vector, the regions of ascending and descending motions are parallel to the direction of the synoptic-scale flow.

With the uncertainties in the magnitude of the diffusion coefficients and the inaccuracies involved in the computation of second derivatives from already crude wind data, it is virtually impossible to test

the Rayleigh-Kuettner theory. However, qualitative comparisons of the observed spacing of the cloud bands and the associated meteorological conditions show good agreement with the predicted shape of the wind profile and the depth of the convective layer.

The following equation for perturbation growth in a flowing medium heating from below (Kuettner, 1971) relates the dimensions of the cloud pattern to the large-scale flow under given conditions of static stability and small-scale turbulence in the convective layer:

$$\sigma_r = \pm [g\beta(l^2 + m^2)/d^2 - (l\overline{U''}/2d^2)^2]^{1/2} - \nu^* d^2 \qquad (2)$$

Here, σ_r is the real buoyancy part of an exponential time constant, representing a growth rate parameter for banded convection; g is gravity; β is $\frac{1}{\theta}\frac{d\theta}{dz}$ instability; θ is potential temperature; z is height; l and m are wavenumbers along the x and y axis (Figure 3-2b); d^2 is $(l^2 + m^2 + n^2)$; n is $\frac{\pi}{H}$; H is the depth of the convective layer; U is the time-averaged environmental wind component in the x-direction; " is the second derivative with respect to height; an overbar denotes an average over the depth H; and $\nu^* = (k\nu)^{1/2}$ where k and ν are the diffusivities for heat and momentum. The derivation of this equation rests on the following assumptions: the flow is incompressible, viscous and conductive over a depth H of "infinite" horizontal extent and steady state under gravity. The underlying surface is flat and the wind speed (but not its direction) varies with height. The vertical density gradient is constant, positive and small in comparison to the density itself (Boussinesq approximation). It is furthermore assumed that both the kinematic viscosity ν and the heat diffusivity k are invariant and equal throughout the medium and that a linear thermal expansion function holds for the small density changes under consideration. The Coriolis force is neglected.

These assumptions seem reasonably valid under the synoptic conditions accompanying the manifestations of bandedness in a cloud pattern, particularly over oceans and flat land surfaces.

A.2 Solutions of the Perturbation Equation

The proposed steady-state solutions of Equation 2 are considered to be valid for well developed cloud bands in which the elements change little with time. Assuming $\sigma_r = 0$ (no further growth of the cloud bands) we can solve for $\overline{U''}$, the second derivative of the ambient wind averaged over the depth H. This may give us a simple, first order approximation of the vertical wind profile between the surface and the top of the convective layer, i.e.:

$$\overline{U''} = \left(-\nu^{*2}\frac{d^4}{B^2} + \frac{A}{B^2}g\beta\right)^{1/2} \; m^{-1} \; sec^{-1} \qquad (3)$$

where

$$A = (l^2 + m^2)/d^2, \text{ and}$$

$$B = \frac{1}{2d^2}$$

The wave numbers l, m and n can be evaluated from the spacing and vertical dimensions of the cloud elements in the banded pattern displayed by the satellite pictures. The solution of U'' is given by:

$$\overline{U''} = \overline{\frac{\partial^2 U}{\partial z^2}} = -C_1$$

$$\frac{\partial U}{\partial z} = -C_1 Z + C_2$$

$$U = -0.5\, C_1 Z^2 + C_2 Z + C_3 \qquad (4)$$

Here we assume that the second derivative of the wind speed is constant with height and has a value given by the solution of Equation 3. To solve for the constants C_2 and C_3 we impose the following boundary conditions suggested by the shape of observed wind profiles in regions with cloud bandedness and unidirectional flow

1) The vertically averaged wind speed $\overline{U}^H$ in the layer of depth H is related to the maximum wind speed U_{max} according to the linear regression equation:

$$U_{max} = K_1 \overline{U}^H + K_2 \tag{5a}$$

where K_1 and K_2 are constants.

2) The wind maximum occurs at a constant height

$$Z_{max} = \eta H \tag{5b}$$

3) $C_3 = U_o$ for Z = 0, i.e., a surface wind, which is not necessarily equal to zero, and which has to be assumed on a basis of climatology.

From Equation 4, the vertically averaged wind speed in the layer is given by:

$$\overline{U}^H = -\frac{1}{6} C_1 H^2 + \frac{1}{2} C_2 H + C_3 \tag{6}$$

For $Z = \eta H$, $U = U_{max}$; $\partial u/\partial z = 0$; $C_2 = C_1 Z_{max}$ and $U_{max} = 0.5\ Z_{max}^2 + C_3 = 0.5\ C_1 \eta^2 H^2 + C_3 = K_1 \overline{U}^H + K_2$,

$$C_2 = \frac{(0.5\eta^2 + 0.1667\ K_1) C_1 H^2 + (1 - K_1) C_3 - K_2}{0.5\ K_1 H} \tag{7}$$

K_1, K_2 and η have to be found empirically. The relationship between U_{max} and $\overline{U}^H$, obtained from 32 observed Kuettner-type wind profiles associated with cloud streets is shown in Figure A-1 and seems to be stable enough to justify boundary condition 1. Hence, K_1 is set equal to 1.181 and K_2 = 3.613. Boundary condition 2 is less stable but the departures from the observationally determined average location of the wind speed maximum do not seem to produce errors in the solution for the average wind speed $\overline{U}^H$ of more than 50 percent.

The effect of errors in η, the location of the wind maximum with respect to the top of the unstable layer, is shown in Table A-1, in which η = 0.65 (the average value is used for reference).

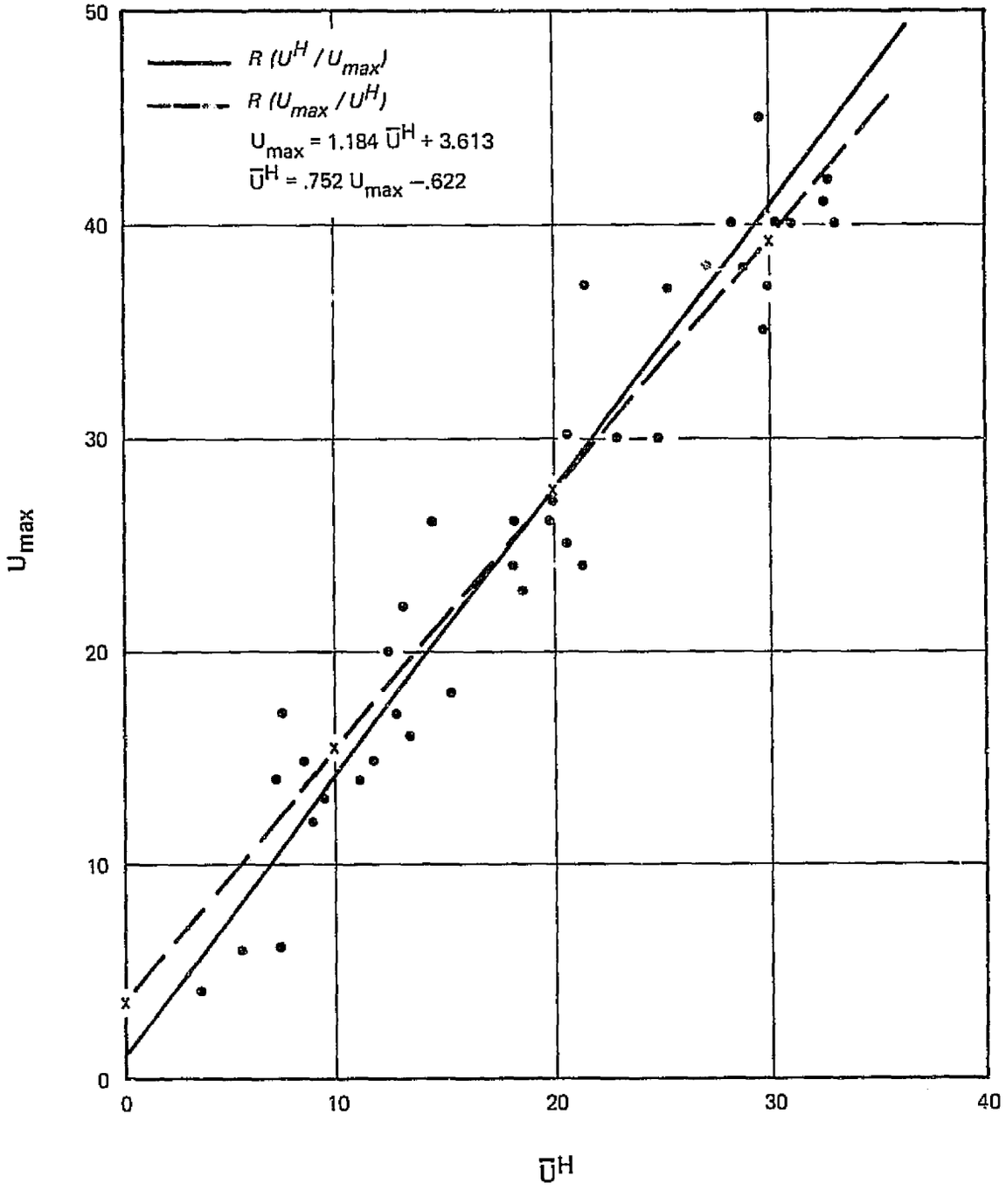

The correlation coefficient is 0.94, and the straight lines correspond to the regression equations shown in the inset.

Figure A-1 Graph Showing the Correlation between Maximum Wind Speed (U_{max}) and Average Wind Speed ($\overline{U}^H$) in Convective Layers during Strong Surface Heating

609016

TABLE A-1

DEPENDENCE OF THE RELATIVE ERROR IN THE COMPUTED AVERAGE WIND SPEED $\overline{U}^H$ ON THE LOCATION η OF THE WIND SPEED

Location η	Average Wind Speed $\overline{U}^H$ ($msec^{-1}$)	Relative Error ($msec^{-1}$)
0.50	7.5	-7.3
0.55	9.0	-5.8
0.60	12.1	-2.7
0.65	14.8	0.0
0.70	17.6	2.8
0.75	20.7	5.9

TABLE A-2

DEPENDENCE OF THE COEFFICIENT K_6 IN EQUATION 7a ON ASSUMED VALUES FOR THE WIND SPEED C_3

Wind Speed Values C_3 ($msec^{-1}$)	Coefficient Values K_6 ($msec^{-1}$)
0	- 6.1
2.7	- 6.9
5.4	- 7.8
8.2	- 8.6
10.9	- 9.5
13.6	-10.3
16.3	-11.2

The use of 0.65 in Table A-1 shows good agreement with the work of Kuettner (1959, 1971), where, in 11 out of 15 cases, the wind maximum occurred at levels between 0.5 and 0.7 H.

Separating assumed (and therefore constant) coefficients from the variables one may rewrite (7) in more convenient form:

$$C_2 = \frac{1}{H}\left\{\frac{0.5\ \eta^2 + 0.1667\ K_1}{0.5\ K_1} C_1 H^2 + \frac{(1 - K_1)C_3 - K_2}{0.5\ K_1}\right\}$$

$$= \frac{1}{H}\left(K_5 C_1 H^2 + K_6\right) \qquad (7a)$$

Coefficient K_5 is sensitive to η whereas K_6 depends on the assumptions for the surface wind speed C_3 as shown in Table A 2.

Observations (Kuettner, 1971) suggest that the product $|\overline{U'''} H^2| = C_1 H^2$ lies close to 100 m sec^{-1}. Hence, K_5 is close to 70, so that a departure of even 5 $msec^{-1}$ from the assumed surface wind speed C_3 causes an error in C_2 of only three percent. Therefore, it is the errors in the surface wind which dominate in Equation 6 and give an error of approximately the same order of magnitude in the end result.

This particular weakness in the assumed wind profile model stems from the mathematical intractability of the flow properties in the lowest turbulent layer which depends very much on the roughness of the underlying terrain. Over open water this problem may be mitigated as in all likelihood there exists a rather simple relationship between the wind at ship level and the geostrophic wind or the average wind in the convective layer, from which C_3 can be derived analytically. Over land C_3 is arbitrarily set at 5.4 $msec^{-1}$.

Apart from the effect of errors in the boundary conditions on the solution, errors on the solutions for $\overline{U'''}$ in Equation 3 have to be considered. As will be shown, these depend rather critically on the assumptions for β, the average instability in the convective layer and to a much lesser extent on ν^*, the diffusivity parameter. However, since the shape of the wind profile depends to a large extent on the static stability and the degree of turbulence (see, for instance, Schlichting, 1968), there is reason to believe that there exists a rather stable relationship among the parameters β, ν^*, h, U_{max} and $\overline{U}^H$.

Since this investigation is aimed at an expedient evaluation of air mass and flow properties under conditions of cloud banding by cloud pattern evaluation, our approach to the problem remains mostly an empirical one. Figure A-2 shows the relationship between average wind speed $\overline{U}^H$ for given values of H, λ_y/H, ν^*, K_1, K_2 and η, derived from Equations 3, 4, 5 and 6. It must be remembered, however, that values above 2 km would not be valid for the equations. Figure A-3 shows the dependency of $\overline{U}^H$ on the instability β and the depth H of the layer, keeping the other variables constant. Note that the average wind speed increases strongly with increasing buoyancy and cloud depth, showing that stronger heating is needed to maintain cloud bands in stronger and shallower flows.

Even though over any reasonably uniform terrain, H can probably be determined fairly accurately with modern photogrammetric satellite output analysis techniques, good estimates of $g\beta$ will be hard to come by even over areas where rawinsonde observations are made routinely. Yet the deeper the clouds and the stronger the heating from below, the more accurately we need to know $g\beta$ to predict the wind profile associated with a certain cloud street pattern. The dependency of $\overline{U}^H$ on the spacing of the cloud streets is much less critical. In most cases with deep convection, the diffusivity parameter ν^* has little effect on the wind profile solutions. Even variations of ν^* by four orders of magnitude change U'' and $\overline{U}^H$ only by a few percent. This would mean that the rate of mixing of ambient heat and momentum into the updrafts is largely independent of the characteristics of the large-scale flow.

A.3 Relationship Between Cloud Street Geometry and Average Buoyancy in the Convective Layer Suggested by Simple Thermodynamical Considerations

Since the quantity $g\beta$ is very difficult to estimate even from sophisticated ground truth, attempts have been made to estimate its order of magnitude from a very simple convection model, originally based on parcel theory and adjusted on the basis of observations of temperature and liquid water in cumulus clouds.

Originally the atmosphere is gravitationally stable for unsaturated air and gravitationally unstable for saturated air, i.e.,

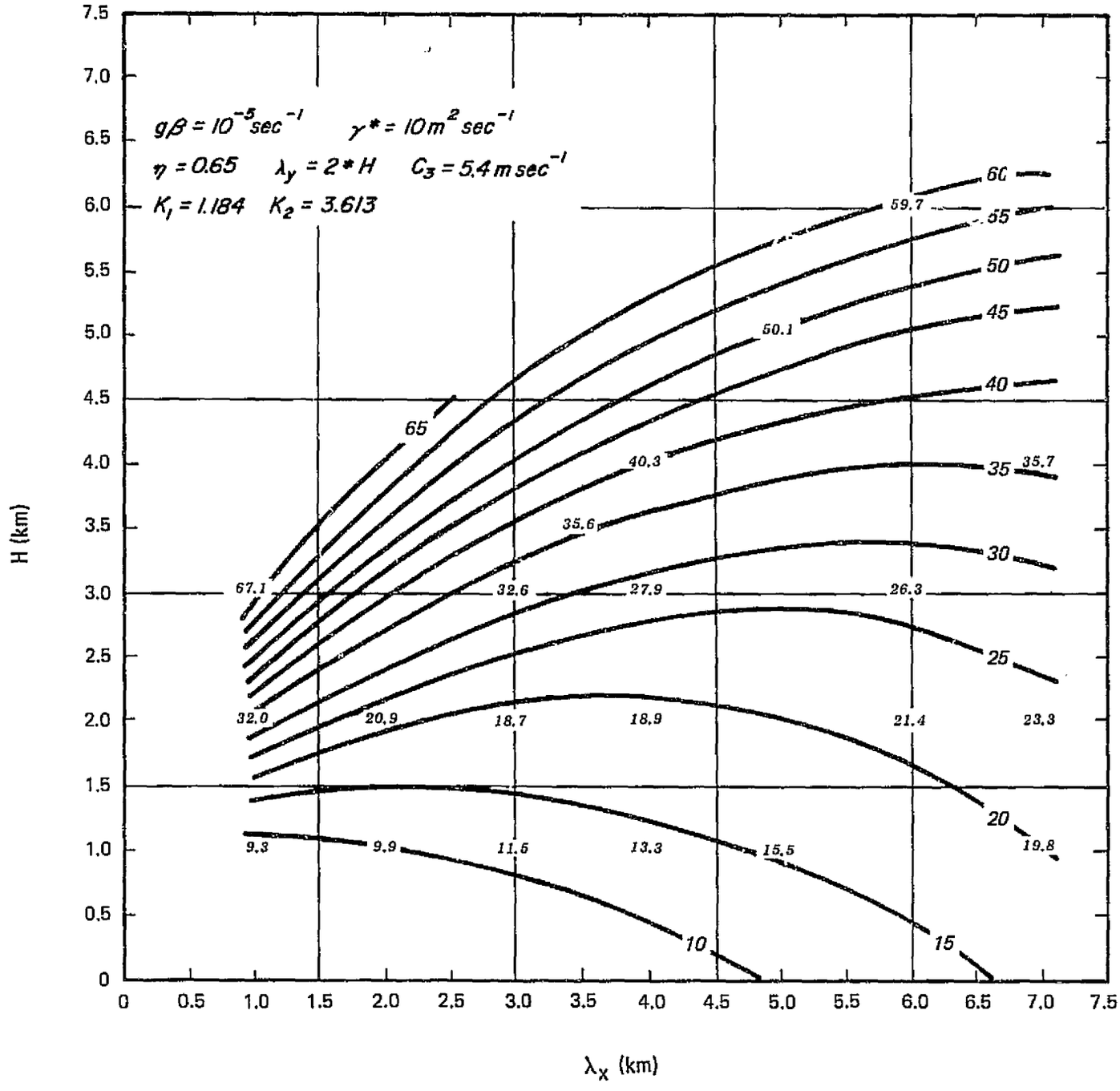

Figure A-2 Graph Showing the Average Wind Speed in the Layer $0<z<H$ as a Function of λ_x and H for Specified Conditions

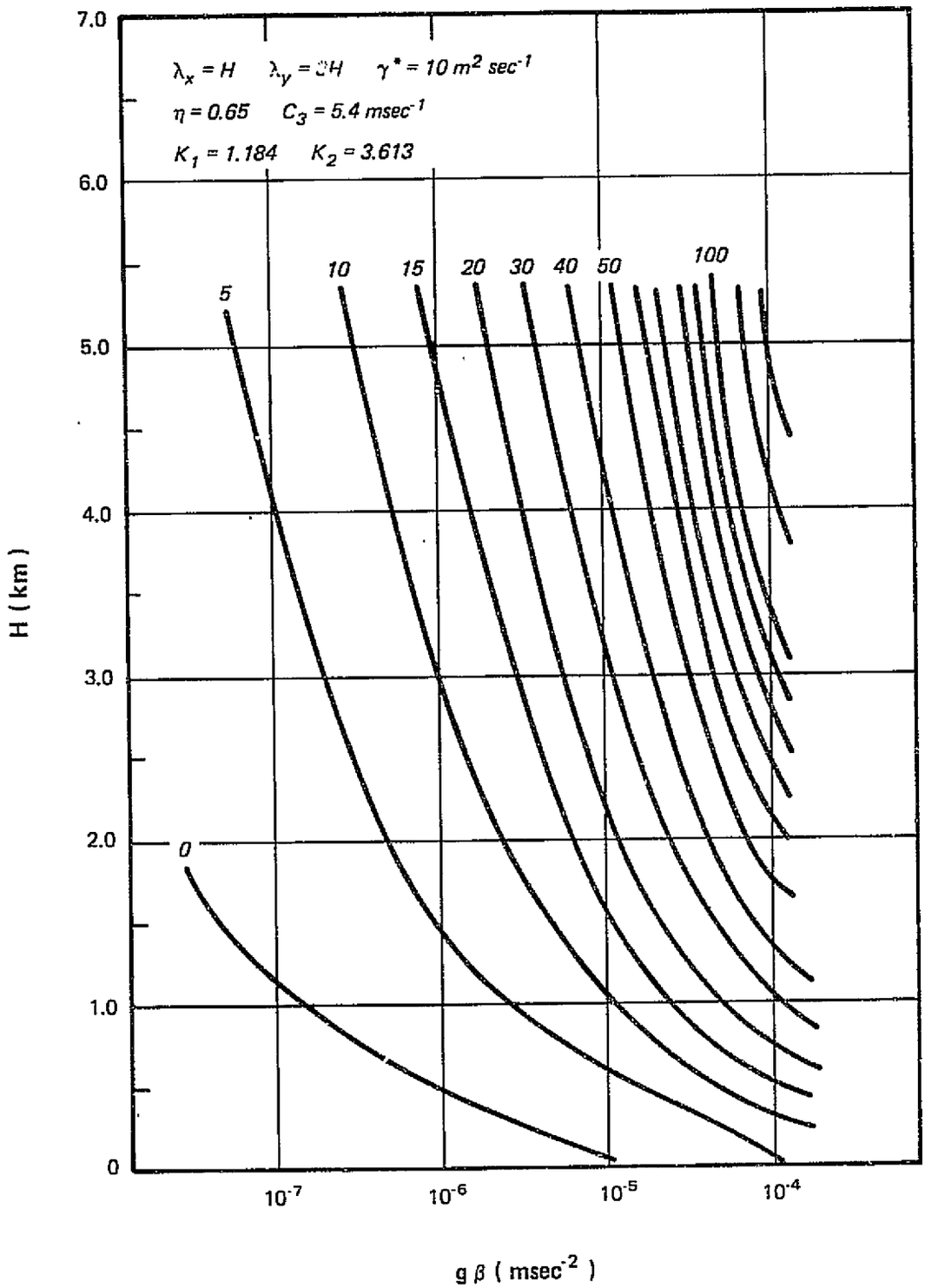

Figure A-3 Graph Showing Average Wind Speed in the Layer $0<z<H$ as a Function of H and $g\beta$ for Specified Conditions

$$\Gamma_d < -\frac{\partial T}{\partial z} < \Gamma_m$$

where Γ_m and Γ_d are most adiabatic and dry adiabatic lapse rates, respectively.

Suppose now that a saturated air parcel is lifted from Z to Z + dZ. Assuming that the pressure at Z + dZ does not change, then, according to the gas law the restoring force per unit mass is

$$-F_m\, dz = g(\partial\rho/\rho) = -g(\partial T/T) = -g[(\Gamma_m - \Gamma_e)/T]dz \quad (8)$$

where Γ_e is the lapse rate of temperature in the environment. Thus, if $\Gamma_e - \Gamma_m < 0$ the atmosphere is conditionally unstable.

In reality, rising motion must be compensated by descending motion to preserve mass continuity. Let us schematically denote the area of rising motion at a fixed level by A_+ and the area of sinking motion by A_-. Let a typical upward displacement be $\ell_+ A_+ = \ell_- A_-$. The work W_- done against buoyancy in the downward displacement is measured by $W_- = F_e \ell_-^2 A_-$ and the work by buoyancy forces against gravity in the upward displacement is measured by $W_+ = F_m \ell_-^2 A_+$. The ratio of the two is:

$$\frac{W_+}{W_-} = \frac{F_m \ell_+^2 A_+}{F_e \ell_-^2 A_-} = \frac{F_m A_+}{F_e A_-} \quad (9)$$

If energy is to be released we must have

$$\frac{A_+}{A_-} < \frac{F_m}{F_e} = (\Gamma_e - \Gamma_m)/(\Gamma_d - \Gamma_e) \quad (10)$$

This energy is at least an order of magnitude smaller than W_+ and W_- in the helical circulations associated with cloud streets (Brown, 1970). Hence we assume: $A_+/A_- \approx F_m/F_e$.

In a regularly spaced group of nearly straight uniform cloud bands we find from symmetry:

$$\frac{A_+}{A_-} = \frac{\lambda_x}{\lambda_y - \lambda_x} \quad (11)$$

where λ_x is the distance between the centers of the individual cumulus elements within a band and λ_y is the spacing of the cloud bands (see Figure A-2). The cumulus elements in a band are assumed to be symmetric and closely linked together and the flow is assumed upwards in cloud and downwards in clear air. These assumptions are met in most cloud streets (Kuettner, 1959, 1971). Hence we can put

$$\frac{\lambda_x}{\lambda_y - \lambda_x} \approx \frac{\Gamma_e - \Gamma_m}{\Gamma_d - \Gamma_e} \tag{12}$$

Knowing the approximate surface temperature of the airmass and the depth of the convective layer, Γ_d and Γ_m can be determined from parcel theory on a thermodynamic diagram.

Solving Equation 12 for Γ_e, the temperature lapse rate in the cloud free air we find:

$$\Gamma_e = \frac{C\Gamma_d + \Gamma_m}{1 + C} \tag{13}$$

where $C = \lambda_x/(\lambda_y - \lambda_x)$.

The average buoyancy $\overline{\beta}$ in the cloud layer is then given by:

$$\overline{\beta} = \frac{1}{\overline{T}} (\overline{\Gamma_m - \Gamma_e}) = \frac{C}{1 + C} \cdot \frac{1}{\overline{T}} (\overline{\Gamma_m - \Gamma_d})$$

$$= \frac{1}{\overline{T}} \frac{\lambda_x}{\lambda_y} (\Gamma_m - \Gamma_d) \tag{14}$$

where $\overline{T}$ is the average temperature of the layer.

It must be borne in mind that this derivation is based on parcel theory and the tacit assumption that in the cloud the buoyancy is positive. However, even in rising cloud parcels the buoyancy is not necessarily always positive, and it is definitely not in clouds or parts of clouds that are colder than their environment, as has been frequently observed. In dense clouds the weight of the suspended condensation products may be large enough to completely offset upward buoyancy forces (Saunders, 1957). Model computations (Kessler, 1971; Betts, 1973) and observational evidence (Byers and Braham, 1949; Telford and Warner,

1962) suggest that probably only one-tenth of the cloud area is positively buoyant. Hence we assume:

$$\beta = \frac{KE}{T} \frac{\lambda_x}{\lambda_y} (\Gamma_m - \Gamma_d), \quad KE \approx 0.1 \tag{15}$$

Actually, there are two reasons to believe that kinetic energy (KE) decreases with temperature. First, the saturation deficit in warm air increases faster with decreasing relative humidity, so that evaporation and the resulting cooling proceed faster at the edges of the cloud. Secondly, where the updrafts are protected from dilution the weight of suspended cloud and precipitation elements increases faster in updraft due to the increased rate of supersaturation and condensation in warmer parcels. This dependency of β on climatic factors has not yet been shown by direct observation.

Summarizing, we can say that under certain conditions such as steady state, incompressibility, viscous and conductive unidirectional flow on a flat surface and constant vertical gradient of the vertical windshear, that realistic values of the wind speed can only exist for limited regions of the values of η (the ratio of the height Z_{max} of the wind maximum to the depth H of the layer) and the average instability $\overline{\beta}$. To ascertain the extent to which cloud bands are indeed in a steady state requires time-lapse photography. There may well be a delicate balance among the parameters U, U'', η, ℓ, m, n, ν^* and $g\beta$ to which the atmosphere continuously adjusts. The solution for the maximum wind speed in the convective layer relies heavily on this assumption, but it does provide us with a simple tool to estimate the main characteristics of low-level flow in data-silent areas from the properties of the cloud bands only.

Equations 3, 4, 5, 6 and 15 enable us to estimate the average flow in an airmass with marked cumulus banding over a data-silent area from one single Landsat image. The pertinent cloud pattern characteristics, λ_x, λ_y and H are easy to measure; the only ground truth needed is an estimate of the surface wind and the surface temperature obtained from available data sources.

A.4 Boundary Conditions for Cloud Bands Over Sea Surfaces

As stated above, the uncertainty in the boundary conditions for Z = 0 has a large effect on the steady-state solutions of the Rayleigh-Kuettner Equation 3. Due to the great variability of the surface wind observed under similar conditions of stability and large-scale flow, it is very difficult to determine the integration constant C_3 in Equation 4, which depends largely on local terrain features. In our case studies a value of 5.4 m sec^{-1} was assumed for this constant.

However, over sea surfaces where polar outbreaks are accompanied by much more regular cloud banding than over land there may well be a stable relationship between the wind speed U_s at ship level (10m above the surface) and the average wind speed $\overline{U}^H$ in the convective layer. If this can be represented by simple linear regression of the type:

$$U_s = C_3 = K_7\overline{U}^H + K_8 \tag{16}$$

the constant C_3 can be eliminated by substitution of this relationship in

$$\overline{U}^H = \frac{1}{6} C_1H^2 + \frac{1}{2} C_2H + C_3 \tag{6}$$

and

$$C_2 = \frac{(0.5\ n^2 + 0.1667\ K_1)C_1H^2 + (1 - K_1)C_3 - K_2}{0.5\ K_1H} \tag{7}$$

which gives the following solution for $\overline{U}^H$, independent of assumptions about the actual ground truth:

$$\overline{U}^H = \left(\frac{K_1}{K_1 - K_7}\right)\left[\left(\frac{K_5}{K_1} - \frac{1}{6}\right)C_1H^2 + \frac{K_8}{K_1} - \frac{K_2}{K_1}\right] \tag{17}$$

in which $K_5 = 0.5\ n^2 + 0.1667\ K_1$ and C_1H^2 is determined solely from cloud pattern characteristics. The coefficients n, K_1, K_2, K_7 and K_8 would have to be determined statistically from ship rawinsondes in areas with cloud banding, as shown in Table A-3. It appears that the

TABLE A-3

DEPENDENCE OF SOLUTIONS OF EQUATION 17 ON
ASSUMED VALUES OF PERTINENT COEFFICIENTS

C_1H^2 (m sec^{-1})	η	K_1	K_2	K_7	K_8 (m sec^{-1})	$\bar{U}^H$ (m sec^{-1})	U_s (m sec^{-1})
100	0.65	1.18	3.6	0.75	1.0	42.7	33.0
100	0.65	1.18	3.6	0.50	1.0	27.1	14.6
100	0.50	1.18	3.6	0.50	1.0	14.5	8.3
100	0.50	1.30	0	0.50	1.0	16.9	9.5

solutions of 17 will be sensitive to deviations from the average location of the wind maximum in the convective layer (η) and to the regression coefficient K_1 which relates the surface wind speed U_s to the average wind speed $\overline{U}^H$.

APPENDIX A

REFERENCES

Betts, A. K., 1973: Non-precipitating cumulus convection and its parameterization. Quart. J. R. Met. Soc., 99, pp. 178-196.

Brown, R. A., 1970: A second flow model for the planetary boundary layer. J. Atmos. Sci., 27, pp. 742-757.

Brown, R. A., 1972: On the inflection point instability of a stratified Ekman Boundary Layer., J. Atmos. Sci., 29, pp. 850-859.

Brown, R. A., 1972: On the physical mechanism of the inflection point instability, J. Atmos. Sci., 29, pp. 984-986.

Byers, H. R. and R. R. Braham, 1949: The Thunderstorm, U. S. Government Printing Office, Washington, D. C., pp. 20-32.

Kessler, 1971: Model of Precipitation and Vertical Air Currents, NOAA Tech. Memo, ERL-NSSL 54, pp. 4-10.

Kuettner, J. P., 1959: The Band Structure of the Atmosphere. Tellus 11, No. 3, pp. 267-294.

Kuettner, J. P., 1971: Cloud Bands in the Earth's Atmosphere, Observations and Theory. Tellus 23, 4-5, pp. 404-426.

Saunders, P. M., 1957: The thermodynamics of saturated air; a contribution to the "classical" theory. Quart. J. R. Met. Soc., 83, pp. 342-350.

Telford, J. W. and Warner, J., 1962: On the measurements from an aircraft of buoyancy and vertical velocity in cloud. J. Atmos. Sci.; 9, pp. 415-423.

APPENDIX B

THEORY OF FLOW FOR TERRAIN-INDUCED CLOUDS

APPENDIX B

THEORY OF FLOW FOR TERRAIN-INDUCED CLOUDS

Since a considerable number of Landsat images display terrain-induced clouds, a brief survey of the theory of formation of clouds over mountains will be given. Most of the literature up to 1967 is summarized in Alaka (1968). Since then computer models of orographic clouds have appeared, but these analytical studies are already highly sophisticated, since wave phenomena are mathematically tractable to a high degree of approximation and amenable to verification by only specially designed field projects. Even with the available high speed computers, calculations of the wind profile from wave cloud characteristics and the shape of the mountains would be quite prohibitive for routine computation since the stratification of temperature and relative humidity would have to be known in space and time to an accuracy which is unattainable by present-day routine soundings.

Simplified first-order approximations of the basic equation, though, seem to give a fair estimate of the average wind speed in the cloud layer, because above level ground downstream from the mountain ridge, the wavelength of mountain-induced disturbances depends mainly on the characteristics of the airstream. Since wave clouds are produced in stable stratified flow, parcels subjected to vertical displacement over the mountain top become negatively buoyant and, hence, attempt to move back to their level of origin. The resulting gravity-inertia forces tend to cause oscillations of the parcels about their equilibrium positions. The balance of forces is given by the differential equation

$$\frac{d^2z(t)}{dt^2} + g\,\frac{\Gamma_d - \Gamma_e}{\bar{T}}\,Z(t) = 0 \qquad (1)$$

of which the simplest solution contains a parameter F, expressing the dynamical state of the airstream at any level in the atmosphere

$$F(z) = \frac{g\bar{\sigma}}{\bar{U}^2} - \frac{\bar{U}''}{\bar{U}} \qquad (2)$$

in which σ is the static stability, $(\Gamma_d - \Gamma_e)/\overline{T}$, Γ_d and Γ_e are the dry adiabatic and environmental lapse rates respectively, $\overline{T}$ is the average absolute temperature, g is gravity, $\overline{U}$ is the large-scale horizontal wind speed in the layer and $\overline{U}''$ is its second derivative with respect to height. F is related to the wavelength of the gravity waves by

$$F = \left(\frac{2\pi}{\lambda}\right)^2$$

In many wind profiles $\overline{U}''$, being a small difference between large numbers, is difficult to determine. When $\overline{U}''$ is set to zero the expression for F can be substituted in (2) to solve for the average large-scale wind speed:

$$\overline{U} = \frac{\lambda}{2\pi} (g\sigma)^{1/2} \qquad (3)$$

Using the unidirectional flow outlined in Appendix A, it is possible to deduce a relationship between $\overline{U}''$ and $\overline{U}^H$, the vertically averaged wind speed in the layer from Equations 5a, 6, and 7 (Appendix A); namely

$$\overline{U}^H = \frac{{}^1/_2\ K_6 + C_3}{1 - ({}^1/_6 + {}^1/_2\ K_5)\ F(z)\ H^2} \qquad (4)$$

Here $\overline{U}''$ has been assumed to be constant through the layer depth H and equal to its average. For assumed surface wind speeds of the order of 10 knots and a wind maximum at Z = 0.65 H:

$$\overline{U}^H = \frac{9.3}{1\ 0.5117\ \frac{2\pi}{\lambda} H^2} \quad \frac{9}{1\ \ 20\ (H/\lambda)^2}\ \text{m sec}^{-1} \qquad (4a)$$

The justification for this approach can be verified by inspection of the solutions of Equation 1 for negative values of the wind profile curvature U''. These clearly demonstrate that in this case the average wind speed in the layer is strongly dependent on curvature and wavelength but only weakly dependent on the static stability in the range $0 < \sigma < 10^{-4}$, a fact which is frequently observed in cold unstable low-level flows. Note that σ is a measure for the restoring forces, whereas the instability β applies to dry and moist convection in flows which are heated from below.

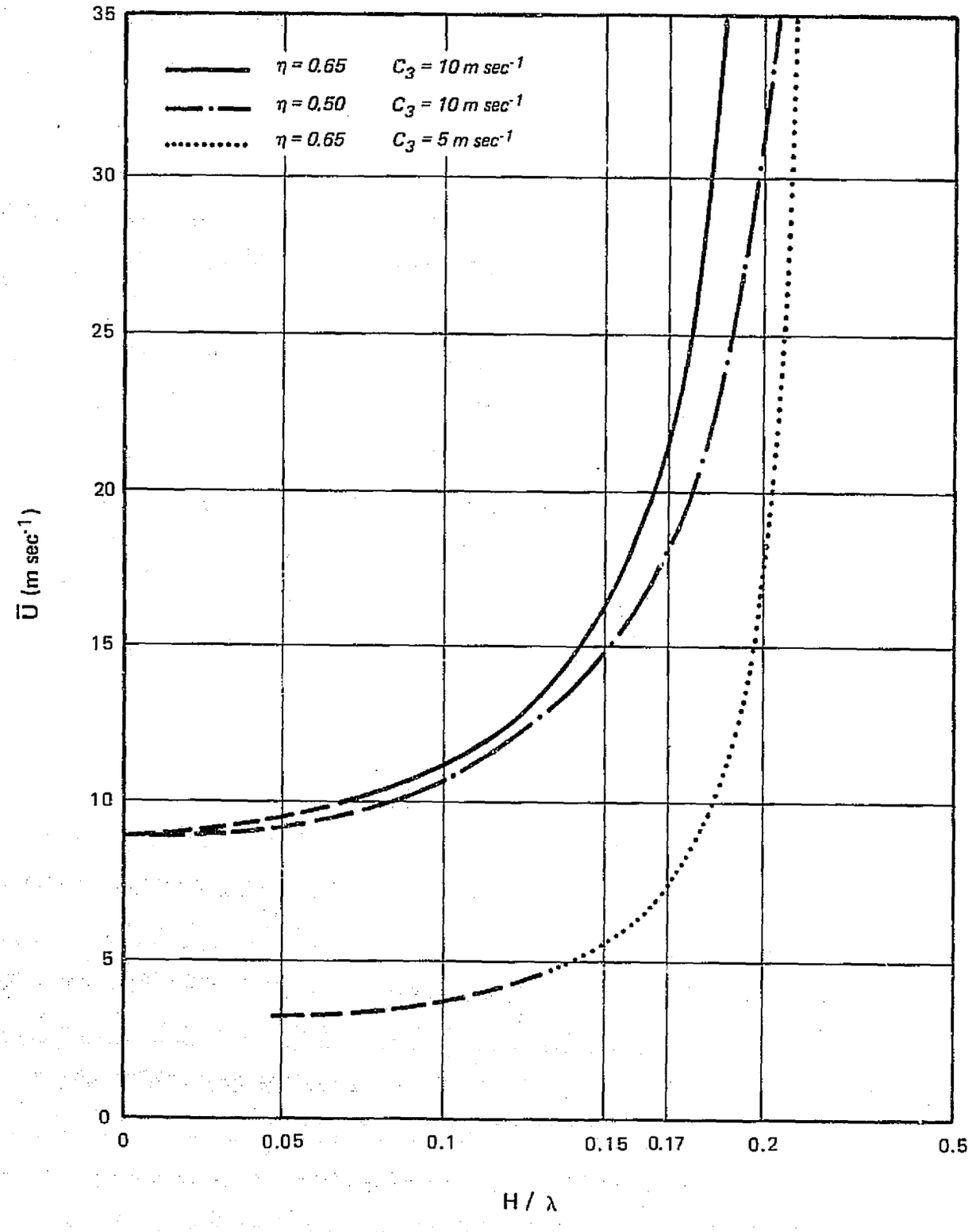

Figure B-1 Graph Showing Solution of Equation 4 for $\bar{U}$ when $F=(2\pi/\lambda)2=-\bar{U}'/\bar{U}$

Cases of marginal stability and hybrid manifestations of Kuettner-type cloud banding and gravity-inertial waves have already been discussed in Section 3 and Appendix A. Solutions of Equation 4, derived from Equation 2, are presented in Figure B-1.

APPENDIX B

REFERENCES

Alaka, M. A., 1968: The Airflow Over Mountains, W.M.O. Technical Note 34, Geneva, Switzerland, 135 pp.